UNIVERSITY OF WISCONSIN - MADISON

MASTERS OF SCIENCE THESIS

Advanced Energy Management for Energy Storage Systems

DECEMBER 2018

Author:

Ryan P. HICKEY

Supervisor:

Dr. Thomas M. JAHNS

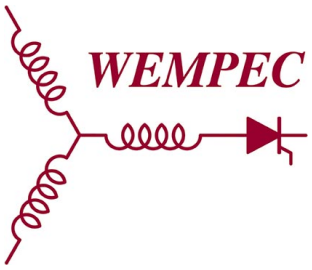

A thesis submitted in fulfillment of the requirements

for the degree of Masters of Science

in the

Wisconsin Electric Machines and Power Electronics Consortium

(WEMPEC)

Electrical and Computer Engineering

UNIVERSITY OF WISCONSIN - MADISON

Abstract

Dr. Thomas M. Jahns

Electrical and Computer Engineering

Masters of Science

Advanced Energy Management for Energy Storage Systems

by Ryan P. HICKEY

The objective of this thesis is to investigate how the EMS for batteries in both vehicle and stationary (e.g., grid-tied energy storage) applications can be enhanced using one of three different approaches. The first of these is the evaluation of battery models such as State of Energy (SOE) to understand system enhancements in comparison to traditional SOC tracking. A direct comparison between SOE and SOC is evaluated on a per discharge event basis, but additionally as the battery is aged to understand model error between SOE and SOC. Next, the second aspect of this thesis is for battery sensors, but more specifically, the implementation of pressure, or battery dimensional change sensors to correlate to SOC as a more rapid SOC adjustment scheme. The third and final approach being pursued to enhance EMS performance is called dynamic reconfiguration (DR). DR uses power electronic switches (e.g. MOSFET, IGBT, etc.) inside the battery pack to give the EMS the ability to adaptively reconfigure the series/parallel configuration of the cells during operation in order to optimize the battery's contribution to system performance as a function of the system operating point together with the battery's present condition, including SOC and SOH. This work is being evaluated by simulation in order to understand lifetime performance capability which has previously not been evaluated in the field.

Acknowledgements

I first would like to thank Johnson Controls, for without their financial & technical support this project would not have been possible. With my years of experience within Johnson Controls, there are countless people that have helped me get to where I am today, & this project reflects the countless support that all of my colleagues throughout my time with Johnson Controls have provided. I would like to give special acknowledgements to specific individuals throughout my time collaborating with JCI that have dedicated extensive time throughout my educational process. First & foremost, I would like to give special thanks to MaryAnn Wright. Without your help & guidance throughout my life I truly would not be where I am today. Your help & advice throughout the years has been invaluable to me. Next I would like to thank Dr. Patrick Hurley, who has personally taken time away from his work and family to help me throughout the years in my research. Your help & guidance has been incredible, & the guidance you have continued to give since your departure from JCI was above & beyond anything I could have ever asked for.

I would like to next thank my advisor, Dr. Tom Jahns, who dedicated countless hours throughout my time in graduate school to help the completion of this project. Your knowledge and expertise was critical in helping to guide this project in the right direction. In addition to Dr. Jahns, I'd like to extend my thanks to the entire WEMPEC group (Wisconsin Electric Machines and Power Electronics Consortium) for everyones support. A special shoutout goes to a fellow graduate student, Peter Killeen, whom loaned me his very expensive personal computer to aid me in my research centered around Dynamic Reconfiguration. The use of his computer allowed this project to be completed, and was greatly appreciated.

Last but certainly not least, I want to thank my family, & specifically my parents, Dori Hickey, Bill & Tina Hickey, for the unconditional support in my academic career, as well as all other aspects in my life.

Table of Contents

List of Figures

List of Tables

List of Abbreviations

Ah	**A**mp **h**our
BEV	**B**attery **E**lectric **V**ehicle
BOL	**B**eginning **O**f **L**ife
CCCV	**C**onstant **C**urrent **C**onstant **V**oltage
C-Rate	**C**urrent – **R**ate
DES	**D**istributed **E**nergy **S**torage
DOD	**D**epth **o**f **D**ischarge
EMS	**E**nergy **M**anagement **S**ystem
EOL	**E**nd **O**f **L**ife
ESS	**E**nergy **S**torage **S**ystem
EV	**E**lectric **V**ehicle
HEV	**H**ybrid **E**lectric **V**ehicle
ICE	**I**nternal **C**ombustion **E**ngine
Li-Ion	**L**ithium - **i**on
OCV	**O**pen **C**ircuit **V**oltage
P-Rate	**P**ower – **Rate**
PCM	**P**hase **C**hange **M**aterials
SOC	**S**tate **o**f **C**harge
SOE	**S**tate **o**f **E**nergy
SOF	**S**tate **o**f **F**unction
SOH	**S**tate **o**f **H**ealth
SOP	**S**tate **o**f **P**ower
SPC	**S**witches **P**er **C**ell
Wh	**W**att **h**our

List of Symbols

Symbol	Name	Unit
E_{batt}	Nonlinear voltage	V
E_0	Constant voltage	V
K	Polarization constant	Ah^{-1}
$i*$	Low frequency current dynamics	A
i	Battery current	A
it	Extracted Capacity	Ah
Q	Maximum battery capacity	Ah
A	Exponential voltage	V
B	Exponential capacity	Ah^{-1}
T_{ref}	Nominal ambient temperature	K
T	Cell or internal temperature	K
T_a	Ambient temperature	K
E/T	Reversible voltage temperature coefficient	V/K
α	Arrhenius rate constant for the polarization resistance	[-]
β	Arrhenius rate constant for internal resistance	[-]
$\frac{\Delta Q}{\Delta T}$	Maximum capacity temperature coefficient	Ah/K
C	Nominal discharge curve slope	V/Ah
P_{loss}	Overall heat generated during charge/discharge process	W
t_c	Thermal time constant, cell to ambient	s
R_{th}	Thermal resistance, cell to ambient	°C/W
Q_{BOL}	Battery maximum capacity at BOL, nominal ambient temperature	Ah
Q_{EOL}	Battery maximum capacity at EOL, nominal ambient temperature	Ah

R_{BOL}	Battery internal resistance at BOL, nominal ambient temperature	Ω
R_{EOL}	Battery internal resistance at EOL, nominal ambient temperature	Ω
ε	Battery aging factor	[-]
γ_1	Exponent factor for discharge current	[-]
γ_2	Exponent factor for charge current	[-]
I_{ch_ave}	Average charge current during half cycle duration	Amps
I_{dis_ave}	Average discharge current during half cycle duration	Amps
ψ	Arrhenius rate constant for the cycle number	[-]
ξ	Exponent factor for the DOD	[-]
H	DR cycle number	[-]
T_{a}	Ambient Temperature	°C

Chapter 1

State-of-the-Art Review

1.1 Lithium Ion Battery Overview

Li-Ion batteries were first commercially available in 1991 by Sony, and have been offered ever since due to their higher working voltage profile in comparison to the traditional Nickel based batteries [1]. Li-Ion batteries operate as intercalation electrodes with a lattice structure in which Lithium Ions (Li+) are inserted and removed in both the cathode and anode materials [1, 2]. During the charging process, Lithium Ions are transferred from the cathode (positive electrode) to the anode (negative electrode), and subsequently transferred from anode to cathode during discharge [1, 2]. This charging/discharging process is shown schematically in Figure 1.1 for visual reference [2].

Depending on the application, different electrode materials can be utilized for optimizing the Li-Ion battery for specific targets such as energy, power, etc [2, 3]. Additionally, Li-Ion cells have various geometric options, while in commercial options, the vast majority are cylindrical (e.g., volumetric), or prismatic cell design [2]. Traditionally, cells have been made as cylindrical cell design, but recently the prismatic design has drawn more attention to improve the packing efficiency when stringing large quantities of cells together [1, 2].

1.2 Battery Applications and Systems

Understanding the basic functionality of a Li-Ion battery discussed in the previous section, the use and functionality of batteries in application specific scenarios is key. Many

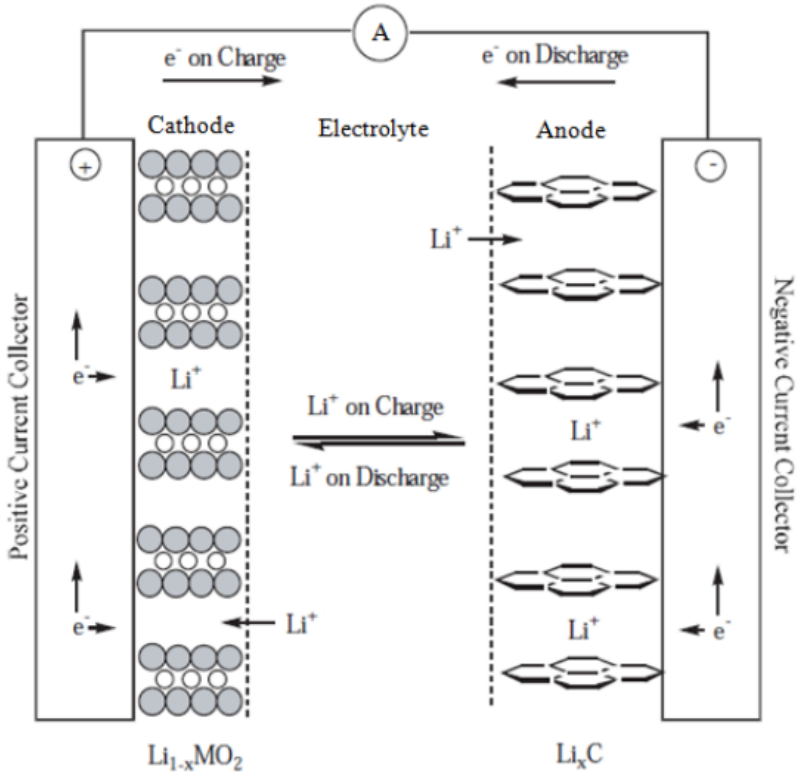

Figure 1.1: Schematic of the electrochemical reactions in Li-Ion cells [2]

applications can be found that utilize an ESS, however for the scope of this project, focusing on automotive and grid related applications will be the focus. Johnson Controls' main battery applications lie in this area, which directs our attention for EMS improvements into these main application areas. Due to this, further discussion into each of these applications should be conducted to understand the potential EMS options.

Figure 1.2 shows the operating range of temperature relative to the operating voltage that can be used for Li-Ion batteries. Understanding the region for safe operation of Li-Ion batteries is critical in all applications when designing the EMS [4]. The key operating window for Li-Ion can be seen in the figure as 1.5V to 4.2V voltage range, and a temperature range of -20C to 50C. This plot is solely meant as an initial requirement, where the actual operating range of a battery can be altered based on specific electrolytes, electrode additives, and cell design.

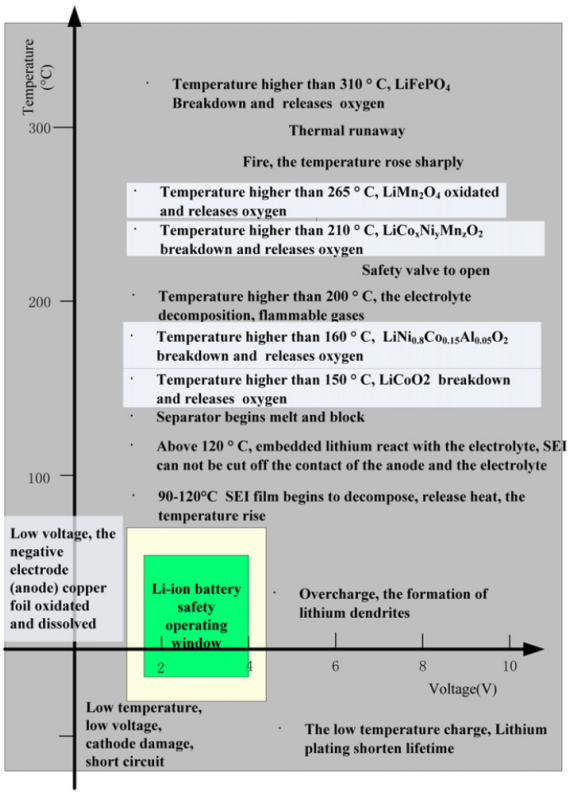

Figure 1.2: Safety operating window for Li-Ion batteries [4]

1.2.1 Grid Energy Storage

Battery systems have grown in interest for utilization alongside the grid in recent years. There are two main categories that batteries are used for: Peak shaving, and frequency regulation. Of course they could be used for backup power when the grid shuts down, but this is very uncommon, so majority of interest lies in maintaining a stable grid via frequency regulation, and peak shaving in times of high demand. Battery backup systems are heavily utilized in commercial applications, however the actual usage is very minimal, and the improvement potential in this application isn't as significant in the applications surrounding peak shaving, and frequency regulation. Each of these application types will be discussed in more detail to understand potential EMS impacts of each type.

Peak Shaving

Peak shaving is a method in which the battery system will be utilized alongside the grid when load demands exceed a preset value in order to reduce the demand required from other

energy sources in the grid (e.g. Power plants, renewables, etc.) [5, 6]. Figure 1.3 shows the typical load profile that would be seen from the EMS to decide when the battery system could be utilized to peak shave [5]. In the figure, the red region shows times at which the battery system would supply energy to the load to reduce demand from the grid, while the blue region shows time where the grid is supplying excess power to the load, at which the battery system could utilize this excess power to recharge the system.

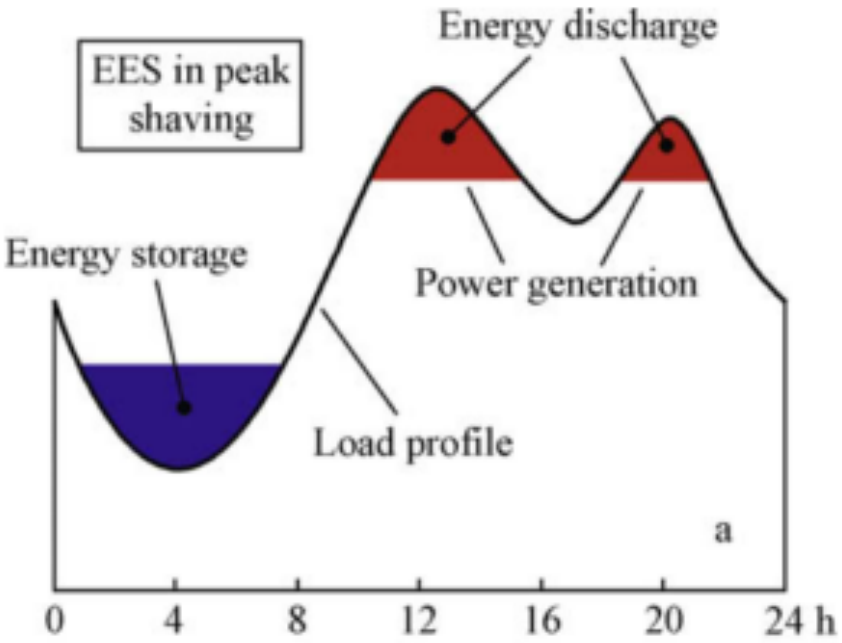

Figure 1.3: Load profile for peak shaving opportunities [5]

The control methodology for how the EMS will integrate the battery system alongside the grid power to supply the load demand is critical to have effective and efficient system performance. Figure 1.4 shows the schematic of interaction between the EMS controller, battery system, grid, and load components [6]. Note that the red lines indicate power flow connections, and the black lines indicate control signal flow (no power transfer). Understanding how the grid load is effected by the battery utilization is critical in load scheduling. The value at which the battery system peak shaves is entirely user choice and application specific, however the value that is used is significant to making sure that the battery system is properly sized to be able to support the load for the required time of the discharge event.

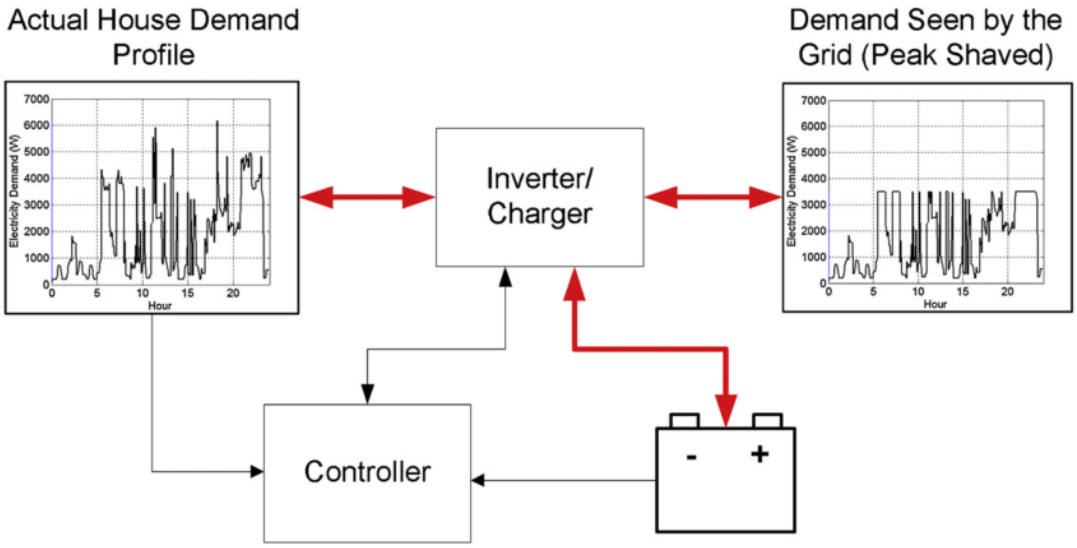

Figure 1.4: Schematic of system for peak shaving [6]

Frequency Regulation

Frequency regulation is often performed on the grid level with generators at the MW scale, and with the reduction in price of Li-Ion batteries, the integration of battery systems for frequency regulation is of growing interest [7, 8]. Frequency regulation is essential to maintain stable operation of the grid across the country, and ultimately the world. Utilizing battery systems is a viable candidate to maintaining grid stability. Figure 1.5 shows the difference between a grid operating on its own, and a grid operating with a battery system acting for frequency regulation [7]. Note that when the battery system is employed alongside the grid, the overall stability of the grid looks significantly smoother for the first 1,000 seconds where the batteries are utilized. Looking at the lower plot in Figure 1.5 it should be noted that after 1,000 seconds, the frequency becomes more oscillatory and eventually can become unstable when the batteries are no longer regulating. The lower plot directly shows the significance of grid energy storage, and more specifically the improves stability by utilizing the concept of frequency regulation. The system shows improved stability when the energy storage is regulating the frequency, then when the energy system is disconnected, the grid stability oscillates much more significantly than the time when the energy storage was active.

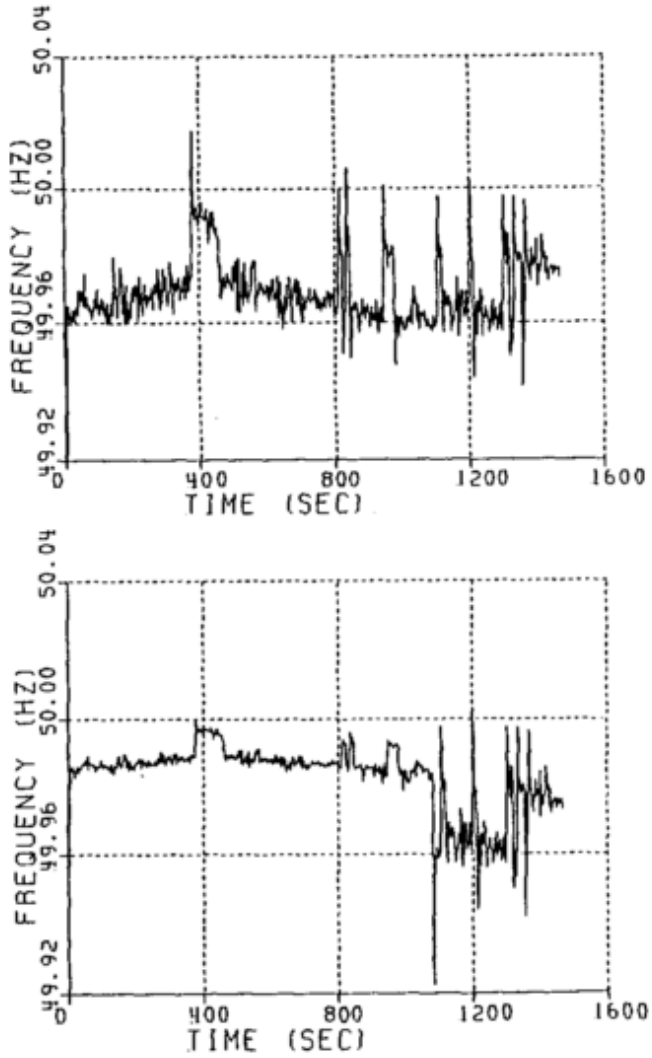

Figure 1.5: Frequency response when battery systems are not used, and when the batteries are used to regulate frequency [7]

1.2.2 Automotive Energy Storage

The automotive industry has many applications of battery systems ranging from small starter battery systems all the way to full electric vehicles. Figure 1.6 shows a number of commercially offered vehicles with different levels of vehicle electrification and the resulting carbon emissions for the vehicles [9]. A study showed that approximately 24% of the global carbon dioxide production comes from the transportation industry [10]. The amount of vehicle electrification can result in significant reduction in emissions, as seen in figure 1.6. Taking a more in depth look to each of these electrification levels are important, as each respective level has their own EMS strategies in the vehicle.

Understanding the various different types of vehicles on the road is an important first

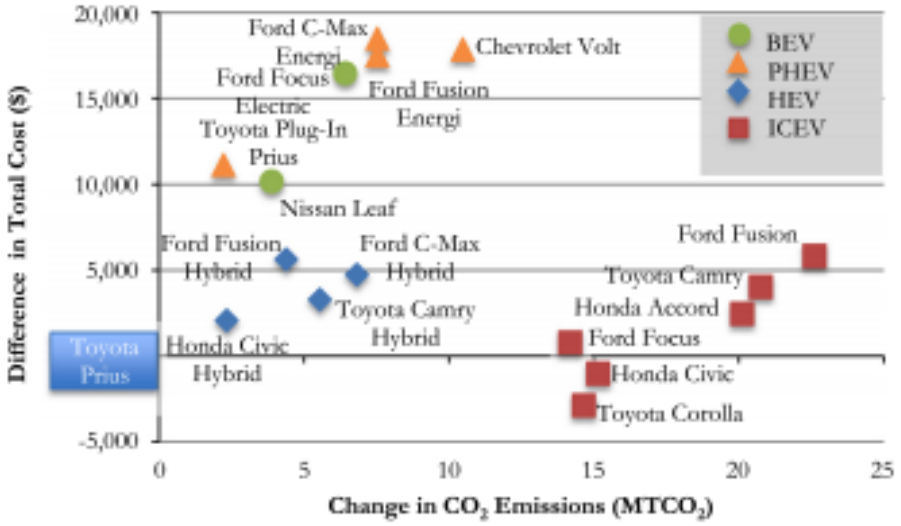

Figure 1.6: Comparison of vehicle cost to emissions [9]

step to designing the EMS. In subsequent sections, the different types of vehicles will be discussed more in depth, but the schematic difference in the vehicles is shown in Figure 1.7. Note that moving left to right from a to g, the vehicle electrification is increasing, which ultimately means that the size of energy storage would need to increase along this axis in order to maintain similar range as the traditional ICE vehicle.

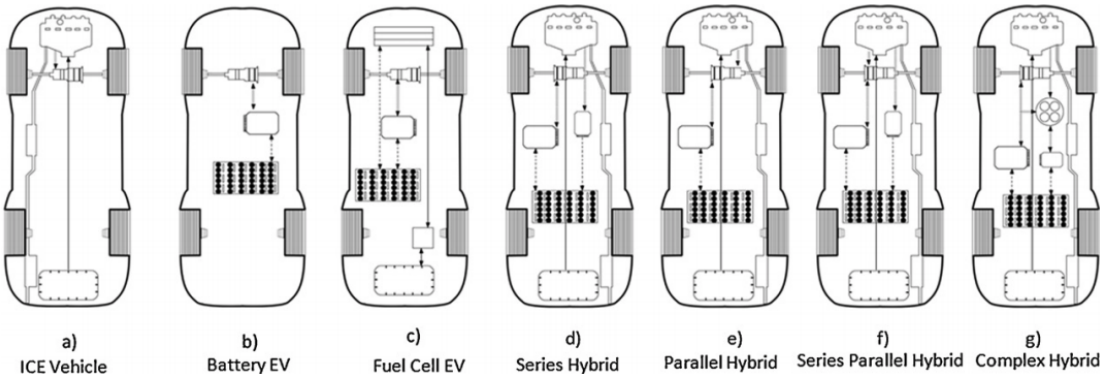

Figure 1.7: Schematic drawings of different types of vehicles [11]

Hybrid Electric Vehicle

HEV's offer a low cost addition to standard vehicles, while allowing improved performance [9, 10, 12–14]. HEV's can be mainly classified into four different areas: Series Hybrid, Parallel Hybrid, Series-parallel Hybrid, and Complex Hybrid. Figure 1.8 shows

the functional block diagram to show the comparison between the four HEV methodologies [15].

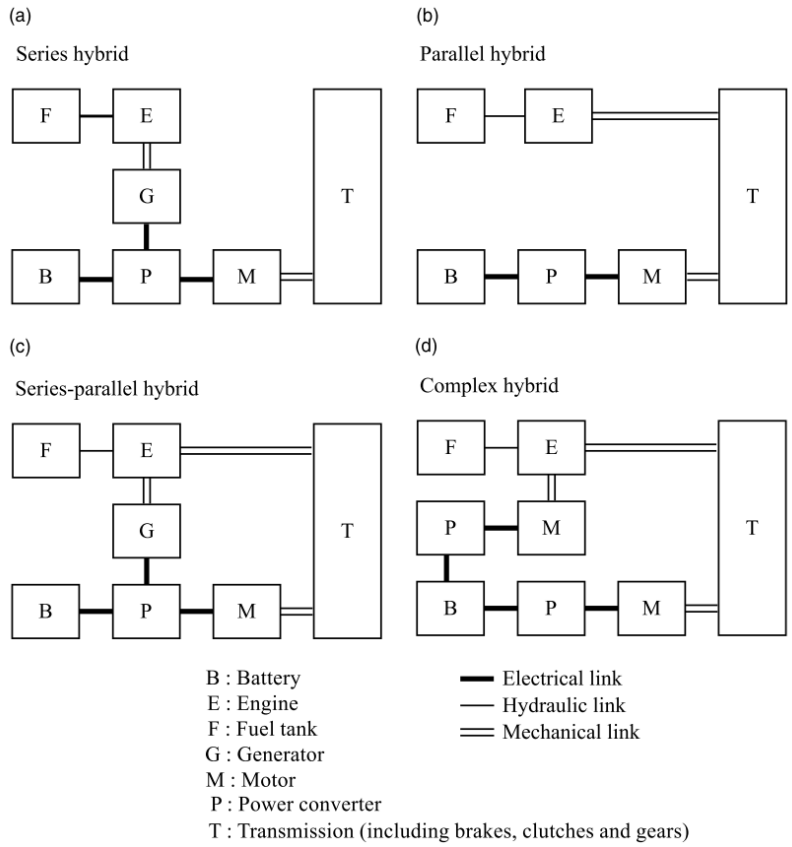

Figure 1.8: Classification of HEV's [15]

For an HEV application, the battery system does not experience a full 100% DOD, which would result in different aging mechanisms, but more importantly, different EMS control strategies/algorithms [14]. A typical HEV duty cycle will operate at a nominal value around 50% SOC, and the range of the operating window won't typically extend beyond 80% SOC on charging, and 20% SOC on discharging [14]. This is important to understand, because from the design perspective, the amount of available energy in the battery pack is limited based on the SOC operating window selected. For example, if the operating range is selected to be from 25% to 75% SOC (with a nominal value of 50%), then the useful energy is only one half of the rated energy of the system. Basically, this means that the energy required for the application needs to be multiplied by a factor of 2 so that the size of the battery system is appropriately rated to take account for the available energy in the pack. Subsequently, the size of the pack has to be oversized to meet the electrical needs of

the vehicle, resulting in twice of the volume to store the battery system to meet the design needs based on the operating window of 25% to 75% SOC.

Full Electric Vehicle

Full electric vehicles are unique in comparison to traditional ICE in many different aspects. ICE uses gasoline as its fuel along with a combustion engine for propulsion, where the BEV uses an electric machine for propulsion, but utilizes batteries for the energy supply (or fuel). While ICE vehicles have batteries for traditional starter systems, the energy storage capacity in a BEV is significantly larger than in ICE vehicles. One main difference between BEV and ICE vehicles is the BEV has no tailpipe emissions, which most vehicle companies market as a zero emission vehicle, but understanding the environmental impact for the different types of vehicles is important for comparison. For example, if comparing emissions between BEV and ICE vehicles, it is important to understand the emissions generated in the power plant to supply the power to charge the battery system in the BEV [11, 16]. Comparing the emissions across different hybrid and full electric vehicles is important, but out of the scope for this research. This research is going to focus on the various subsystems, models and algorithms that can be found within the ESS of different classes of vehicles.

Further understanding of how battery packs are utilized in applications vary significantly based on the automotive manufacturer. Table 1.1 provides a breakdown of certain vehicles, additionally showing details for the associated battery pack in the vehicles [17]. As imaginable, the automakers don't divulge significant details for the vehicles themselves, let alone the ESS. Due to this, in depth breakdowns of different subsystems within the ESS isn't feasible. However, a broad introduction to the various systems utilized in BEV's will be done throughout this section to discuss control algorithms, sensors, aging models, thermal management, balancing methods, etc. In following sections, these systems will be broken down, along with significant advantages/disadvantages associated with them when making decisions in order to integrate these systems within a ESS.

Table 1.1: Electric Vehicles with details on battery systems utilized [17]

Model	**Battery Pack**
Toyota Prius (PHEV)	4.4kWh Li-ion, 18km (11 miles) all-electric range
Chevy Volt (PHEV)	16kWh, Li-manganese/NMC, liquid cooled, 181kg (400 lb), all electric range 64km (40 miles)
Mitsubishi iMiEV	16kWh; 88 cells, 4-cell modules; Li-ion; 109Wh/kg; 330V, range 128km (80 miles)
Smart Fortwo ED	16.5kWh; 18650 Li-ion, driving range 136km (85 miles)
BMW i3	22kWh (18.8kWh usable), LMO/NMC, large 60A prismatic cells, battery weighs 204kg (450 lb) driving range of 130?160km (80?100 miles)
Nissan Leaf	30kWh; Li-manganese, 192 cells; air cooled; 272kg (600 lb), driving range up to 250km (156 miles)
Tesla S	70kWh and 90kWh, 18650 NCA cells of 3.4Ah; liquid cooled; 90kWh pack has 7,616 cells; battery weighs 540kg (1,200 lb); S 85 has up to 424km range (265 mi)
Chevy Bolt	60kWh; 288 cells in 96s3p format, EPA driving rate 383km (238 miles); liquid cooled; 200hp electric motor (150kW)

1.3 Battery Metrics

Battery metrics in terms of this research is defined as an all encompassing term for models, algorithms, and sensors that would be used in a system that isn't application specific. In prior sections, applications were introduced with varying EMS objectives and methodologies, but in this section, discussion of EMS components and strategies will be discussed that would be used regardless of the specific application of the energy storage system. In other words, the term battery metric is used to discuss a technology that is application independent, or universally used across all ESS fields.

1.3.1 State of Charge

SOC at its simplest form is a method to track the current state of the battery in terms of its available capacity (or Ah) remaining in the battery before needing to be recharged. In its most simplest form, a current integral can be performed, and normalized with the rated capacity of the battery to give a number as a percent of 100 basis to describe the SOC. There are countless methods in academia and industry to track SOC in real-time, but discussing the main categories of methods for tracking will be discussed here.

Coulomb Counting

Coulomb Counting is a method used by the EMS to calculate the remaining capacity by accumulating the charge transferred in or out of a battery [18–20]. An obvious disadvantage of this method is the need for constant real-time monitoring of a battery's voltage, applied current, temperature, etc. The accuracy of this method comes down to the accuracy of current and voltage sensors implemented in the battery pack, as well as accurate determination of the initial SOC of the cell. One of the major sources of error in this method is the efficiency of the charge/discharge rate. [18] has shown that the C-Rate being applied corresponds to an efficiency for the cell which will be needed to accurately estimate SOC when using the Coulomb Counting method.

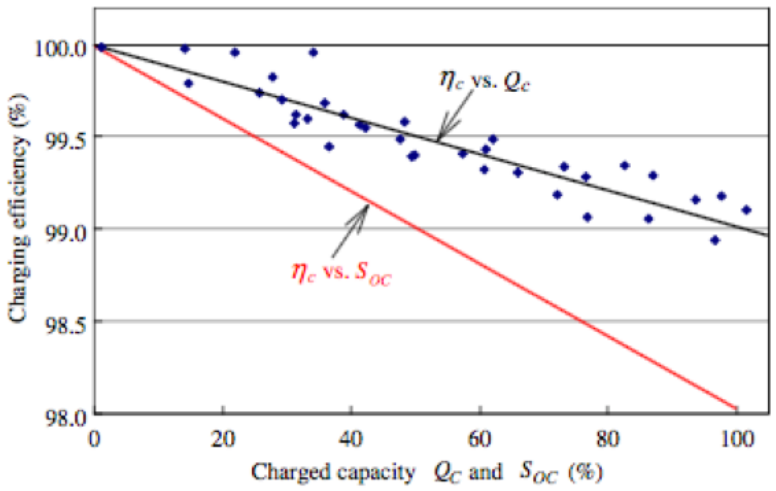

Figure 1.9: Charging Efficiency vs Charged-Capacity or SOC % [18]

Figure 1.9 shows the relationship used in [18] for the charging efficiency with respect to both charged capacity and SOC. The results were obtained by charging cells with a 0.6C-Rate to the designated capacities, and then fully discharging them at a 0.1C-Rate. The efficiency is then calculated by comparing the amount of charge delivered to the cell to the charge discharged from the cell. The charged capacity is converted to SOC percent to obtain the red line in the graph which describes the relationship on how the charging efficiency is related to the SOC of the cell. It is intuitively reasonable that the charging efficiency is reduced as the SOC increases while using the same charging and discharge C-Rate.

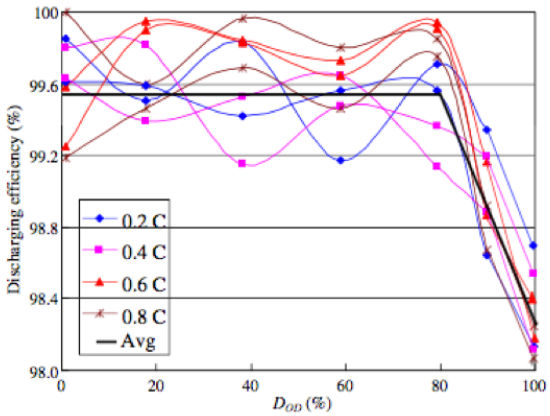

Figure 1.10: Discharge Efficiency under various C-Rates vs. Depth of Discharge (DOD) percentage [18]

Figure 1.10 shows discharge efficiency curves that were experimentally measured in [18] by fully charging cells to 100% SOC and then discharging by a two-stage current profile, first by a specified C-Rate current found in the legend, and then by a 0.1C discharge rate to the cut-off voltage. Then the discharge efficiencies are calculated using Equation 1.1 where I_1, I_2, T_1, and T_2 are the discharging currents and periods during the first and second stages, respectively.

$$\eta_{\mathrm{d}} = \frac{I_1 T_1 + I_2 T_2}{Q_{\max}} \tag{1.1}$$

The results shown in Figure 1.10 show that the discharge efficiency exhibits nonlinear behavior when varying the DOD. According to [18], the optimal rate to implement when targeting discharging efficiency is also dependent on the DOD that will be applied. This

concept is intriguing from an EMS approach, which suggests that a cell chemistry's discharging efficiency could be characterized for a wide range of C-Rates, as well as DOD values, to enable the EMS to select the optimum C-Rate to apply if targeting maximum discharge efficiency.

As discussed previously, the accuracy of the Coulomb Counting method is heavily based on accurate measurements of the charge/discharge capacity (e.g., charge) being transferred, as well as the associated charge/discharge efficiency that is associated with the applied C-Rate [18–20]. If these parameters are identified with high accuracy, the Coulomb Counting method can provide a good SOC tracking method throughout operation.

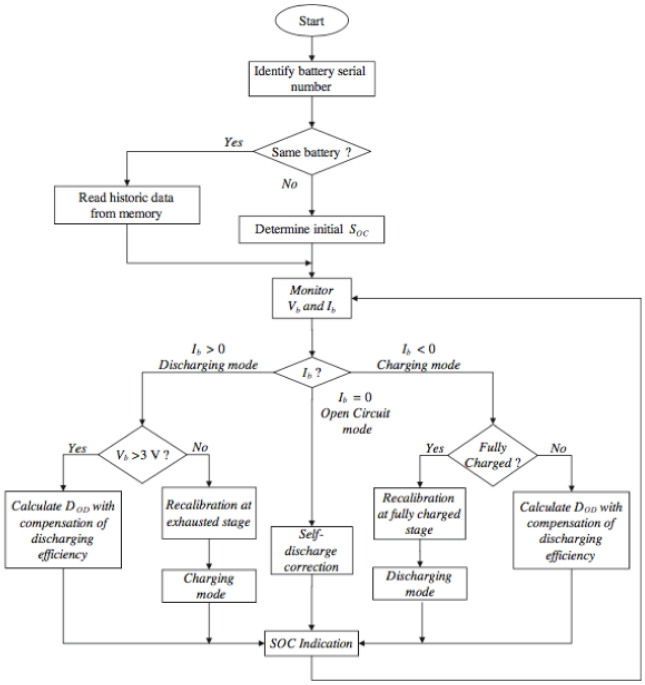

Figure 1.11: Flowchart of Coulomb Counting SOC Estimation Method [18]

Figure 1.11 shows the common flowchart for an EMS that is implementing a Coulomb Counting method for SOC tracking. Note that the voltage values used in the Vb greater/less-than decision block is chemistry-dependent. For systems that contain small numbers of cells, the EMS would be able to implement this flowchart method for tracking SOC. However, as the number of cells increases, the computational power needed to implement this loop for all of the cells becomes progressively more demanding, and could result in more expensive EMS instrumentation to perform optimally.

Estimation Algorithms = Two RC-pair Battery Circuit Model

Examining all of the many different SOC estimation algorithms in the literature would be a major task. However, it is not necessary to look at all of them based on the scope of this research. Nevertheless, it is important to understand the fundamental concepts of the most important and popular estimation algorithms. To do so, understanding the two-RC-pair battery circuit model is essential for developing a fundamental understanding of the many variations in SOC estimation algorithms found in the literature.

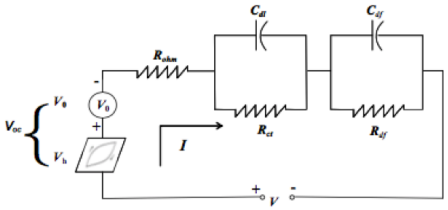

Figure 1.12: Two-RC-pair battery circuit model for a Lithium-Ion battery [21]

Figure 1.12 shows the two-RC-pair battery circuit model that is used as the basis for many estimation algorithms [21–24]. This circuit models the battery as a second-order system, with values for the capacitors and resistors corresponding to the properties of the cell electrochemistry, cell design, as well as cell size. More specifically, in Figure 1.12, R_{ct} is the charge transfer resistance, C_{dl} is the double-layer capacitance, R_{df} is the diffusion resistance, and C_{df} is the diffusion capacitance [21]. The R_{ct}-C_{dl} pair is used to account for dynamics of the double-layer, and the R_{df}-C_{dfpair} is used to account for diffusion [21].

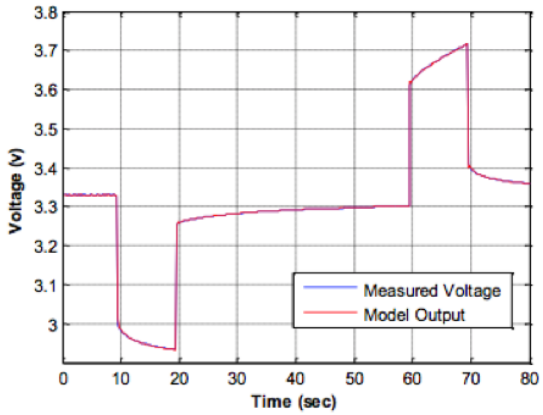

Figure 1.13: Matching of model output and HPPC data for Lithium Iron Phosphate battery at 25°C and 65% SOC [21]

Figure 1.13 shows the results when simulating a battery using the equivalent circuit discussed above, and compares the model output to the measured voltage when applying the same load profile [21]. Examining the plot, the difference between the two results are minimal, and in this case the estimation algorithm is proving to be adequate for on-board SOC estimation by the EMS. Unfortunately, the models become less accurate for more dynamic battery cycles, where the load is constantly changing in small intervals.

A key prerequisite for maintaining accurate SOC estimation is to have highly-accurate measurements of the battery voltage and current during operation. That is, the SOC estimation algorithm can only be as accurate as the accuracy of the voltage and current sensors.

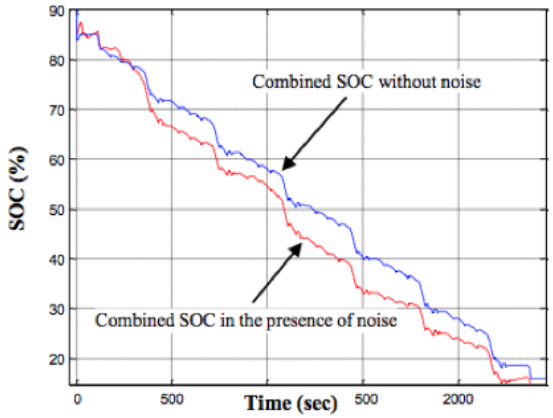

Figure 1.14: SOC estimation in presence of voltage and current noise [21]

In [21], the impact of sensor noise in the voltage and current measurements on SOC estimation accuracy was studied. In terms of EMS performance, understanding how the sensor noise affects other system metrics is crucial to interpreting input data and making EMS decisions. Figure 1.14 compares the estimated SOC vs. time when the voltage and current sensors are exposed to noise with the same SOC estimates when there is no noise present. It should be noted that sensor noises cause errors in the estimated SOC. This implies that an EMS must minimize signal noise in the sensors outputs. In addition, the EMS algorithms for calculating the battery metrics should be designed to be as noise-tolerant as possible to enable the EMS to make proper decisions to achieve the system targets.

In nearly all battery systems today, SOC estimation is utilized for tracking and maintaining EMS performance. Accurate SOC tracking both online and offline are crucial to

maximize performance of the system, as well as to operate the batteries in a safe manner. The performance of an EMS system is closely correlated with the accuracy of the SOC tracking algorithm. As the SOC error increases, the battery may or may not be able to deliver the power that the EMS believes it can deliver. In most cases, this would be detrimental to not only the battery, but the system in which the batteries are utilized.

1.3.2 State of Power

SOP, also known as State of Available Power, provides information on the power that the battery is capable of delivering [25, 26]. To map the available power that can be delivered by the battery, the EMS must first be able to map the voltage profile of the battery at potential C-Rates. The available power from the battery varies depending on the C-Rate due to nonlinear behavior of batteries based on the current they are delivering. There are several methods for mapping the voltage profile of batteries.

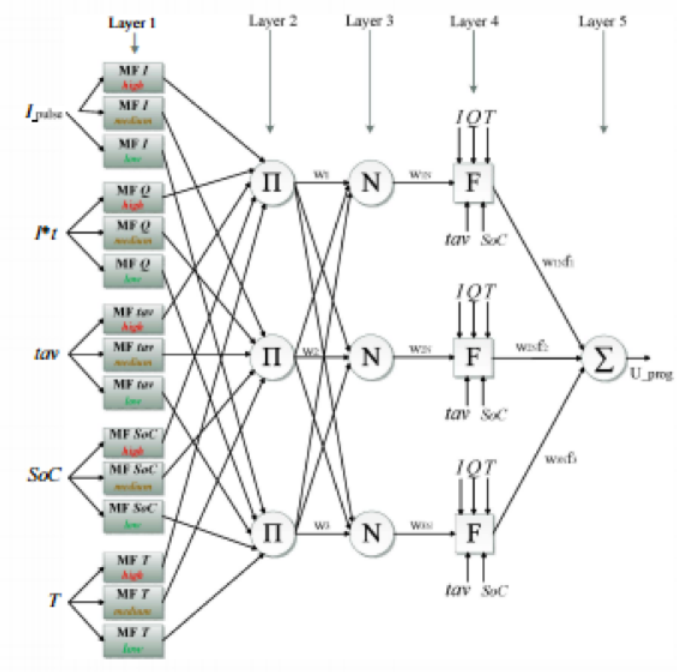

Figure 1.15: Voltage Mapping structure for SOP prediction [25]

One common method illustrated in Figure 1.15 implements a sophisticated method to map the voltage during operation [25]. This method determines the voltage map for the expected range of output currents, and allows the EMS to apply this profile to determine

the available power. Once the available power is known, the EMS can decide whether the battery can accomplish a required task using the SOF metric which is described in detail in Section 1.3.3. Simply stated, SOF gives the EMS a binary answer to the question of whether the desired drive or load cycle can be accomplished by the battery system in its current state. With this information, the EMS can incorporate other models to make decisions on whether to proceed with the applied load, reduce the C-Rate current delivery, or stop operation to protect the battery system.

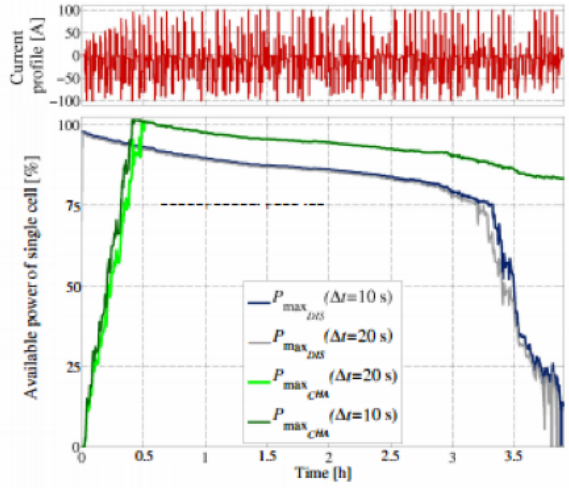

Figure 1.16: State of Power Model Results [25]

Figure 1.16 shows the SOP model prediction results implemented in [25]. Note that there is information provided by the SOP model not only for a single load duration (10 sec), but an extended load duration (20 sec). This makes it possible for the EMS to interpret the capability of the battery system to perform beyond the target region. In [25], the system expected a 10 second cycle duration, and the SOP model also returned results for 20 seconds so that the EMS would have the information it needed to estimate's the battery's power delivery capability if the cycle extended beyond 10 seconds. In cases where the system is fully charged and the load event is small, having this extra information might be unimportant. However, when the applied load is expected to bring the battery system to a low SOC, the ability of the algorithm to predict the effects of extending the load time is essential to maintaining safe operation of the battery system.

1.3.3 State of Function

Technical details of the SOF estimation algorithm are likely to be different for different applications. However, the basic premise of SOF remains the same. The goal of a SOF model is to give the EMS a binary 1 or 0 signal to signify whether the battery can perform a certain duty [27]. The EMS compares the predicted values from the SOP model with the required values and utilizes the SOF model to decide if the current EMS strategy requires updating. In [27] the SOF model determines the capability of the battery to crank the combustion engine after several minutes of engine-off. In this situation, the SOF calculates the minimum voltage reached during simulation of the continuous discharge followed by a cranking pulse. The goal of the SOF is to predict if the battery is still capable of delivering the required power for a defined amount of time.

[28] discusses the major factors that affect the SOF of a battery, which include SOH, SOC, SOP, temperature and terminal voltage of the battery. However, [28] notes that SOF must be tailored to the specific application. High accuracy is required from the SOC and SOH algorithms, as well as the measured battery operating temperature to accurately combine them together for prediction of the SOF.

1.3.4 State of Health

SOH can be defined as the relative performance and health condition of a used battery compared with a fresh new battery. In [29] , SOH deterioration is attributed to irreversible chemical reactions which lead to capacity fading and reduction in the remaining useful life. SOH is a somewhat ambiguous concept, since different manufacturers have their own methods of determining SOH, and there is currently no fixed definition of optimal methods for determining SOH for various applications. With this being the case, defining the SOH for used by the EMS can be interpreted as simply determining the remaining usable capacity of the cell in a way that remains accurate regardless of the cell's age [29, 30]. For the scope of this project, interpreting SOH in these terms is expected to be more than adequate to achieve our objectives.

Understanding the rate of deterioration of the SOH output can give useful insight to the EMS to understand and predict end-of-life of the battery. Determining end-of-life is crucial for an EMS because this can allow the EMS to make control decisions in order to delay the cell's failure. If the EMS has accurate information about SOH, the EMS control strategy can be designed to reduce the rate of the SOH deterioration until the battery can be safely replaced.

1.3.5 State of Energy

SOE can be defined according to Equation 1.2 below by [31–35]. This new metric can be compared to the SOC metric discussed previously in Section 1.3.1. Since SOC is simply the integrated current (e.g., charge) divided by the nominal charge capacity, SOE is a conversion of E_n, the nominal stored energy capacity of the battery, η_e is the energy efficiency, and SOE % is the percentage value (from 0 % to 100%) of the remaining energy in the battery that can be used by the system.

$$SOE\% = \frac{\int_{t_0}^{t_1} \eta_e V(t) I(t) dt}{E_n} * 100\% \tag{1.2}$$

This function is closely related to SOC, but calculated in terms of energy instead of charge capacity, incorporating the voltage profile during operation into the integration term. The incorporation of voltage is crucial to addressing the efficiency of energy stored in the battery. SOC does not take voltage into account, and, therefore, the EMS has no way of determining if the way that energy is being stored in the battery is the most efficient method. By using SOE, the EMS is provided information about the available energy in the battery pack (e.g., vehicle range), as well as information that it can use to evaluate the efficiency of the energy storage in the battery.

Figure 1.17 shows the results for a typical drive cycle for an electric vehicle [36]. The correlation between how the speed of the vehicle translates into the power required from the battery pack shows the need to have a constant power draw function incorporated into the EMS. Since the battery voltage is dynamically changing, determining the resulting current

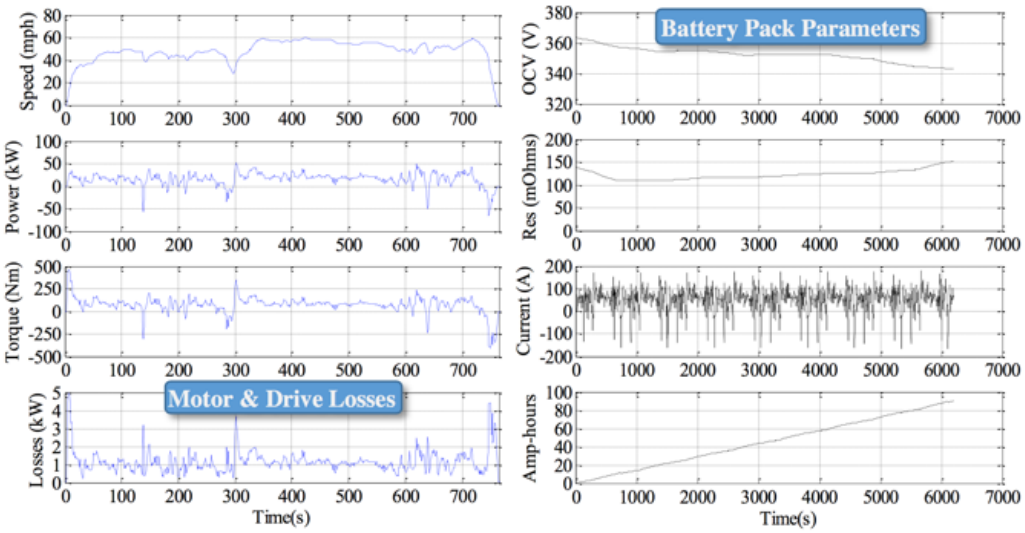

Figure 1.17: Drive cycle profile for an electric vehicle [36]

demanded from the pack becomes a challenging task for the EMS control algorithm. By using the SOE criterion, constant power (the product of the dynamic voltage and current) can be drawn from the battery pack to meet the vehicle requirements. In this case, calculation of the estimated range becomes simpler since the SOE can be easily manipulated to estimate the range based on calculated battery power.

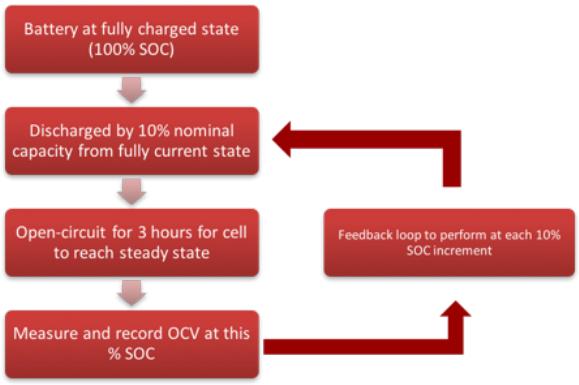

Figure 1.18: Test procedure for OCV experiment [37]

Figure 1.18 shows the test procedure used in [37] to perform an OCV test on a Li-Ion battery. The goal is to understand the impact of the discharged battery energy on the OCV. The cell was discharged by 10% intervals and rested to record the OCV, and measurements for both OCV and the discharged energy were recorded.

Figure 1.19 shows the OCV vs SOC relation during the OCV test performed in [37]. Figure 1.20 shows the relationship between discharged energy and SOC for the same OCV

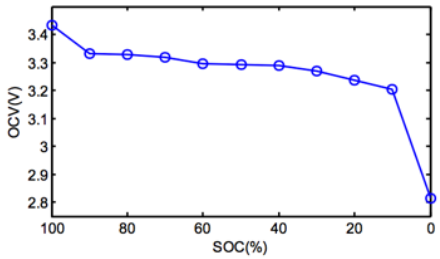

Figure 1.19: OCV test curve showing OCV as a function of SOC [37]

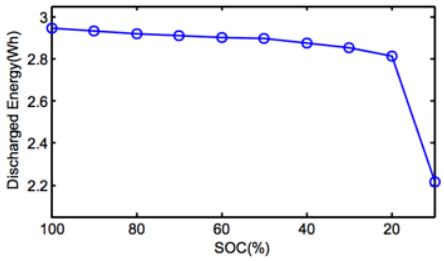

Figure 1.20: OCV test curve showing Discharged Energy as a function of SOC [37]

test. It should be noted that Figure 1.20 plots the discharged energy during each 10% change in SOC. The plot in Figure 1.20 shows that the value of discharged energy is not the same for every 10% SOC window that was tested. For example, from 100% to 90% SOC the discharged energy was 2.945Wh, and the change in voltage was 0.1V. Then for 10% SOC to 0% SOC the discharged energy was 2.215Wh and the change in voltage was 0.4V. It should be noted that both the change in voltage and discharged energy are not the same for every 10% SOC window, which suggests that voltage needs to be incorporated into the model so that the EMS can take advantage of the fact that various amounts of energy can be removed from the system at any given SOC. The traditional SOC metric does not incorporate voltage, and the results from this test show how the voltage input has an influence on the discharged energy.

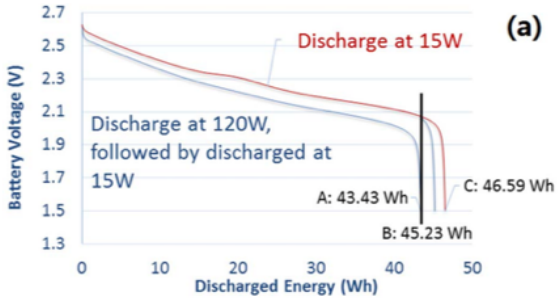

Figure 1.21: Discharge Energy experiment based on power rate [33]

Figure 1.21 shows one of the methods that SOE could be used to characterize the nominal energy of the battery [33]. Much like SOC uses a constant C-Rate current at a low value to determine capacity of the cell as a function of voltage, the SOE metric uses a constant P-Rate at a low value to determine the energy of the cell as a function of voltage.

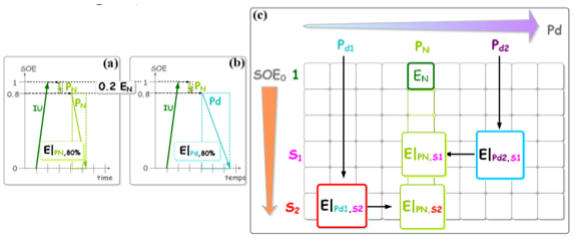

Figure 1.22: Characterization procedure for populating 3-D lookup table for modeling SOE [38]

Figure 1.22 shows the characterization method proposed in [38] for populating a 3-D table for mapping available energy based on P-Rate and SOE percent. The process starts by using a fully charged battery and discharges the battery at a constant P-Rate (nominal rating) until 20% of the rated energy has been discharged. Allowing the cell to rest for several hours, the cell is then discharged at a constant P-Rate (nominal) until fully discharged, and the amount of energy discharged here corresponds to the available energy for 80% SOE at a nominal P-Rate. This same characterization process can be repeated for different SOE percentage levels as well as different P-Rates until all the information needed for operation is acquired.

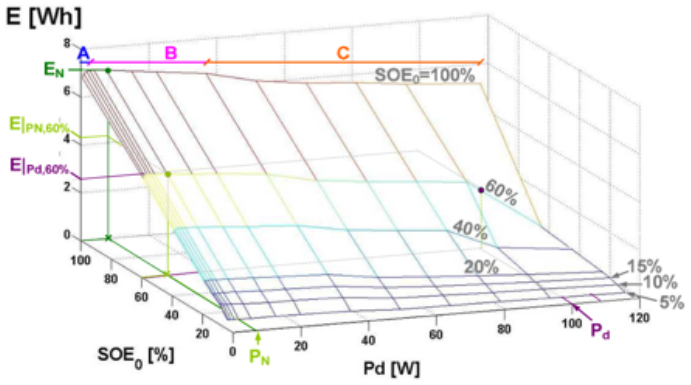

Figure 1.23: Characterization procedure for populating 3-D lookup table for modeling SOE [38]

Figure 1.23 shows the 3-D map generated by utilizing the characterization process described above for [38]. Note that as the P-Rate decreases, the available energy gets larger.

Utilizing this 3-D map, an EMS could determine the range for a vehicle based on the SOE percentage level and P-Rate required. In addition, the EMS can determine the energy efficiency of the P-Rate being used, and make decisions about whether a more efficient P-Rate can be used to boost the range.

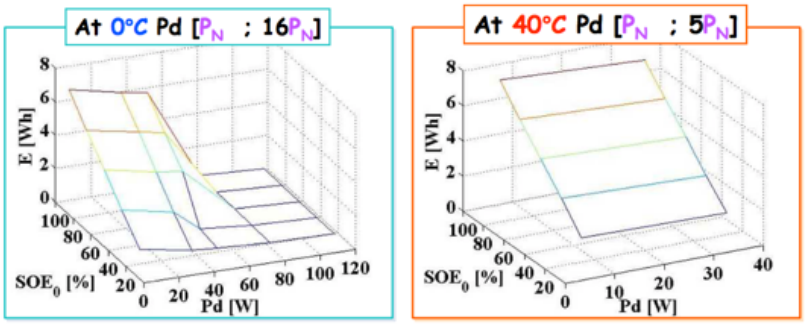

Figure 1.24: Characterization procedure for populating 3-D lookup table for modeling SOE [38]

Figure 1.24 shows the same 3-D map for two different temperatures [38]. This data shows that SOE is a function of temperature, which is also true for SOC. Understanding the temperature effects on the SOE model are crucial for the EMS to fully utilize the power and energy capability of the system. Further work needs to be conducted to study the effect of various battery chemistries on the SOE model characteristics in order to determine the nature of its dependence on electrochemistry.

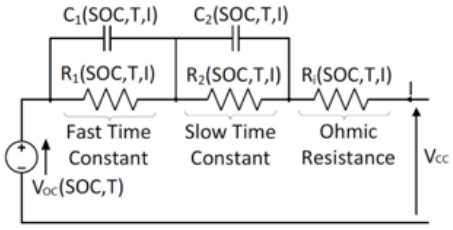

Figure 1.25: 2nd Order equivalent circuit model used for deriving SOC and SOE models in experiment [39]

Figure 1.25 shows the equivalent circuit used in [39] to characterize the SOE metric using an equivalent circuit model, which is a different approach from the integral Equation 1.2 discussed previously. The power integration is one method for offline SOE calculation, but by implementing an equivalent circuit for calculating the SOC, an adjustment can be made to determine the SOE.

Figure 1.26 and Figure 1.27 show the overlaid simulation and experimental results for discharging a cell from a fully-charged state down to its lower voltage limit [39]. Using the

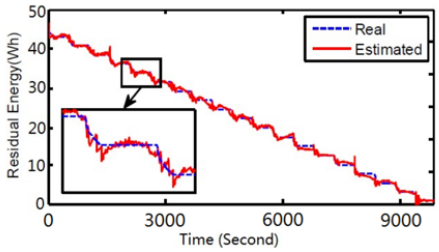

Figure 1.26: Remaining energy in the system during operation both experimentally and simulated [39]

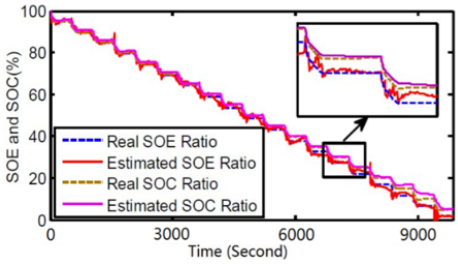

Figure 1.27: Correlation to SOC and SOE by utilizing 2nd order equivalent circuit [39]

equivalent circuit, the results for SOC and SOE can be determined for both the experimental data, as well as the simulated model. The important observation is the separation between SOC and SOE results throughout the drive cycle. At higher energy levels, both SOC and SOE align closer together. However, as the energy is discharged, the separation between the SOC and SOE predictions grows. Intuitively this makes sense due to the additional voltage multiplier inside the integral for calculating SOE which cause a more rapid degradation when normalized by the nominal energy. This separation in data shows the need to model the SOE metric, since the performance characteristics of the SOC and SOE metrics are not identical. Incorporating the SOE metric into an EMS can enhance vehicle range predictions, as well as resulting in more energy-efficient usage of the energy storage components in the system.

1.4 Battery Parameters

This section focuses more on physical measurements that can be made and communicated to the EMS in order to make an EMS decision. For example, Li-Ion requires cell voltage monitoring (for safety concerns), temperature sensors to monitor the battery temperatures locally, and typically a current sensor on each series line. However, the scope of

this research is to study any new sensor technologies that could be implemented to offer the EMS to make better, or more informed control decisions.

1.4.1 Pressure Sensor

There can be multiple types of pressure sensors that can be utilized for a Li-Ion Battery. In subsequent sections, these different ways to measure the battery's pressure will be discussed. As the internal pressure of the battery changes, the exterior casing of the cell will change depending on the type of battery casing used [40, 41]. Since the ideal sensor for commercial purposes would measure externally to the cell, pressure sensor types will focus here on solely measurement types that can be performed without penetrating the cell case.

Battery Dimensional Changes Measurement

Integrating a pressure sensor within the battery pack could offer EMS performance advantages in several areas. Traditional battery systems do not contain pressure sensors, and the investigation of how pressure evolves during battery cycling is relatively undocumented. The closest parallel would be investigation of gassing in cells. However, that study is more focused on the specific gases being generated rather than the physical pressure in the system. For many cell designs, the cell can expand and contract to a degree that external sensors can be applied to the cell to make pressure measurements closely correlated with the internal pressure [40–44]. Understanding how the cell's volume changes throughout the cell's lifetime holds promise for providing the EMS with additional information about the operating conditions of the cell that it can use in combination with other battery metrics such as SOH, SOC, etc.

Figure 1.26 shows the experimental setup used in [42] to take in situ measurements of the battery's volume change while applying various charge/discharge profiles to the cell. Note that this external volume measurement scheme captures information about how the entire cell expands and contracts, and raises questions about how different regions of the cell

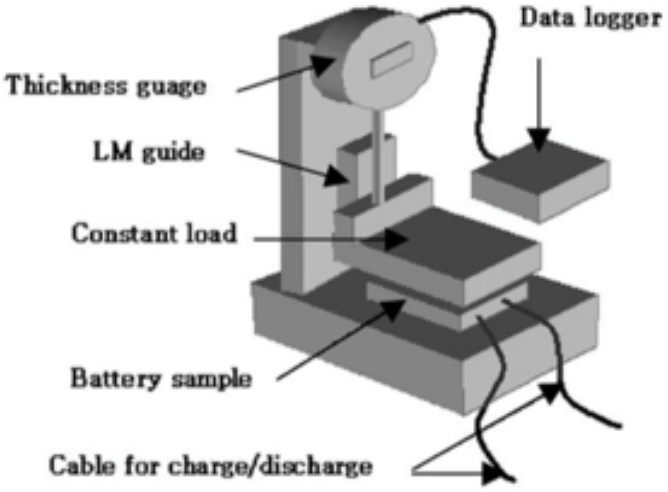

Figure 1.28: In Situ thickness measurement device [42]

expand and contract throughout the cycling. Would localized pressure sensor measurements mounted across the cell surface result in different EMS decisions?

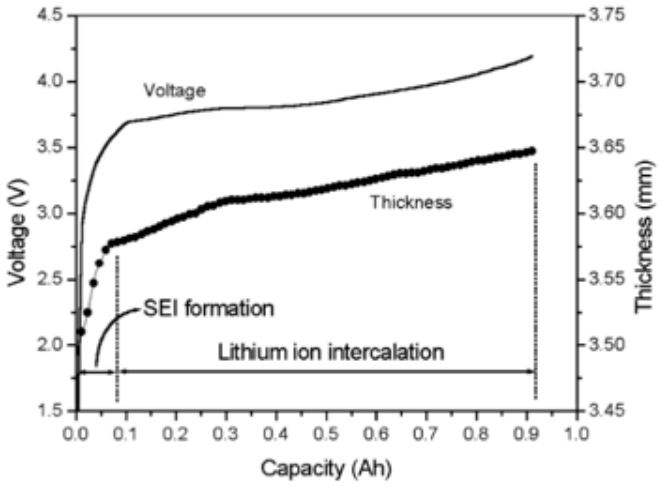

Figure 1.29: Increase of battery thickness during first charge at 0.05C rate of LG's 383562 polymer cell [42]

[42] first discusses applying an initial 0.05C rate to a fresh cell, and uses the test fixture shown in Figure 1.26 to measure volume change throughout this charge interval. Figure 1.29 shows the results of this experiment. The similarity of the measured thickness vs. time profile to the measured voltage vs. time profile is very apparent. These results suggest that volume change information could provide the EMS with additional information for SOC estimation. To utilize the volume change information as part of an EMS control strategy,

the relationship between cell thickness and SOC beyond the initial charge needs to be better characterized.

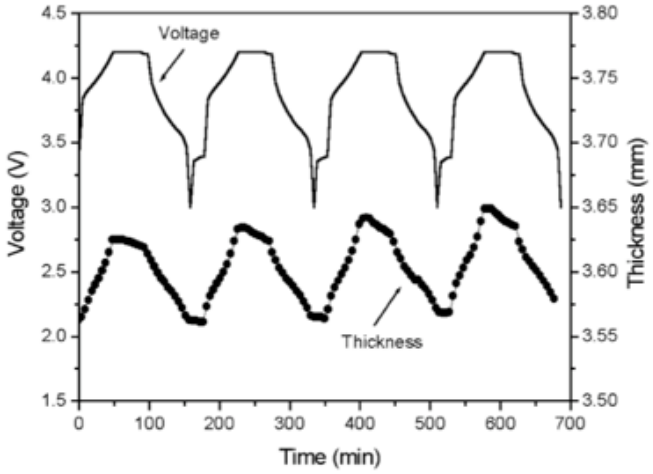

Figure 1.30: In situ measurements of battery thickness during charge/discharge cycles at room temperature for LG's 383562 polymer cell [42]

Extending the experiment beyond the initial charge, multiple charge/discharge cycles were applied to the same polymer cell battery [42]. Figure 1.30 shows the results obtained from this experiment, and the trend that is observed from the volume change again closely resembles the voltage profile of the cell. Seeing this trend raises the possibility of the EMS using the volume change as an additional input into other battery algorithms and models such as SOC estimation, SOH, etc. However, it is important to note that all battery chemistries exhibit different properties, as well as being used in different cell designs. Understanding other aspects of this volume change beyond just this individual case is crucial before the potential of this type of sensor in future EMS algorithms can be confidently evaluated.

Figure 1.31 shows the results of applying the same cycling profile from Figure 1.30 to a different cell design. Note that this volume change once again exhibits correlations with the voltage profile. However, the volume change dynamic response of this cell design appears to be more damped than for the previous cell results in Figure 1.30. This observation stresses the importance of the cell design choice for determining the value of this volume measurement sensor. When integrating this sensor into the EMS, selecting a cell chemistry and design with faster response characteristics is likely to provide more useful information to the EMS controller.

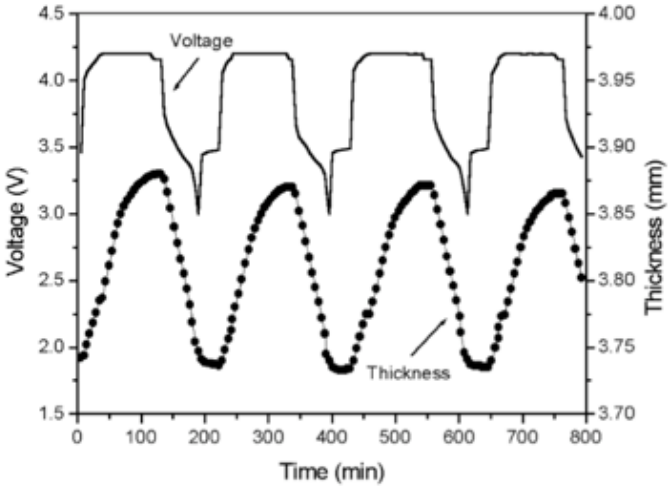

Figure 1.31: In situ measurements of battery thickness during charge/discharge cycles for undisclosed battery manufacturer B in [42] of cell size 383562

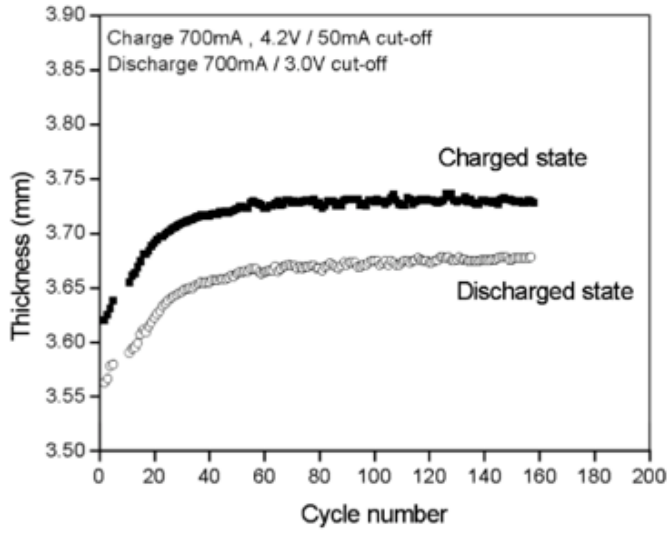

Figure 1.32: Variation of thickness during long cycles for LG's 383562 polymer cell [42]

Figure 1.32 shows the measured thickness measurement in both charged and discharge states vs. cell cycle number. Note that the discharged state means that the cell is at the lower voltage cutoff limit, and the charged state corresponds to cell operating at the upper voltage cutoff limit. The space between two curves represents the cell's volume change envelope during cycling. Examining the trend, the volume change plateaus after the initial SEI formation, reaching a steady-state value after approx. 60 cycles. Understanding how this volume change behaves throughout the cell's life would be of great interest and importance for evaluating the usefulness of this volume change measurement. For example, if the cell volume rapidly expands towards the end of its life, this volume measurement could provide an EMS

with early failure warnings that would improve fault protection of the battery system.

Strain Gauge Measurement

[43] characterizes the pressure relationship of a cell by installing a strain gage between adjacent cell surfaces. The implementation of a strain gage would be simple in large-scale systems. However, the nature of strain gages could also provide drawbacks which must be considered. For example, strain gages secure their readings from very small changes in the strain gage elongation, so a careful examination of the strain gage tolerance would be required before the strain gage reading can be confidently incorporated into the EMS control algorithm.

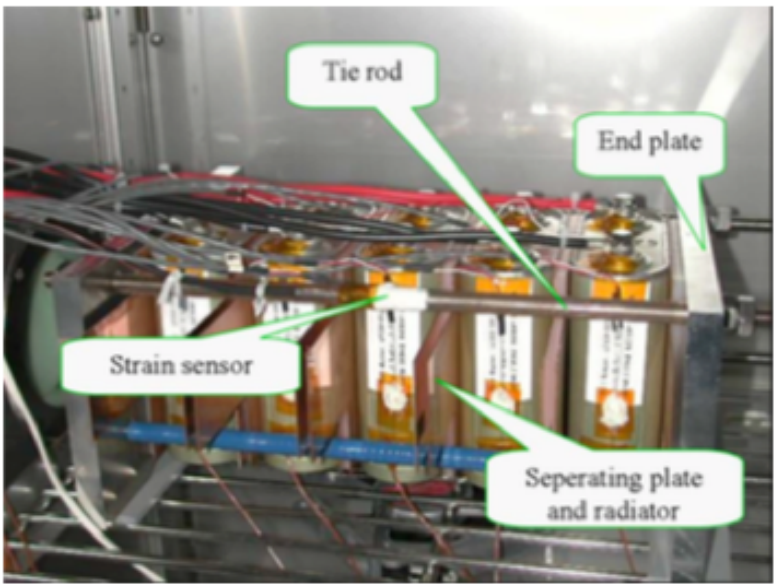

Figure 1.33: Strain gage experimental setup [43]

[43] performed experiments using five 50 Ah-class lithium- ion cells that were connected in series and stacked between two metallic end plates with four tie rods as shown in Figure 1.33. A strain sensor was attached to a tie rod to record in situ the strain change of the cell stack during charging and discharging using an instrumentation amplifier. The cells in this experiment were tightly fixed between the end plates with an initial strain value

of 21 N/cm2. The strain change of the cell stack reflects the cell volume change. An increase/decrease in strain indicates an expansion/contraction of the five Li-Ion cells, respectively. The 50 Ah-class Li-Ion cells in [43] were tested by simulating a spacecraft in LEO operation (Low Earth Orbit) with a DOD of 40% under constant current/constant voltage charge and constant-current discharge conditions.

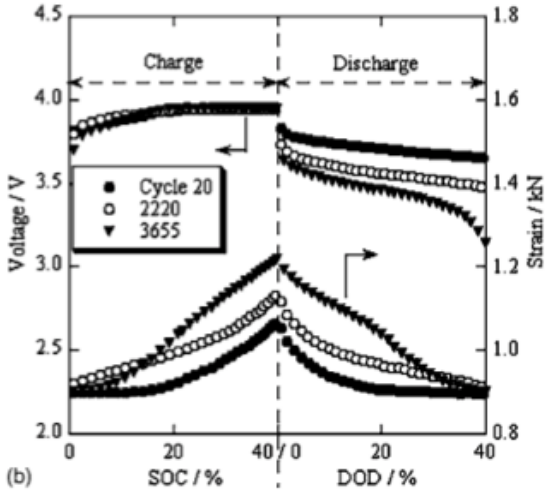

Figure 1.34: Strain gage measurements for selected cycles over cells lifetime [43]

Figure 1.34 shows measured voltage and strain results for a 0.5C charge rate with a taper voltage at 3.95V as a function of the SOC for three cycle numbers on the left half of the figure [43]. Corresponding discharge cycle results are plotted on the right side of the figure. The strain increases monotonically during charging and decreases monotonically during discharging.

It should be note that the voltage at the end of the discharge period decreases with increasing cycle number. This decline in the finishing voltage of the cycle indicates degradation of the cell. The degradation that is observable in the voltage can also be noted in the strain readings for both charging and discharging. [43] suggests that the cell volume change can be explained by simultaneous volume expansion (or contraction) of the anode and cathode in the Li-Ion cell during charging (or discharging) events. Observing this change in strain holds potential for providing valuable information for evaluating the aging of the cell. If the EMS can interpret the expected strain change relationship over a cell's lifetime, the

EMS can use the strain sensor readings to predict the battery lifetime and implement appropriate changes to the cell usage, if needed.

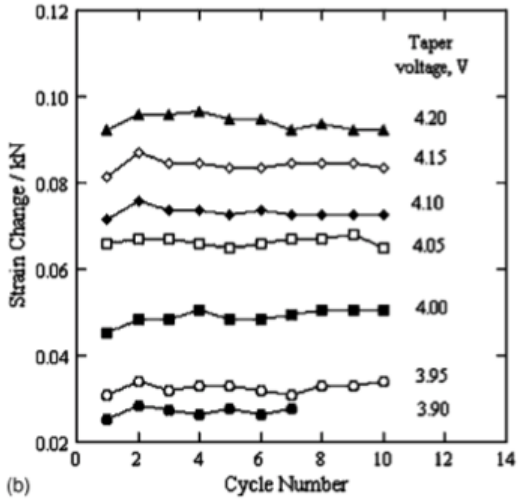

Figure 1.35: Effect of the taper voltage on the strain measurement [43]

Figure 1.35 shows the change in strain vs. cycle and its dependence on the taper voltage value that was applied to the cell during charging [43]. From this data, it can be noted that the value for strain change depends highly on the taper voltage selected. For an EMS, the selection of voltage limits of a cell can affect more than just the energy extracted from the cell or the long-term aging of the cell. Selecting the correct voltage limit also determines the change in strain that the sensor will detect. If an EMS is making control decisions based on these readings, understanding the full significance and tolerance of the strain sensor values is critical for the EMS to make correct decisions.

External Pressure Measurement

As noted earlier in this section, pressure sensors show potential for helping the EMS carry out its analysis and control responsibilities in several different ways. Understanding the different types of pressure readings that can be obtained is important. Previous studies showed measuring volume expansion, as well as measuring change in strain. Finally, a study of the external pressure applied to the cells in a battery pack will be discussed.

Figure 1.36 shows the apparatus used in [41, 44] to apply an adjustable constant pressure to the external surfaces of a cell. For this experiment, commercial 500mAh pouch cells

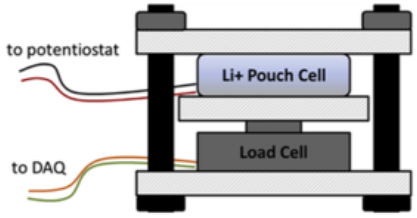

Figure 1.36: Constraint apparatus to maintain and measure compressive stack stress [44]

were used. The battery chemistry was lithium-cobalt-oxide cathode and graphite anode with LiPF6 organic solvent electrolyte. The cells were conditioned with C/2 rate current until reaching a 2.7V cutoff prior to being placed in the test apparatus.

Table 1.2: Summary of cell stack pressures in MPa. Initial is the stack pressure applied before stress relaxation occurs [44]

Stack pressure	Initial	Min	Max
Unconstrained	—	—	—
Low	0.05	0	0.5
Medium	0.5	0.2	1.5
High	5	1	3

Table 1.2 shows the pressure values that were used in the experiment to define low, medium, and high stack pressure values that were utilized in the experiments [44]. The "initial" column represents the stack pressure applied before stack relaxation occurred.

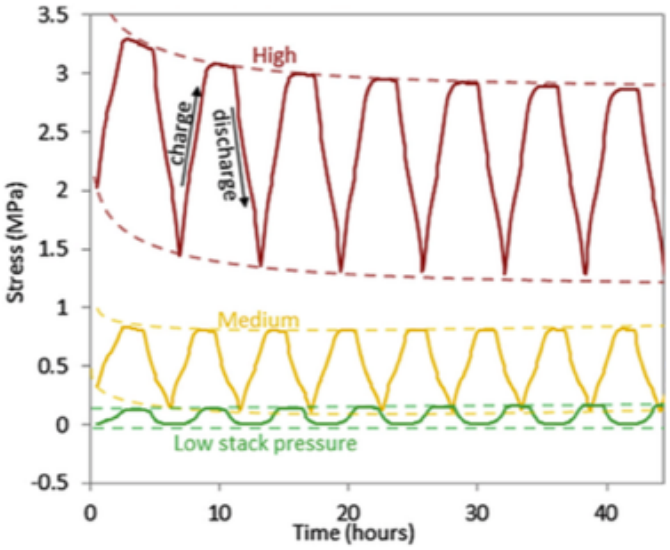

Figure 1.37: Stack stress evolution at early time at high, medium and low stack applied pressure [44]

Figure 1.37 provides results from the experimental test for a series of charge and discharge cycles, showing how the stress measured by the load cell is affected by low, medium and high applied pressures [44]. These results show that the amplitude of the envelope between the upper and lower voltage limits of the cycle grows with increasing applied stack pressure. This feature is important when considering the potential value of these readings to an EMS, since the sensor amplitude change needs to be normalized by the applied stack pressure. In this situation, it would be preferred for the EMS to apply a high stack pressure so that the change in stress is largest, reducing the required sensitivity of the EMS sensor input channel. However, understanding how the stack pressure affects the cell life is important as well in order to avoid premature aging of the cells.

Trends in the Figure 1.37 waveforms indicate that the measured stress is correlated to the cell SOC, as observed with the volume change measurement and the strain gages. As a result, this external pressure measurement technique, like the other two, is a candidate for use in SOC estimation algorithms and, possibly, cell aging estimation algorithms as well.

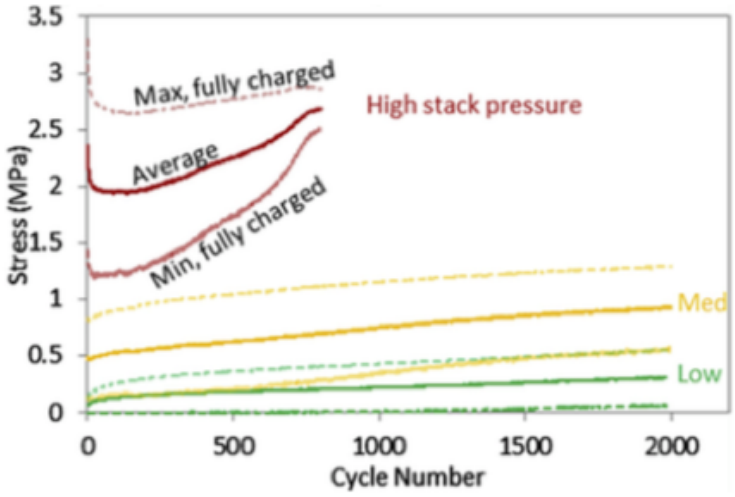

Figure 1.38: Stack stress evolution as a function of cycle number for high, medium and low applied pressure [44]

Figure 1.38 shows data curves for maximum, minimum and average stress results for multiple cells under the same test conditions as a function of cycle number [44]. Examining the results, it is important to note the resulting stress evolution vs. number of cycles for each stack pressure. The cell tests with low and medium initial applied pressure behave similarly in a linear fashion, while the high stack pressure caused early failure. This significant result

highlights the tradeoff that must be evaluated when considering the use of stack pressure as a potential cell parameter. As noted above, high stack pressure amplifies the stress change, but its significant negative impact on cell life is unacceptable. The potential to use low or medium pressure will depend on whether these pressure levels have a measurable negative impact on the cell's lifetime, while recognizing that the measurement sensitivities for these reduced pressures will be lower than for the high pressure condition.

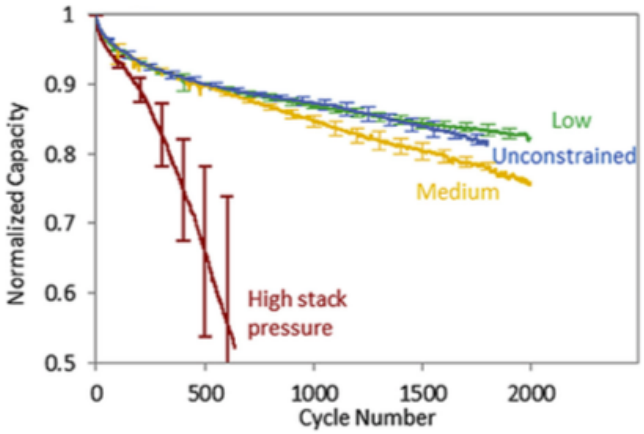

Figure 1.39: C/2 capacity averaged overall 3 cells at high, medium and low applied pressures as a function of cycle number [44]

Figure 1.39 shows the resulting capacity of the cells normalized against each other as a function of cycle number [44]. Since more than one cell was tested for each condition, the lines shown are averaged, with error bars added to show the variation in cell performance among the tested cells. As noted above, it is critical to understand the impact of applied cell pressure on life in order to evaluate the potential usefulness of this measurement technique. This figure confirms that using a high stack pressure will result in early failure of the cell. In contrast, the impact of low and medium pressure conditions on the cell capacity vs. cycle number is much more benign. For comparison, the plotted curves also include one for unconstrained cells in order to provide a baseline for cells that have no external pressure applied. These curves indicate that medium pressure exhibits a rather small but measurable degradation in cell capacity vs. cycle number compared to the unconstrained curve. Interestingly, the cells with low applied pressure actually exhibited high-cycle-number capacity that is slightly better than the unconstrained cells, which could be a statistical anomaly. Most importantly, these results suggest that the use of low to medium applied pressure to enable

external cell stress measurements deserves further consideration as a means of providing improved SOC estimates for use by future EMS control algorithms.

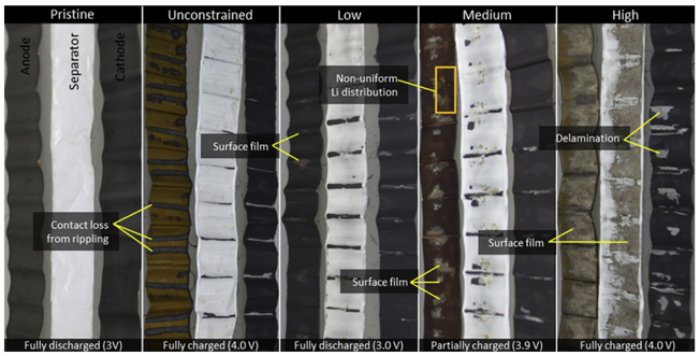

Figure 1.40: Photographs of the disassembled pouch cells showing different types of mechanical stress dependent degradation. The boxed portion underscores an area where the spatially nonuniform lithium distribution within the anode is particularly visible, with black, red, and yellow colored regions in close proximity. Similar lithium distributions can be seen on each face of the partially charged medium stack pressure anode. [44]

Figure 1.40 shows the results of destructive physical forensic analysis on numerous cells in the study [44]. Headings along the top of the figure identify the test conditions for each of the cells, with a "Pristine" untested cell shown at the far left to provide a useful baseline for comparison. Examining the differences in cathode, anode, and separator provides valuable insights into the physical effects of applying mechanical stress on the cell. For high stack pressure, delamination of the cathode material is evident, and the discoloration of the separator show that the rapid degradation on cell performance had a serious negative impact on the electrodes. However, under medium and low stack pressures, the delamination effect is no longer evident, and the electrode surfaces remain much more intact, suggesting that the impact of these applied mechanical stresses on the electrode surfaces is much more benign.

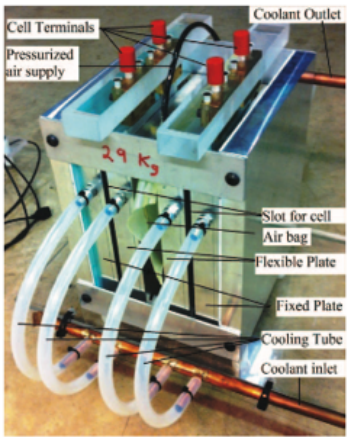

Figure 1.41: Experiment apparatus with fixed pressure between all cells in pack [45]

Figure 1.41 shows the apparatus used to study 25Ah NMC based lithium ion pouch cells [45]. An airbag was placed between each of the cells in the apparatus to maintain constant pressure on all surfaces of the cells. The airbags are all connected to a centralized pressure regulator to maintain a constant pressure value on the surfaces of the pouch cells for the entire experiment. As the cells expand, the airbag self-regulates to maintain a lower internal pressure value, which results in constant applied pressure on the surfaces of the pouch cells.

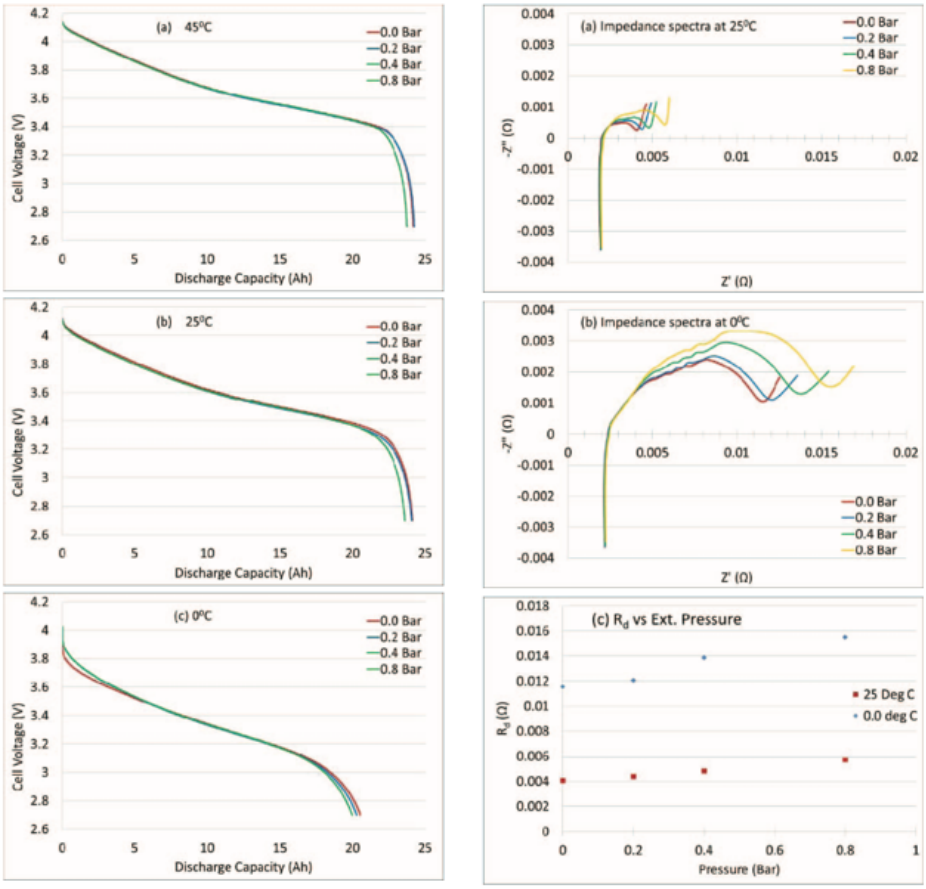

Figure 1.42: Discharge curves and EIS test results for varying temperatures [45]

Figure 1.42 shows results from both a capacity test (left), and an EIS test (right) for the pouch cells shown using the test apparatus described above at three different temperatures [45]. First examining the results from the capacity test, it should be noted that, as the applied pressure to the pouch cell increases, the discharged capacity decreases. This result is consistent with the results of the previous study [44], exhibiting the same capacity trend as a function of applied pressure. However, this study took the experiment a step further by characterizing the capacity effect at different temperatures. As the temperature increase, the

capacities also increase. Although this trend is not a surprise, it is interesting to observe the gradient between delivered capacities as a function of applied pressure across these different temperatures.

Studying the results from the EIS test in the right column, the relationship between measured impedance and pressure is observable. EIS has the potential to provide insights into the cause of the impedance rise from different phenomenon. Understanding that varying temperatures cause variation in impedance level, examining how the impedance is affected by varying pressure shows interesting insight into the electrochemical impacts within the cell with varying pouch cell pressure.

From an EMS perspective, the ability to utilize the information that applied stress can provide has been shown. An EMS could use this type of sensing to help predict other system components, such as SOC estimation, but could be extended to models such as SOH/aging. Selecting the correct applied pressure is crucial to ensure that the EMS interprets the data in the correct way.

1.4.2 Gassing Sensor

Within Li-Ion battery systems, gas evolution does not occur during normal operation. Due to this, gas sensors have not traditionally been implemented into Li-Ion battery systems. Standard monitoring of voltage, current and temperature are adequate but do not detect certain hazardous situations such as electrolyte leakage, or cell venting. If a Li-Ion cell vents, or leaks, the material exposed to a fresh air environment poses a serious fire hazard. Due to this, early detection of these failures is crucial to let the EMS take counter measures to try to prevent events such as thermal runaway.

Figure 1.43 shows the proposed system topology in [46] to implement a gas monitoring system within a battery pack. This type of system detects when a cell has already failed, since the sensors are not internal to the cells themselves. However, this sensor is still beneficial because when a cell fails and vents, the fire hazard comes from continuously

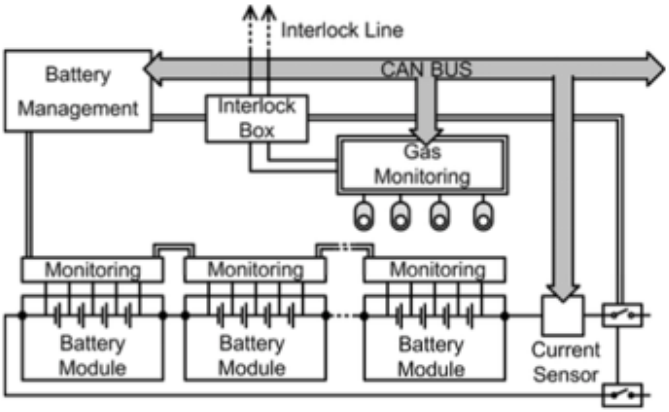

Figure 1.43: Block diagram of a battery system with additional gas monitoring unit [46]

charging/discharging the cell. If the gas monitoring system detects a cell venting, then the EMS can shut down current flow to prevent further damage to the cells.

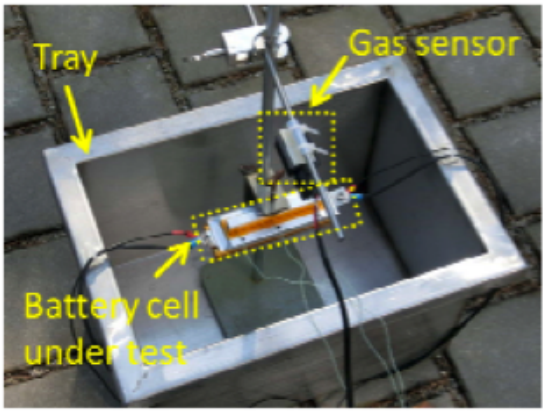

Figure 1.44: Experiment apparatus for overcharge experiment with gas monitoring sensor [46]

Figure 1.44 shows the testing apparatus that [46] implemented to perform a 5C overcharge test. A 5Ah NMC lithium ion pouch cell was used for the experiment. The gas sensor was placed directly above the cell so that when venting does occur, the gas would pass directly over the gas monitoring system.

Figure 1.45 shows the results from the experiment, where the top plot is the data from the gas sensor, the middle plot is the cell temperature, and the bottom plot is the cell voltage data [46]. Two important times were marked on the plots to bring attention to key points in the test that would be useful for an EMS. The first time (cursor 1 = 340 seconds) shows the time that the gas sensor dropped severely in magnitude, indicating that the calibrated gas has been detected. The second time (cursor 2 = 380 seconds) shows the time that the cell began

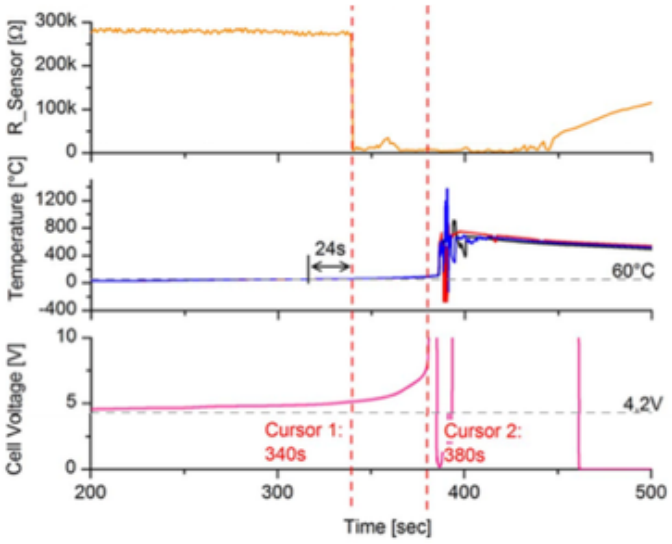

Figure 1.45: Results of 5C overcharge experiment [46]

going into thermal runaway. Between these times the EMS could have had 40 seconds to interpret the data from the gas sensor, and shutdown current flow through the cell. From an EMS perspective, this study shows that implementing a gas sensor could have prevented this system from entering a thermal runaway event. Even though the cell did fail, if the system prevented thermal runaway then this is still a success. Depending on the application, such as an electric vehicle, if a cell enters thermal runaway several people could be seriously injured. Utilizing gas monitoring systems within a battery pack has been shown to be of some benefit to enhancing EMS performance by improving safety and detecting early failures.

1.4.3 Temperature Sensor

For safety concerns, temperature monitoring of the batteries within the ESS is crucial to ensuring that no cell can enter thermal runaway (thermal runaway is a fire type of an event that occurs for Li-Ion when internal temperatures exceed 120 degrees Celsius). In order to monitor temperature, the EMS has the option of employing temperature sensors externally to the battery to monitor the external surface temperature, or design an internal temperature sensor to place within the cell when manufacturing. This section discusses both of these options, as well as potential advantages/disadvantages associated with each sensor type.

Cell Level

Traditional external thermocouple sensors are utilized in monitoring the cell temperature for all cell's in a battery pack. Critical selection for placement of where the thermocouple is placed on the cell will determine how the EMS will make decisions based on the temperature data. A study shown in [47] tackles the issue of optimizing sensor placement on a cell based on the thermal properties of a pouch cell. By placing thermocouples across a cell's surface, they showed the temperature profiles during cell operation.

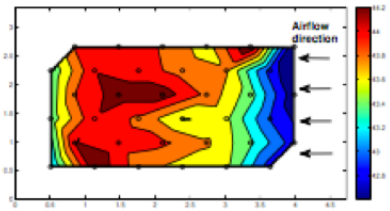

Figure 1.46: Cell Temperature profile during operation for a pouch cell design [47]

Examining the results of the experiment in Figure 1.46 show how the temperature across a cell's surface varies, and that the location that a temperature sensor is placed is crucial for how the EMS makes decisions. Placement of sensors in regions of high temperatures result in the EMS system understanding that this is the absolute high value, and in some cases, will shut down operation prematurely to prevent thermal runaway. Placement of sensors in low to moderate temperature regions can be dangerous as the EMS will never understand the highest temperature of the cell to prevent thermal runaway.

[47] and [48] discuss the performance benefit to the accuracy of cell temperature when implementing more than one temperature sensor. Both papers discuss the optimal placement of a temperature sensor if utilizing one sensor. However, [48] takes this a step further and discusses the optimal location placement of two sensors for EMS performance. If the system has more than one sensor per cell, placement of one sensor in the region of the highest temperatures, and another sensor in the region containing the average temperature in the cell gives EMS the best information for performance enhancement. By having these two sensors, the EMS can use the average value sensor to use this value in algorithms to predict things like SOF, SOP, SOH and other models. While the EMS can use the sensor in the

highest temperature region to protect the system from entering thermal runaway. In this case, having two sensors measuring temperature could prove to have a system performance enhancement.

Cell Internal

Designing an internal sensor for Li-Ion Battery chemistries required several important factors. The first of which is the environment that the sensor needs to operate in. Li-Ion chemistries use inorganic electrolytes that can cause degradation of sensors over time. Since the sensor is exposed to the full chemistry within the battery, the sensor needs to survive in this environment while still providing accurate readings. The second critical criteria are the flexibility of the sensor. Especially in Pouch Cell designs, the ability for the sensor to be flexible as the cell expands and contracts throughout cycling is important.

A fabrication process for designing such a sensor was performed by [49] by designing a flexible sensor material utilizing parylene. They manufactured and calibrated the sensor prior to inserting the sensor internal to the pouch cell.

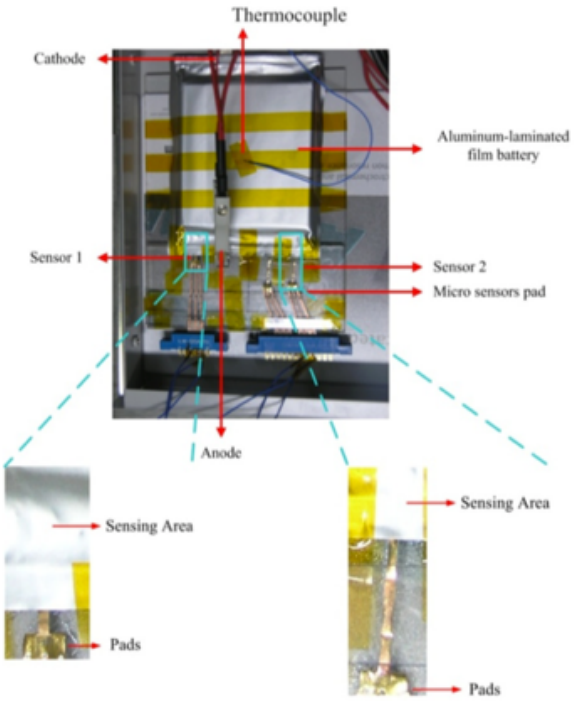

Figure 1.47: Internal Temperature Sensor implemented within Li-Ion Pouch Cell [49]

Figure 1.47 shows the method of which [49] implemented the internal sensor within the pouch cell. For their experiment, 2 internal temperatures were implemented on the bottom edge of the cell on the left and right sides. An external thermocouple sensor was places on the flat surface of the cell in the center where typical systems would measure the external surface temperature of cells.

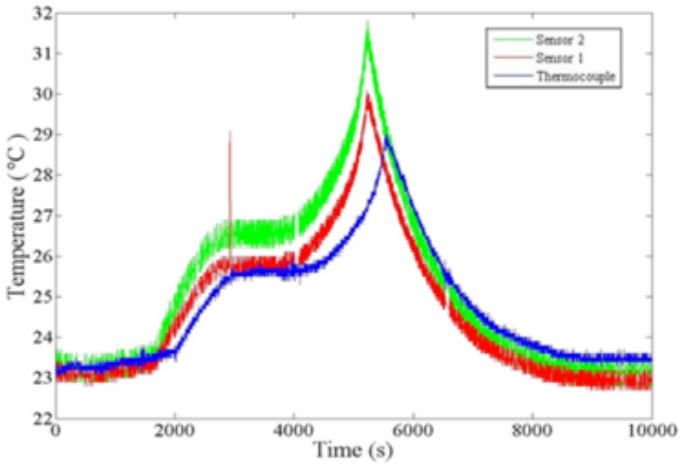

Figure 1.48: Internal Temperature Sensor results for a 1C cycle of Lithium-Ion Pouch Cell with external thermocouple as comparison [49]

Figure 1.48 shows the results of a 1C charge/discharge cycle of the cell design shown in Figure 1.47 [49]. Results show that by measuring internal temperature, not only the magnitude of temperature being measured is different, but the time response for the temperature change is more rapid for the internal temperature sensor.

Understanding the system level benefit of an internal temperature sensor is critical for the scope of this project. Today's energy management systems use the external thermocouple as a temperature sensor on each of the Li-Ion Cells within a Battery Pack. The information that the management system receives is then used to protect the cell from entering thermal runaway. All Li-Ion cells cannot exceed a specific temperature to prevent thermal runaway, so the management system needs to understand what temperature each cell is to shut down operation in situations where the temperature of a cell begins to increase to an unsafe level. The issue with external temperature sensors is that management systems need to take that information and use an algorithm to predict what the internal temperature of the cell would be to determine if the cell needs to be removed from operation. As could be

imagined, in some instances, the cell is shut down prematurely, and the system stopped operation when it was not necessary, but if a management system had more accurate temperature measurements of each cell, the performance of the overall system could be pushed to further limits due to higher operational control of each Li-Ion cell. As shown in Figure 1.48, the internal temperature sensors provide 2 important benefits to an EMS that traditional external sensors do not.

The first performance benefit is the higher accuracy of temperature readings for the internal temperatures of the cell. By having more accurate values to what the true temperature is within a cell, the EMS could push performance further of the system while still operating in a safe region in comparison to measuring external temperature and applying an algorithm to predict the internal temperature value.

The second performance benefit is the more rapid temperature response that the EMS is given for the internal sensor. Examining Figure 1.48 we can see that both the internal temperature sensors show a more rapid response to how the temperature is evolving. With this higher response time, the EMS will be able to push performance further without the concern for the cell temperature continuing to rise after stopping operation.

1.5 Energy Management Control Strategies

Previous sections focused on sensors and algorithms to monitor individual battery performance. This section focuses on the control of the different EMS topologies. The sensors themselves are important for EMS performance, but by employing different control strategies, the overall system performance can drastically be affected, and thus requires an additional consideration in battery pack design.

1.5.1 Thermal Management Methods

Thermal management is perhaps one of the most critical aspects of an EMS, where success or failure of the thermal management can directly result in either safe, or dangerous operation of the battery system. Thermal management systems can be grouped into two

categories, where one is PCM that are modeled as a passive control scheme, while the second group is fluid heating/cooling which is modeled as an active method. Both of these groups will be discussed in detail in subsequent sections to understand the EMS impacts of each group. Traditional ICE vehicles repurpose heat coming off the engine to use as a cabin heater, while when moving into BEV, the luxury of repurposing heat doesn't exist. This results in the need to place a heater device in the vehicle for the EMS to utilize when needed. This results in significant range reduction in regions where large vehicle heating is conducted, such as the midwest in the United States during winter seasons. Focusing on the thermal management systems and how they can be efficiently utilized from an energy demand perspective will be discussed in following sections to understand any ways to mitigate this range depreciation in colder climate regions where BEV's need to utilize additional vehicle heaters.

Phase Change Materials

PCM are classified as a passive control scheme, where the battery pack is filled with a phase change material that completely surrounds the individual batteries. PCM were widely used as a means of storing thermal energy dating back many years, until recently where they were first introduced as a battery thermal management method in 2000 by [50]. Figure 1.49 shows a schematic of how the PCM would be employed in a battery pack. Each numbered cylinder would be a battery (cell) in the pack, and the darker shaded rectangle would be the PCM which surrounds all of the cells in the system [50].

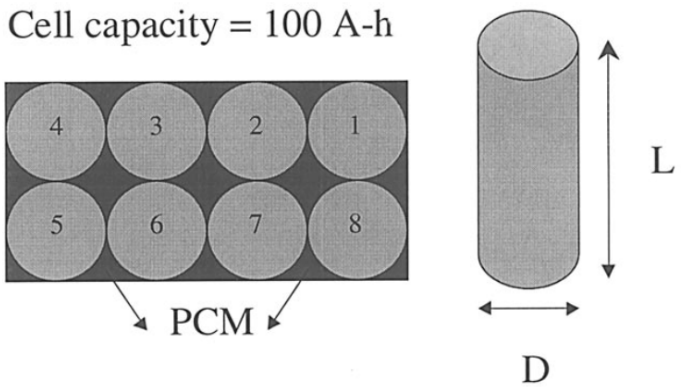

Figure 1.49: Schematic Description of PCM utilized in battery pack where each cylinder is a battery and the surrounding rectangle encompasses the PCM [50]

One interesting benefit of the PCM is that under cold operating conditions, the PCM will store the heat generated from the cells in the PCM after discharge, which will effectively heat the batteries at a higher temperature than the cold ambient conditions, which can result in better energy efficiency in colder climates [50–53]. Other main benefits that can be associated from PCM could be: high compactness, low cost, no need for circulatory network of fans (additionally, no need for space in battery pack to allow air flow), and designed cooling effects [51, 52]. Despite these advantages, the implementation of PCM results in some system drawbacks that would need to be addressed prior to utilization. Figure 1.50 shows a flowchart provided by [51] to address the advantages and disadvantages when using PCM in an EMS. When selecting PCM for a specific application, it is crucial to understand the limit that the PCM can maintain the batteries at a safe operating condition, since the system is passive, it has no way of preventing thermal runaway when this predefined temperature limit is reached.

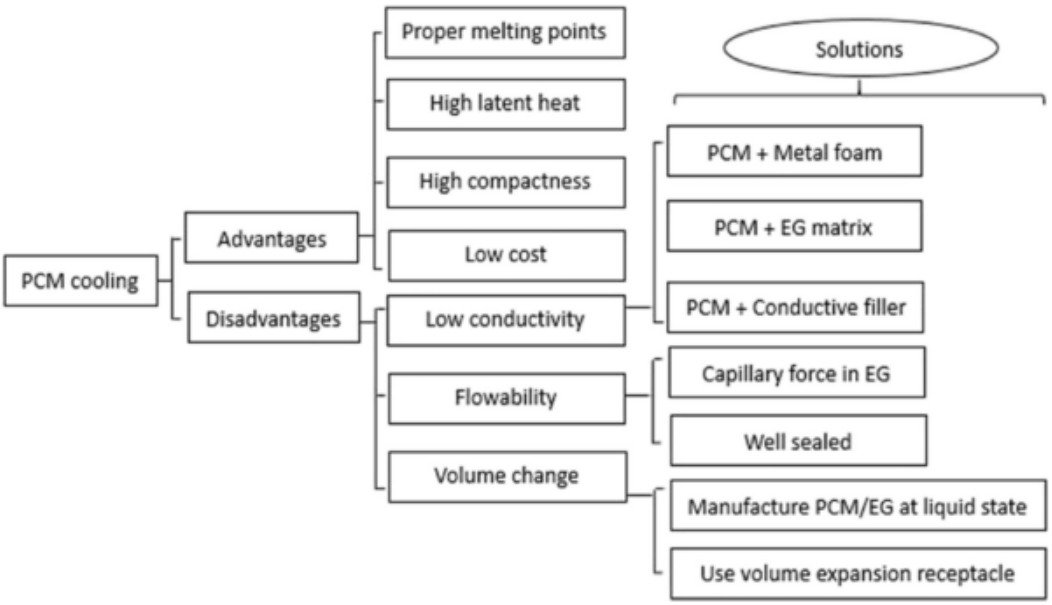

Figure 1.50: PCM Advantages & Disadvantages in EMS [51]

Fluid Heating/Cooling

Fluid heating/cooling takes a more active control strategy in contrast to PCM previously discussed. In this category, heating/cooling methods can be grouped into two categories:

Liquid or air control. Battery systems could be heated/cooled by being submerged in a liquid bath, but more practically, air cooled with fans to disperse the fresh air across the surface of the battery cells. Figure 1.51 shows a schematic of how an air cooling strategy would be employed in a battery system. As seen in the schematic, the flip door valve allows the EMS to have active control of when the battery system needs to be heated/cooled, which gives the EMS capability to dynamically control when the heating/cooling system needs to be used [51–53]. By giving this control capability, the EMS is able to control the amount of energy allocated to the thermal management system, but no matter how often the system is turned on, this type of thermal system will always consume more than the PCM previously discussed. Additionally, the battery pack volume needs to be larger for this type of thermal management system to operate in contrast to PCM, which could pose certain challenges in applications like automotive where volume of systems is limited.

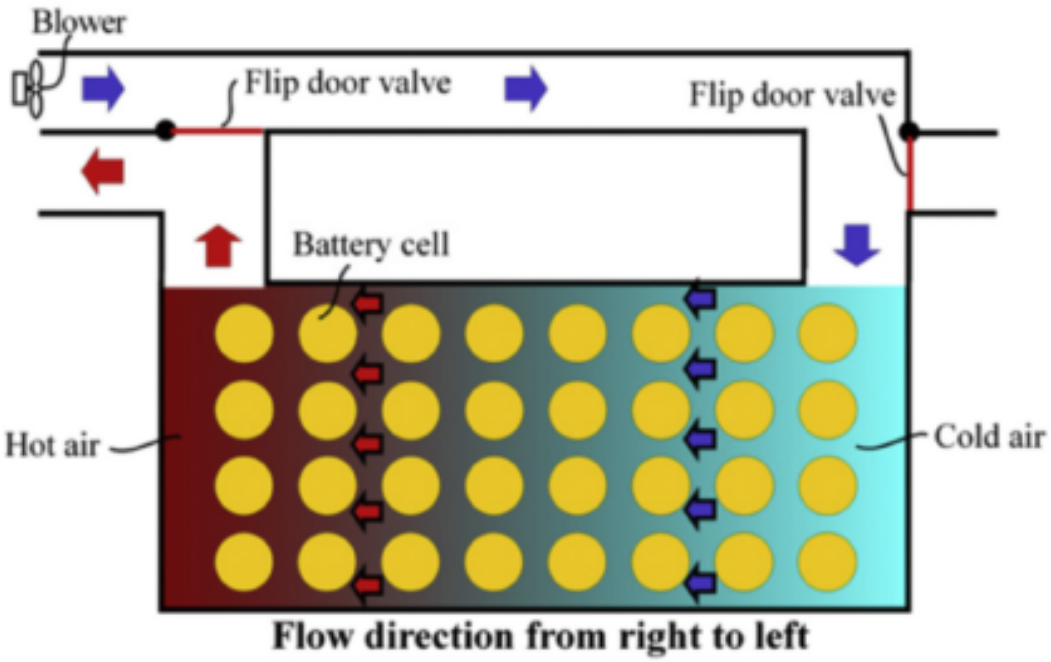

Figure 1.51: Air Cooling schematic for battery pack utilization [51]

1.5.2 Battery Balancing Methods

All batteries have a variance in voltage throughout the entire battery pack that can be attributed to multiple factors. Due to manufacturing conditions, different cells of the same

design might have slight variations in capacity, which will result in slight voltage imbalances as the entire battery pack is discharged [54, 55]. Manufacturers sort cells after a capacity check to place cells with closer exact capacities with each other in order to minimize the amount of cell balancing needed during operation. However, as the cells age over time, the voltage separation increases which results in the demand for increased battery balancing.

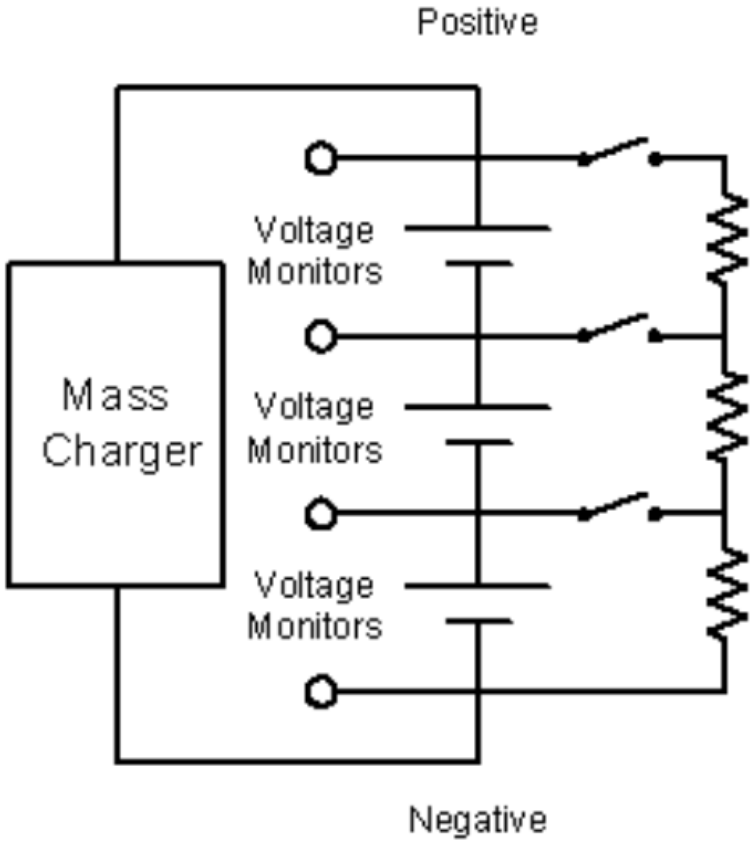

Figure 1.52: Schematic of Resistive Balancing method [55]

Figure 1.52 shows perhaps the simplest (and cheapest) balancing method known as resistive balancing [55]. Essentially the EMS reads the individual cell voltages in the pack, and if the voltages are not aligned according to the application specification, then the EMS closes the switch to the resistor in order to slowly discharge the cell and align the voltages. Note, that this is essentially burning off energy, so this battery balancing method is incredible inefficient, so for applications such as EV's or Grid storage, this method is rarely employed. For applications that require extremely cheap products, this system might be employed to maintain a low cost, while absorbing the inefficiency that comes with the system.

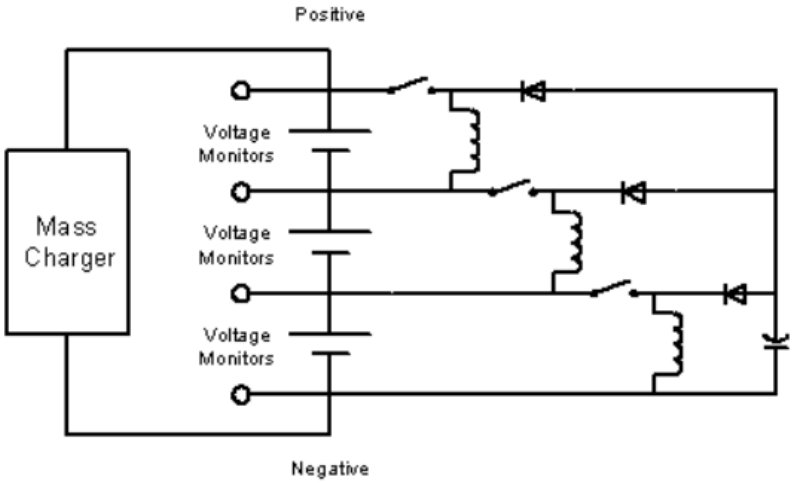

Figure 1.53: Schematic of Boost Shunting Balancing method [55]

Figure 1.53 shows the schematic circuit for employing a more energy efficient balancing method called boost shunting [55]. In contrast to the previously discussed resistive method, in this case the excess energy in cells are redirected by the EMS to essentially charge the cells with lower voltages. Instead of burning off the excess energy in resistors, the energy is utilized to charge the lower voltage cells. While this is a more energy efficient method than the resistive balancing, the energy being used to balance is still lost energy in terms of the load energy seen.

1.5.3 Dynamic Reconfiguration

The concept of DR will be introduced in this section, but an important note should be made before hand. Prior system concepts such as thermal management and battery balancing that have been previously discussed are more small changes to the system and can result in some improvements in system efficiency. DR is a more aggressive system topology change that could also effect significant changes in battery balancing systems, thermal management systems, and other EMS control strategies. However, the overall system improvements evident from DR will be discussed, and if the performance increase is evident, this aggressive topology change would be highly beneficial.

Concept Description

Traditional battery systems comprise of a fixed series-parallel cell topology that is optimized to satisfy current and voltage requirements [56–63]. However, these fixed topologies lack the ability to adapt to dynamic behavior of batteries, especially related to manufacturing difference. As cells are cycled they begin to show separation in performance, and weak cells begin to be identified causing deficiency in performance as well as a cell unbalance issue [56–63]. The concept of DR consists of integrating power electronic switches into the battery pack to replace the fixed series-parallel topology. These integrated power electronics give the EMS the option to dynamically reconfigure the series-parallel topology, thus dynamically altering the battery packs terminal voltage.

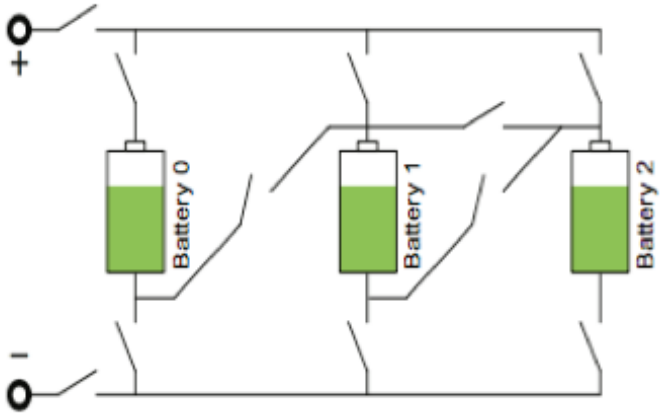

Figure 1.54: Battery Pack Circuit Design with Integrated Power Electronic Switches [56]

Figure 1.54 shows the common battery pack circuit design when integrating power electronic switches. The reconfigurable flexibility of the system is strictly dependent on the number of switches implemented per cell [56]. As more switches are implemented in the system, the number of configurations that the EMS can alter the pack to increases in a non-linear fashion. The task as a design engineer for a commercial manufacturer would be to optimize the configuration flexibility required for the specific application to save money in the system (by reducing the number of switches per cell). By implementing these switches, the EMS earns endless possibilities of which to utilize this new capability to target specific system goals. Some of the main optimization techniques that the EMS can be designed for are discussed in Section 1.5.3.

When examining the potential implementation of this technology, the performance benefit is quite clear as to why this technology can boost EMS performance. However, with this technology a few main drawbacks arise that need to be answered prior to implementing in a commercial ready application. The first is the energy overhead of added electronics. By implementing switches throughout the circuit, the additional energy required to utilize these switches must be accounted for in battery models. Although, the energy consumption of these switches is typically orders of magnitudes smaller than the capacity of a battery. Either way, this energy must be accounted for in EMS models such as SOC, SOF and SOP functions to accurately predict performance that the battery pack can configure. Another potential drawback is the time overhead of reconfiguration. Since power electronic switches are utilized to reconfigure the pack, there is a minimum time the system takes to alter the switch network throughout the pack. While this switching is taking place, the system needs to be under minimum loading, ideally no load, so that the cells don't experience any shorting during switching. However, switching of the configuration can be done at a very fast switching frequency, to perform this under full load considerations the ESS must have an adequate DC bus capacitance to compensate for the time needed for switching. Now, these issues that arise with this added technology are certainly manageable, but certainly must be paid attention to so that a safe and reliable product could be used in commercial applications.

Graph Theory Implementation for Configuration Decision

The application of graph theory can be implemented so that the EMS can determine at any time the optimum configuration based on the load requirements [56]. Applying graph theory to a battery pack we can obtain a weighted and directed graph Equation 1.3.

$$\mathcal{G} = (\mathcal{V}, \mathcal{E}, \mathcal{W}) \tag{1.3}$$

$$\mathcal{V} = n_1, n_2, ..., n_N \tag{1.4}$$

The vertex set $\mathcal{V}$ represents the batteries in the pack, and can denote $\mathcal{V}$ as in Equation 1.4. The edge set $\mathcal{E}$ represents the configuration flexibility of the pack. Figure 1.55 shows the connectivity matrix drawn visually to show the options that a cell would have to connect

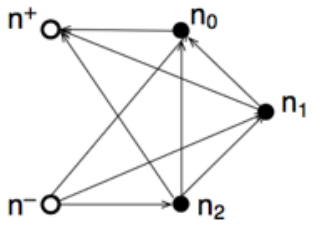

Figure 1.55: Graph Theory Representation of Configuration Flexibility of a Cell in the Battery Pack [56]

with for the configuration found in Figure 1.54. Finally, $\mathcal{W}$ represents the weight of each vertex in the connectivity matrix, meaning the voltage of the corresponding battery at each time instant.

Once this equation is obtained by the EMS, the optimal configuration can be found by using any technique of which the design engineer chooses. Something to note, is that as the number of cells increase in the system, the more useful the graph theory representation becomes. In a small battery pack with 8 cells, it is rather obvious the potential configurations given a low number of power electronic switches per cell. However, as the battery pack gets larger, like in the original Tesla Roadster containing approximately 6,800 cells, the potential configurations are overwhelming even when a low number of power electronic switches are implemented per cell [64]. For battery packs like in the Tesla Model S, this graph theory representation is crucial to allow the EMS to make the optimized configuration choice at a given time instant in hopes to boost performance.

Configuration Optimization Techniques

Since DR has been introduced and discussed in detail from the hardware perspective, discussion on how the EMS will make the configuration decisions is needed. While there are many different ways to control the way the system makes decisions, there are a few that need to be highlighted as signifcant areas investigated in literature.

Minimize Converter Losses for Increased System Efficiency

Perhaps the simplest technique both to implement in a system as well as control dynamically, maximizing the parallel strings in the pack ultimately is reducing the applied current

to individual cells in the pack. The idea behind this is by reducing the current amplitude to the individual cells, not only will they last longer in discharge time, but the cells will degrade at a lower rate.

$$min \frac{\mathcal{P}}{n_p \mathcal{V}_{\text{out}}} \tag{1.5}$$

To maximize the parallel strings in the pack, applying Equation 1.5 along with the graph theory representation, the EMS can identify the optimum configuration for this technique. In this equation, $\mathcal{P}$ represents the power required by the load, n_{p} represents the number of series battery strings that are connected in parallel to supply the load requirements, and $\mathcal{V}_{\text{out}}$ represents the voltage out of the terminals of the configuration [56].

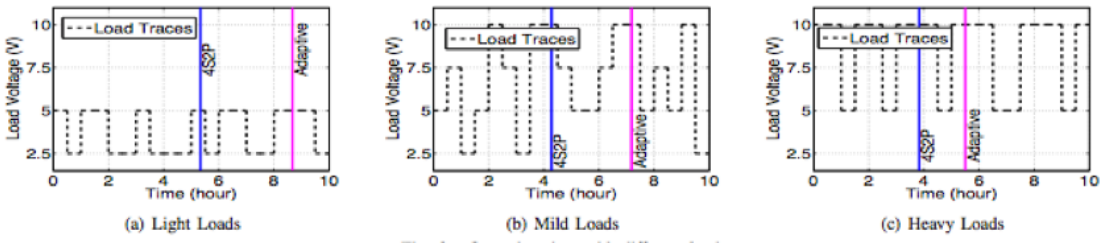

Figure 1.56: Operation Time for DR and fixed series-parallel topologies [56]

Figure 1.56 shows the results in [56] as they applied 3 different load profiles to both a dynamic reconfigurable pack, and a static 4 series 2 parallel (4S2P) configuration. Examining the results, the dynamic reconfiguration design shows superior performance under dynamic loading conditions.

The flexibility for the EMS that this technology provides has potential to the way we design battery systems. Implementation of this technology should keep the volume that the system occupies relatively the same since only the connections between cells are altered. If key obstacles with this technology can be overcame, vehicle applications can make decisions for the energy system as to whether they want to keep the same pack size and take the increased range, or reduce the energy system volume so that it matches the performance of the traditional system. This would then free up space in the vehicle for other systems, or reduction in vehicle size all together.

State of Health Aware Optimization

The concept of State of Health (SOH) aware optimization is to ensure that any usable capacity is extracted from all cells in a pack. For traditional fixed series-parallel systems, the deliverable capacity that the pack can deliver is dependent on the weakest cell in a series string within the pack. Due to manufacturing capabilities, not all Li-Ion cells contain the same deliverable capacity. In addition, not all cells degrade at the same rate, which over time would result in a fluctuation in cell capacities throughout a battery pack [61].

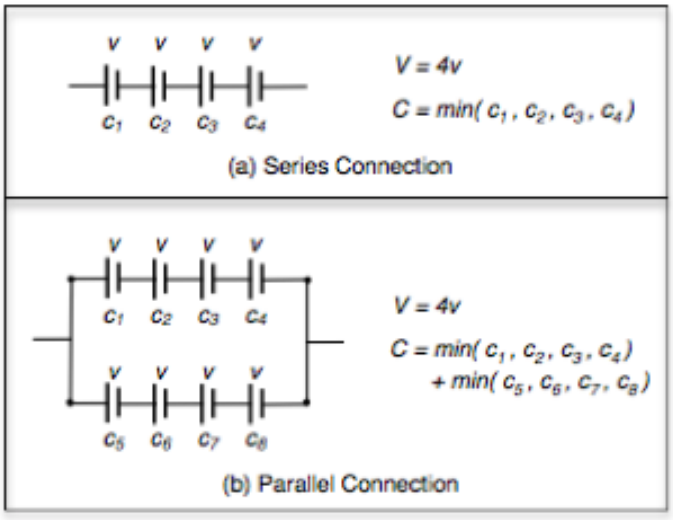

Figure 1.57: Series and Parallel connection of cells resulting Capacity of the system [61]

[61] shows that in Figure 1.57 how the capacity out of the system relates to the cells within the configuration. If the system consists of just one series string, then the capacity the pack can deliver is simply the weakest cell in the system. However, when there are more than one series string, then the pack's deliverable capacity results in the sum of the capacity from each of the weakest cells in each series string.

[61] experimentally studied the effect of SOH reconfiguration, and Figure 1.58 shows the system model that was adapted to test the system performance. For their study, [61] applied a voltage regulator for each series string in the pack to regulate voltage of the string due to voltage imbalance between cells.

The design of experiment can be seen in Figure 1.59 that [61] applied to determining the performance benefit a EMS could receive via reconfiguration optimization of SOH. The

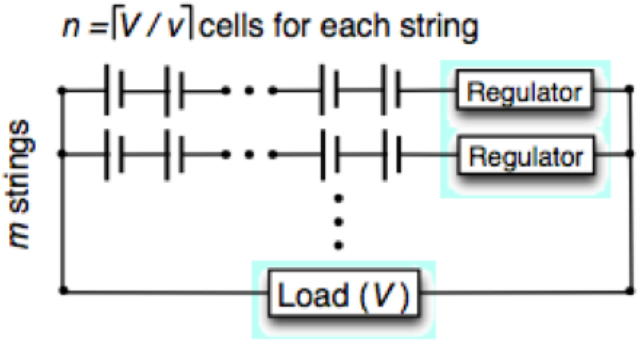

Figure 1.58: SOH aware DR System Model [61]

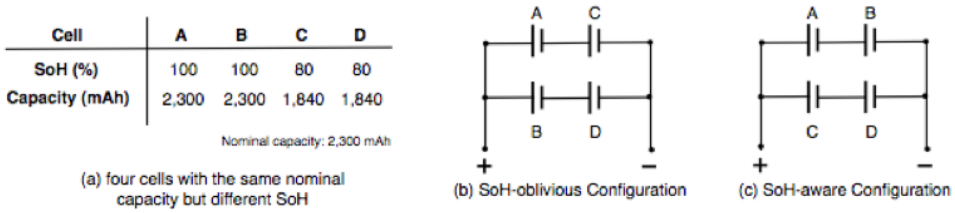

Figure 1.59: Experimental Details of SOH aware Reconfiguration [61]

concept proposed is by grouping cells of the strongest capacity together, and the weaker cells together will result in more usable capacity in each of the strings. Since the deliverable capacity of the series string is dependent on the weakest cell, by grouping the weakest cells in a single string, the extra capacity in the stronger cells will be available to use.

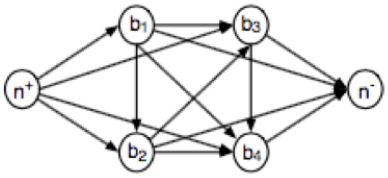

Figure 1.60: Graph theory representation for SOH aware full reconfigurability of experiment with 4 cells' in a battery pack [61]

Figure 1.60 shows the graph theory visualization for the battery system used in [61]. In this case, full reconfigurability is available to the EMS since there are only 4 cells in the system. For this case, grouping of cells in 2 series 2 parallel configurations are the only option, but the selection of which cells are in each string is subject to EMS decision.

Figure 1.61 shows the results when experimentally testing the 4-cell battery pack under 2 different conditions. The first condition is a SOH oblivious pack, or more understood as a fixed series-parallel configuration that is traditionally used. The second condition is a SOH aware reconfigurability system that is being studied in [61]. The results can be seen

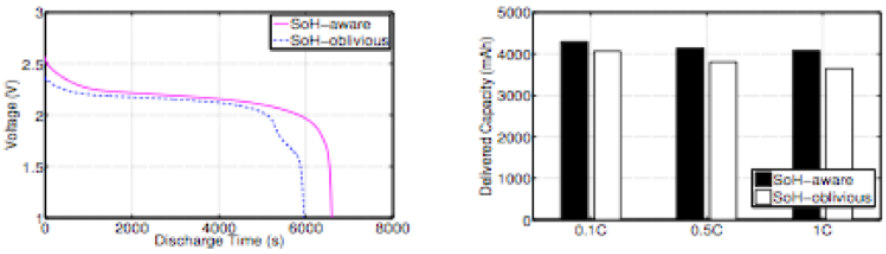

Figure 1.61: SOH aware reconfiguration experimental results [61]

that in all cases of C-Rate used, the pack that is reconfigured with SOH in mind results in a higher deliverable capacity. In addition, the voltage profile throughout the discharging event is altered from the system level, and needs to be considered for the EMS to understand the optimal decision strategy.

Cell Failure Optimization

Handling faults within the system is essential when dealing with the voltage and power capabilities of larger sized energy systems. For vehicles like a Tesla Roadster, the battery pack consists of approximately 6,800 cells [64], and when a cell fails the ability of the system to handle that issue is crucial to vehicle performance. If a cell fails in the Tesla vehicle, in some cases the entire series string becomes unusable, and in other cases the entire pack needs to be shut down to prevent unsafe operation. Implementing a reconfiguration network with faulty cells kept in mind is another optimization strategy that is crucial for long term battery pack utilization.

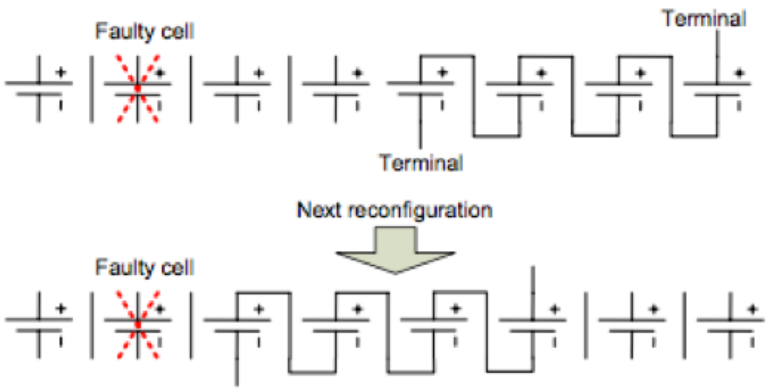

Figure 1.62: 1 series string reconfiguration for a faulty cell within the system [63]

[63] explored the potential of utilizing dynamic reconfiguration for handling when a cell fails within a battery pack. Figure 1.62 shows the initial ideology for when the EMS detects a fault, how the reconfiguration can re-design the series-parallel topology to remove the faulty cell from the network. However, this has several system performance impacts, in this case the system loses more than just the faulty battery. Depending on the configuration flexibility and the location of the faulty cell, the resulting impact could be detrimental to the system performance. Although, it should be noted that even if the performance is drastically impacted in the system, this would still be more performance that can be extracted from the battery pack in contrast to cell failure in traditional fixed series-parallel topologies.

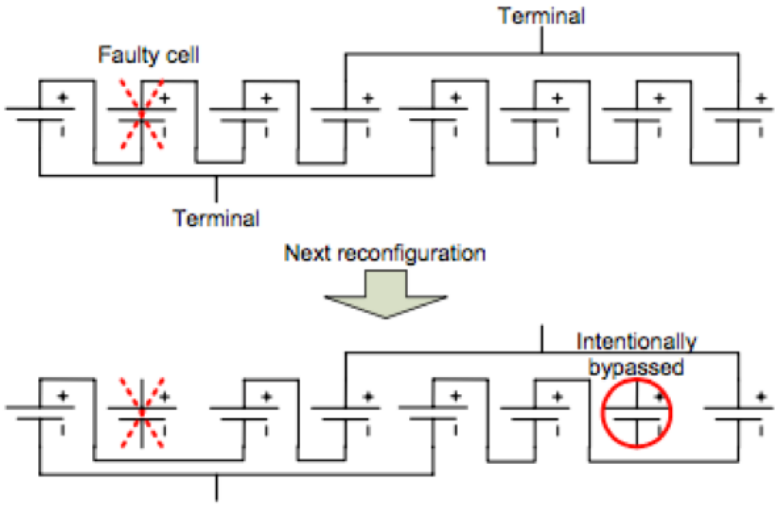

Figure 1.63: Faulty cell reconfiguration with more than 1 series string [63]

Figure 1.63 shows the final approach that [63] took to optimize the performance capability of a battery pack when a cell failure occurs. This is crucial though, to understand that the reconfiguration flexibility is crucial when a cell failure arises, and depending on the flexibility and the location of the cell failure, the resulting configuration options are selected by the EMS. Ideally, the cell failure would be a location where the reconfiguration flexibility allows to utilize all the remaining cells and allow parallel strings to ensure the system requirements for both voltage and capacity.

Reconfiguration Assisted Charging

If a reconfiguration network is applied to a system, the ability to more efficiently charge the system needs to be explored. In [58], a study on how to more efficiently charge a battery pack was performed in comparison to utilizing a traditional commercial charger. Due to cell imbalance in a system, battery balancing throughout operation is crucial to maximizing the efficiency of charging so that the pack can deliver the most capacity on a consistent basis.

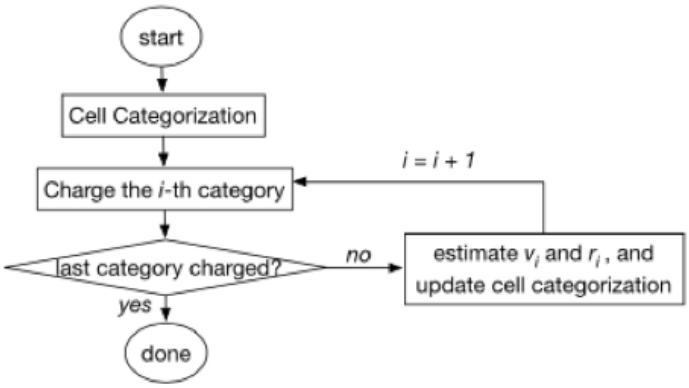

Figure 1.64: Flowchart for reconfiguration assisted charging [58]

Figure 1.64 shows the EMS decision flowchart that would be used in reconfiguring the battery pack and charging process. [58] proposes a category by category charging method, which consists of grouping the cells by a graph theory representation of cell voltage. The flowchart consists of charging a specific category, and for the method selected in this study, an example of this could be a group of cells with the same OCV. Different categories would be dependent on the separation of OCV's of all the cells in the system. However, this method might require a longer time to charge the system, but the results shown in this study suggests a more energy efficient process to ensure maximum deliverable capacity following the charging event.

Table 1.3 shows the results from the experiment in [58] for a more efficient charging method. After all the system was charged, both the reconfigurable and non-reconfigurable battery pack was discharged fully. The resulting discharge capacity of each battery pack was calculated to populate the table. The ϕ corresponds to the voltage imbalance within the battery pack, meaning the larger the ϕ, the larger the separation of voltages from cell to cell.

Table 1.3: Delivered Capacities (mAh) based on cell voltage imbalance and charging method [58]

ϕ	Cell	#1	#2	#3	#4
0.1	**Reconf.**	2619.5	2636.8	2617.6	2670.5
	Non-Reconf.	2508.5	2607.7	2613.7	2660.7
0.3	**Reconf.**	2607.6	2560.6	2608.6	2660.0
	Non-Reconf.	2597.3	627.8	2576.8	2459.0
0.5	**Reconf.**	2616.4	2628.5	2611.1	2665.2
	Non-Reconf.	2622.3	2510.3	2492.6	2304.3
0.7	**Reconf.**	2606.5	2614.8	2595.6	2646.3
	Non-Reconf.	2597.9	2046.1	857.7	2253.8
0.9	**Reconf.**	2617.9	2633.0	2610.9	2670.2
	Non-Reconf.	1566.4	2580.1	2340.3	2663.3
ϕ	**Cell**	**#5**	**#6**	**#7**	**#8**
0.1	**Reconf.**	2706.3	2582.0	2657.9	2621.9
	Non-Reconf.	2611.6	2575.6	2593.6	2606.5
0.3	**Reconf.**	2694.5	2567.7	2644.4	2609.6
	Non-Reconf.	2432.7	2458.2	2647.7	2276.7
0.5	**Reconf.**	2704.2	2577.6	2650.8	2611.8
	Non-Reconf.	2364.4	2222.4	2526.6	2610.6
0.7	**Reconf.**	2682.0	2555.1	2632.6	2593.6
	Non-Reconf.	1821.6	2553.6	2499.8	2300.0
0.9	**Reconf.**	2714.4	2579.4	2649.9	2606.7
	Non-Reconf.	2140.1	541.3	2501.5	2614.3

Intuitively, as ϕ gets larger, the more demand of an efficient charging process is needed, as can be concluded from examining the results within Table 1.3.

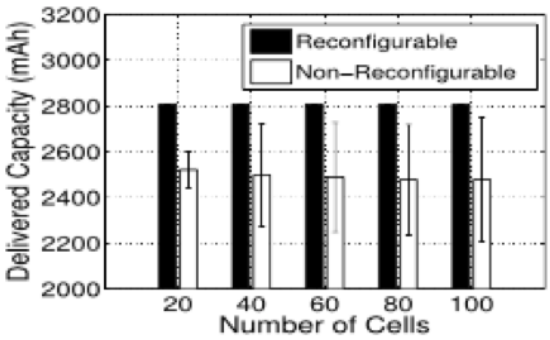

Figure 1.65: Capacity versus number of cells [58]

Figure 1.65 shows the additional experiment in [58] to characterize the need for a better charging method as the number of cells in a system increases. As can be seen, the performance of the reconfigurable battery pack remains constant as the number of cells increases.

This can be attributed to the process of category by category charging of the system. However, as the number of cells increases for the non-reconfigurable battery pack, the deliverable capacity begins to decrease and resulting in higher error ranges.

In terms of the EMS, cell imbalance will always be an issue within battery systems. How the EMS can efficiently use the cells within the pack will determine the limitations of which the pack can be used. If the EMS can utilize dynamic reconfiguration, even if solely for charging purposes only, the deliverable capacity of a fixed series-parallel discharging topology can increase compared to traditional EMS procedures.

1.6 Chapter Summary & Research Opportunities

This chapter outlined the state-of-the-art for Li-Ion battery management technologies. The various methods from sensor, algorithms and control strategies have been extensively investigated and discussed. While many aspects of an EMS have been identified and discussed, some have been identified as potential areas of interest for extended work.

Based on all the topics that have been introduced, there have been 3 main areas of interest that have been identified for further investigation. The first area of interest is the State of Energy Criterion which shows some intriguing capability, and raised several questions for use in EMS that current literature has not addressed.

- Direct comparison of how the SOE model relates to SOC while a Li-Ion Battery is being cycled
- Does the SOE model give a more computationally inexpensive result for range prediction in comparison to using SOC modeled with voltage to determine a range prediction
- How does the SOE vs SOC model differences change as a function of temperature or cell aging

The second area of interest is understanding the battery dimensional changes. In literature, the main areas of focus have been on thickness measurements of the cell via position

sensors on the face of the battery. However, commercially this isn't practical, since open space in the battery pack is extremely small. Due to this, applying a sensor device directly on the battery is critical, while ensuring that the sensor size is kept minimal. Several research paths have been identified in this topic that have not been discussed in literature, and are introduced here.

- Directly apply strain gauge onto the cell to have individual cell to SOC lookup based on dimensional change
- Directly compare the sensor measurements for a strain gauge as well as thickness measurement sensors to understand any differences, or benefits from using one sensor over another
- Investigate the potential of using the battery dimensional change after dynamic current events as an SOC lookup method to mitigate the need for rest time to perform an OCV-SOC lookup

The last area of interest has been identified as DR. In literature, this concept is relatively immature, and has only been investigated for small pack sizes, and only performed a few discharge cycles. Due to the relative immature technology, there have been numerous research interests that require further investigation, and have been listed here.

- How does DR performance compare to traditional static model as cells are aged
- Does performance improvements, or application flexibility change as the size of the battery pack increases. Does the performance improvement change linearly with pack size, or is there a unique relationship
- How does the number of switches per cell ratio effect performance improvements as the battery pack size increases. Is there a constant performance improvement, or another unique behavior that would need to be taken into account for designing the technology for a specific application

Chapter 2

State-of-Energy Model

2.1 Experimental Test Setup

Hardware Testing Setup

This section will describe the testing setup that will be used to perform the analysis discussed in subsequent sections. The testing equipment was donated from Johnson Controls, and placed in the Wisconsin Energy Institute (WEI). The testing equipment was purchased from Digatron, and has a large range of capabilities from testing small cell level equipment, to larger battery pack sized equipment. The specific testing capabilities include:

- 96 voltage and 48 temperature sensing channels
- 8 100V/100A circuits for battery module testing
- 18 variable charge/discharge circuits for cell testing
- 12 electrochemical impedance spectroscopy channels
- 3 thermal chambers, fully monitored
- 1 FILR thermal camera to assist in analysis

Figure 2.1 shows the Digatron testing station with the physical testing equipment behind the desk space shown. Additionally, Figure 2.2 shows the 3 testing chambers where the cells were placed to keep at constant temperature, but also protect the rest of the lab if any batteries

were to enter an unsafe operating condition and enter thermal runaway. Safety systems were designed and installed to work alongside the Digatron system, and monitored for both gas and smoke sensors. All circuits and chambers are connected in series to relays, so in the event that a gas or smoke sensor is tripped in one chamber, the entire Digatron system shuts down and isolates everything within the system.

Figure 2.1: Front view fo the test station used to control the Digatron system to perform battery tests

Figure 2.2: Battery test chambers that housed the physicals cells during battery tests to keep temperature controlled

Lithium-Ion Cells Used

The cells used for all experiments in this research project were provided by Johnson Controls, and one cell is shown in Figure 2.3. Note, that these cells are a prismatic can cell design. It is important to note, that for comparing SOE and SOC, the voltage profile is the key factor in model difference, and since the voltage profile is chemistry dependent, the exact model differences could vary between battery chemistries. This fluctuation in model differences could be significant, and can be studied in future work with various chemistry types experimentally studied in the same CCCV format.

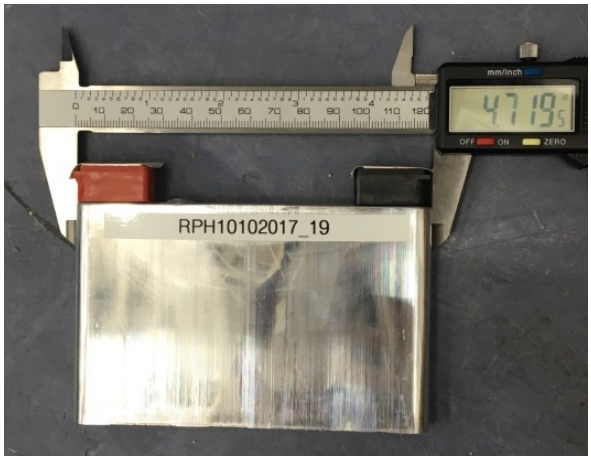

Figure 2.3: Li-Ion cell used for all experimental testing in research project

The voltage profile for the cells received from JCI can be seen in Figure 2.4 as reference. Note, that this profile is strictly chemistry dependent, which ultimately leads to conclusions from this chapter would need to be verified across numerous battery chemistries if commercially applied across applications.

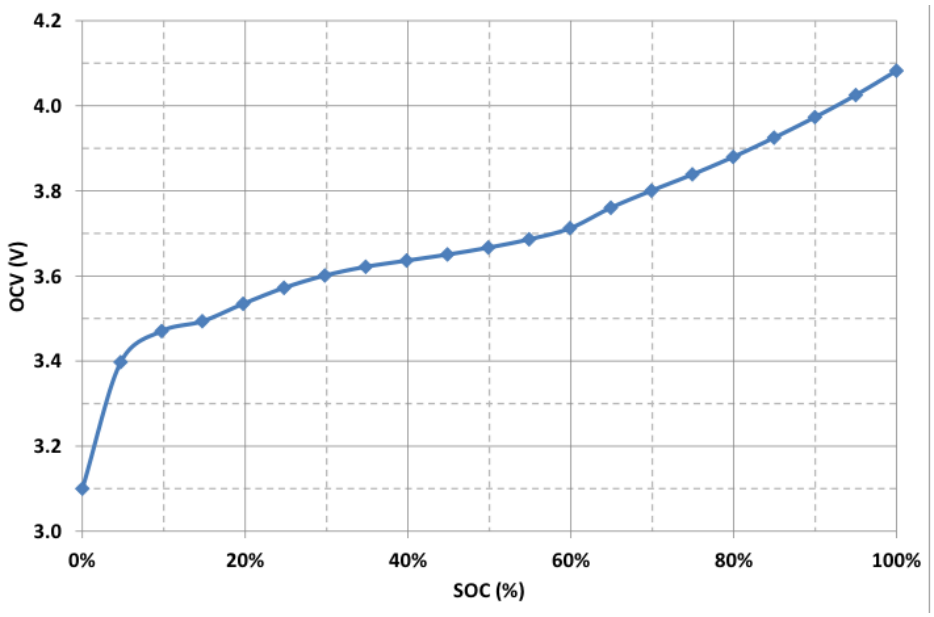

Figure 2.4: OCV curve of cell provided by Johnson Controls

Additionally, the cell specific characteristics can be found in Table 2.1. Both electrical and mechanical characteristics are included in the table. Note that the cell rated capacity is a good starting point, but in all cases, a capacity check will be done to determine the actual cell capacity for each cell used. This capacity value used will be significant, especially when being used to normalize the models in SOC and SOE discussed in this chapter.

Table 2.1: Electrical and Mechanical Characteristics of the Li-Ion cell provided by Johnson Controls

Nominal Voltage	3.65V
Typical Capacity (C rate, +20 Celsius)	5.6Ah
Minimum Capacity (C rate, +20 Celsius)	5.3Ah
Maximum Voltage (Continuous)	4.1V
Maximum Voltage (Pulse)	4.2V
Minimum Voltage (Continuous)	2.7V
Minimum Voltage (Pulse)	2.5V
Cell Height	85 mm
Cell Length	120 mm
Cell Thickness	12.5 mm
Cell Weight	240 g

2.2 Investigation of SOC vs SOE Model Differences

SOE is a immature concept that is still being investigated in literature previously discussed in Section 1.3.5. Since this is a relatively new concept, the investigation into potential advantages and disadvantages hasn't been extensively researched. Due to this, there hasn't been significant work into fundamentally understanding the difference in model results that SOE provides in comparison to SOC. As discussed in Section 1.3.1, the SOC algorithm is essentially a current integral that is normalized by the cells rated capacity. When expanding to the newly proposed model of SOE, the current integral is transformed into a power integral that is normalized by the cells rated energy. Understanding how the voltage profile effects the range prediction in a vehicle is critical for comparing between both SOC and SOE model results. If SOC is consistently under-predicting the remaining range of the batteries, then the application is prematurely shutting down. Understanding how the SOE model results compare to SOC is critical to ensuring accurate battery shutdown as well as extracting the maximum amount of energy from the battery system in a safe and efficient manner.

This investigation is rather straight forward to perform, where the post processing is the critical step to understand the model result differences. Performing a few CCCV cycles, while collecting the data for voltage, current, and time, the current (SOC) and power (SOE) integrals can be calculated to understand how each respective model performs under ideal conditions. Since we want to first understand the model differences, it is reasonable to do all

model comparisons as a post processing test style, where the exact capacity and energy of the cell (from the discharge event just completed) can be used to run the integrals. However, it is important to note that in an application scenario, this wouldn't be employed to operate both models, in which case creating specific real time models for each SOC and SOE would need to be done. However, since we want to first understand the best case scenario difference between models, the post processing method should be investigated first, with the option in the future to study real time predictive algorithms for SOE modeling to then compare to SOC models.

In order to investigate the difference between models, first defining the algorithms employed for each respective model needs to be introduced. Equation 2.1 introduces the algorithm that will be used to track the SOC for the CCCV testing. Note that the capacity value used to normalize the integral is the total Ah discharged from the cycle, which would include the Ah removed during the current tapering region (constant voltage region). Additionally, Equation 2.2 introduces the algorithm that will be used to track the SOE for the CCCV testing. Note that in this case, the equation is normalized by the exact energy removed from the cell during the discharge, including the current tapering region. In both equations, η_e is the efficiency associated with the current applied where in most cases the efficiency can be approximately to 1, but in extreme cases, the exact value needs to be tracked and included for model accuracy.

$$SOC\% = \frac{\int_{t_0}^{t_1} \eta_e I(t)dt}{C_n} * 100\% \tag{2.1}$$

$$SOE\% = \frac{\int_{t_0}^{t_1} \eta_e V(t)I(t)dt}{E_n} * 100\% \tag{2.2}$$

Utilizing Equations 2.1-2.2, the post processing for the CCCV experiments is all that is needed to directly compare the difference between both SOC and SOE models previously defined.

2.2.1 Discharge Event Comparison SOC & SOE

Experiments were performed to study the discharge capability, as well as model differences between SOC and SOE models when discharging cells from a fully charged state, to a fully discharged state. In order to do this, a CCCV method was executed at various C-Rates and ambient temperatures to get a vast understanding of the model behaviors. CCCV was executed by starting the cells at a fully charged state, and discharging the cell at a constant C-Rate until the lower voltage limit was reached. At this point, the constant current event was finished, and the constant voltage event begins until the current was below 100mA. For this experiment, 5 cells were operated under the same conditions, and 3 charge-discharge cycles were performed for all test conditions (ambient Temperatures, and C-Rates). Due to this, statistics were performed to obtain average values, with error bars added to the plots to show any deviation between the 5 cells, and additionally the difference in the 3 charge-discharge cycles.

Figure 2.5 shows the voltage and current experimental results from the CCCV experiment. Note that this figure shows the average value of the 5 cells, as well as the 3 charge-discharge cycles. The error bars are on the plot, but the error between the cells is so small, the error bars visually look like black dots along the lines. Note, that since the cell to cell variation is small for this cell, the conclusions to follow are dependent on the reproducibility across numerous cells. Additionally, the cells were tested under numerous C-Rates to understand any potential impact of SOC to SOE based on severity of C-Rate. Examining the results in the figure, its important to note the significance that the C-Rate has on battery performance in general. The CCCV protocol contains two main regions, one as constant current, and the second as constant voltage. From the figure, it is clear to see that the constant current region relative to the full time in the discharge event decreases when moving from lower C-Rates to higher C-Rates. This may seem relatively obvious, but this is important at this stage, since the lower voltage limit in most cases would signify approximately 0% SOC.

Understanding the results in Figure 2.5 is needed to extend the analysis to understanding

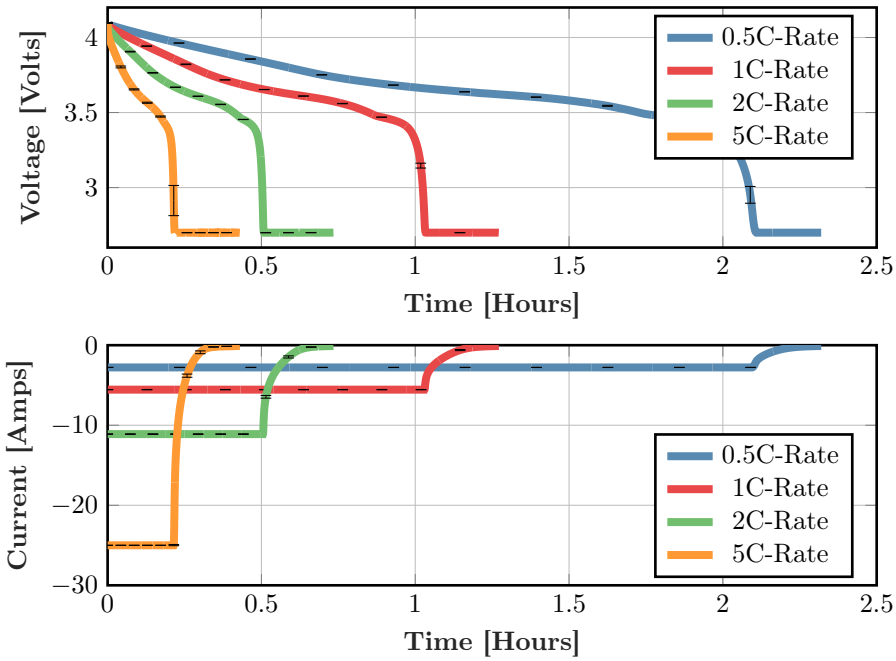

Figure 2.5: Experimental results at room temperature for single discharge event where top plot is showing Voltage, and bottom plot showing Current vs time relationship

the SOC and SOE models for the set of experiments. Since there are effectively two aspects to this CCCV test, understanding where the switch from the constant current to constant voltage region occurs for each respective C-Rate was needed to be understood in order to understand any change in slopes for the SOC or SOE model profiles. This figure also serves as a proof of experiment to show that the correct CCCV protocol was evaluated, so that subsequent figures can be examined adequately.

Figure 2.6 shows the SOC and SOE algorithms for the experiment across all of the C-Rates at room temperature. Examining these results and drawing comparisons between the models can be done, however it is challenging due to the similar profile and values of the respective models. Since the only difference between the models is SOE incorporates voltage into the integral, the variation in results can be minimal. However, the voltage of the cell can be greatly effected by the C-Rate of the cell, so it is intuitive to think the SOE model will be greatly effected by the C-Rate used.

In order to more adequately compare the models, a new calculation needs to occur. Understanding directly how the SOC and SOE models differ in real time are critical to understanding any potential benefits of the SOE model. Equation 2.3 shows the formula

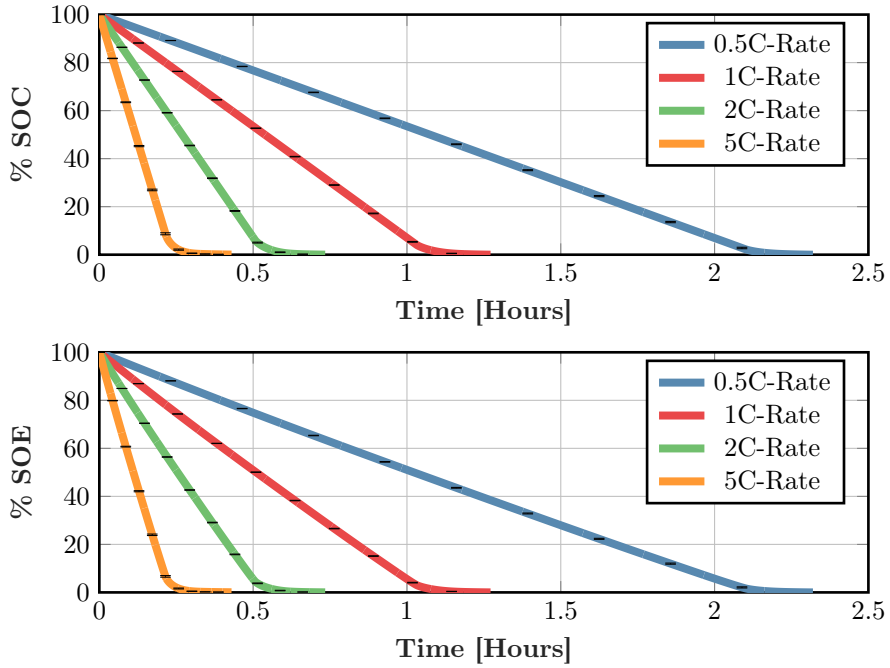

Figure 2.6: Experimental results at room temperature for single discharge event where top plot is showing SOC, and bottom plot showing SOE vs time relationship

for $\Delta SOCSOE$ in order to directly understand the model differences. Looking further to Figure 2.7, the models were directly compared by employing Equation 2.3 throughout the experimental data.

$$\Delta SOCSOE[t] = SOC[t] - SOE[t] \tag{2.3}$$

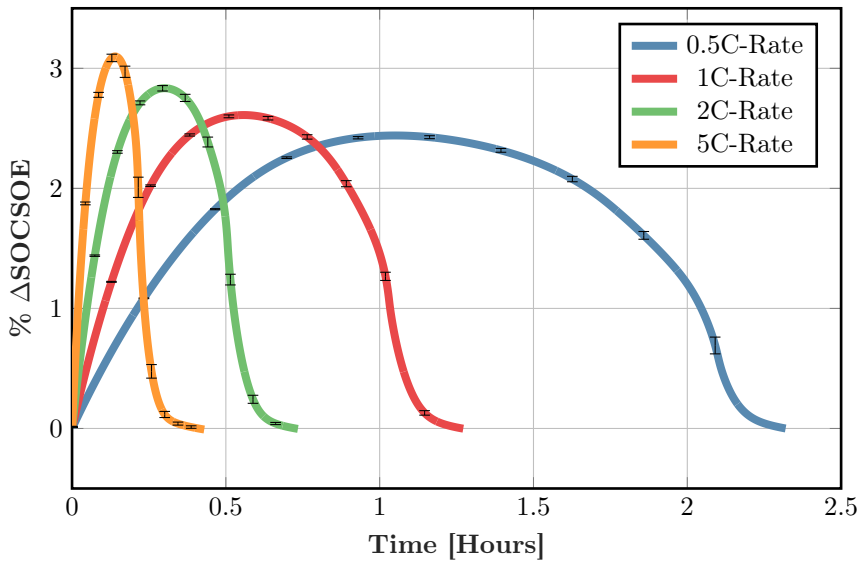

Figure 2.7: ΔSOCSOE vs time experimental results at room temperature (25 degrees Celsius)

Figure 2.7 is perhaps the most critical plot in this experiment to understanding how these models differ in a discharge event. Understanding this figure is critical, and perhaps most important is understanding the peak value of difference between SOC and SOE is dependent on C-Rate used. The 5C-Rate shows the largest variation between the SOC and SOE model, while the 0.5C-Rate shows the least variation. When an EMS would use both models, understanding the peak value of error relative to the C-Rate being used is critical in order to make the correct EMS decision.

Due to the interesting correlation between SOC and SOE for the C-Rate employed at room temperature, the desire to understand if this same relationship holds true at alternative ambient temperatures is desired. In order to gain an understanding of model performance at ambient temperatures other than room temperature, selecting temperatures to study on both the higher and lower end of room temperature is desired. For this study, 10 degrees and 45 degrees Celsius were selected to be studied.

Once again, the CCCV protocol was performed at both 10 and 45 degrees Celsius. This data was then post processed the same way as the room temperature data previously discussed, and subsequently, drawing analysis across these three temperatures is ideal to understanding the models performance across a wide temperature range. With these 3-dimensional plots, it is important to note that only the three temperatures were tested, and on the figures they are denoted by the thicker colored line plots. However, for visual analysis, the surfaces were drawn between these temperatures so that conclusions can be drawn for model behavior across all temperatures between the experimentally tested.

Figure 2.8 shows the voltage and current profiles for all three temperatures to ensure the desired test protocol was achieved. Once again, the test profile exhibits a two part profile, where the first is the constant current region, followed by a constant current region. The profile throughout both of these regions stays relatively similar across the range of temperatures tested, so further analysis needs to be performed in order to visually, and analytically see performance differences. In order to achieve this, the post processing analysis of SOC and SOE models were calculated in order to understand the temperature effect on the SOC and SOE models.

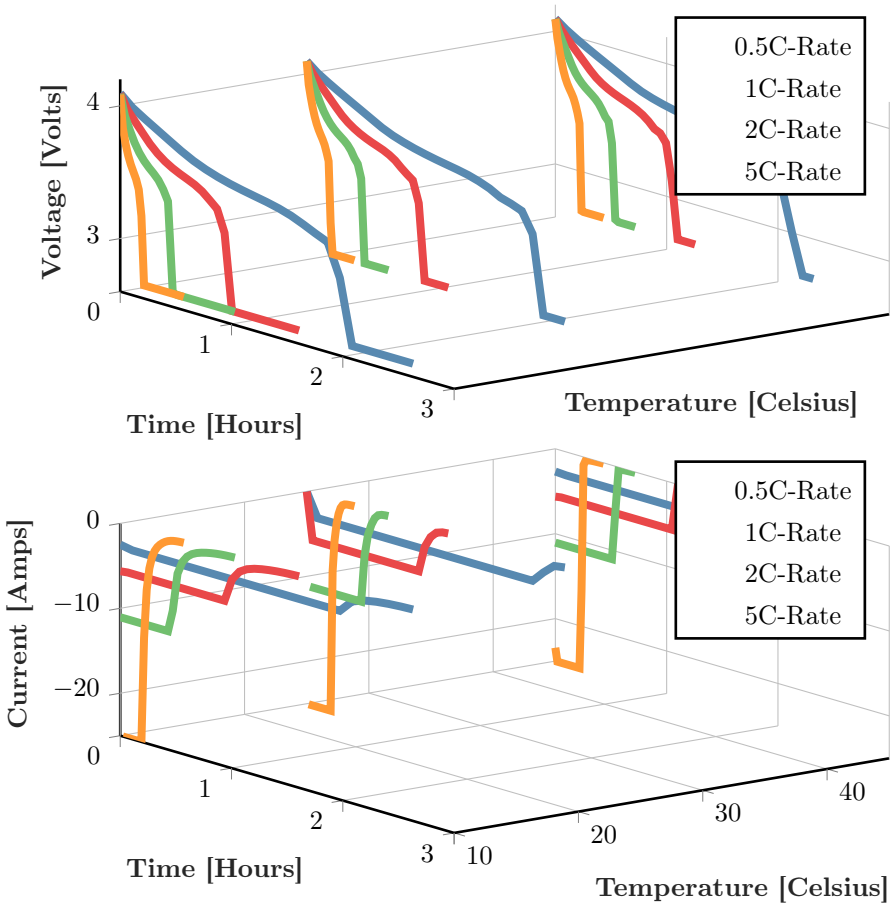

Figure 2.8: Experimental results at multiple temperatures for single discharge event where top plot is showing Voltage, and bottom plot showing Current vs time relationship

Moving further to understand how both the SOC and SOE models behave across these three different ambient temperatures, Figure 2.9 shows the calculated models in 3-dimensional plots comparing the discharge event across the various ambient temperatures tested. Once again, due to the similar nature between the models, conclusions were difficult to draw from examining these surface plots. While there can be some conclusions relative to each individual C-Rate profile being effected by the temperature changes, drawing comparisons from each subplot for both SOC and SOE models are still not plausible. This can be deduced by the only difference between the models being the SOE incorporating voltage into the integral, and the voltage profile found in Figure 2.8 shows very minimal changes in value, especially in the middle ranges of the discharge event.

Utilizing Equation 2.3 again will allow better visualization of the model differences,

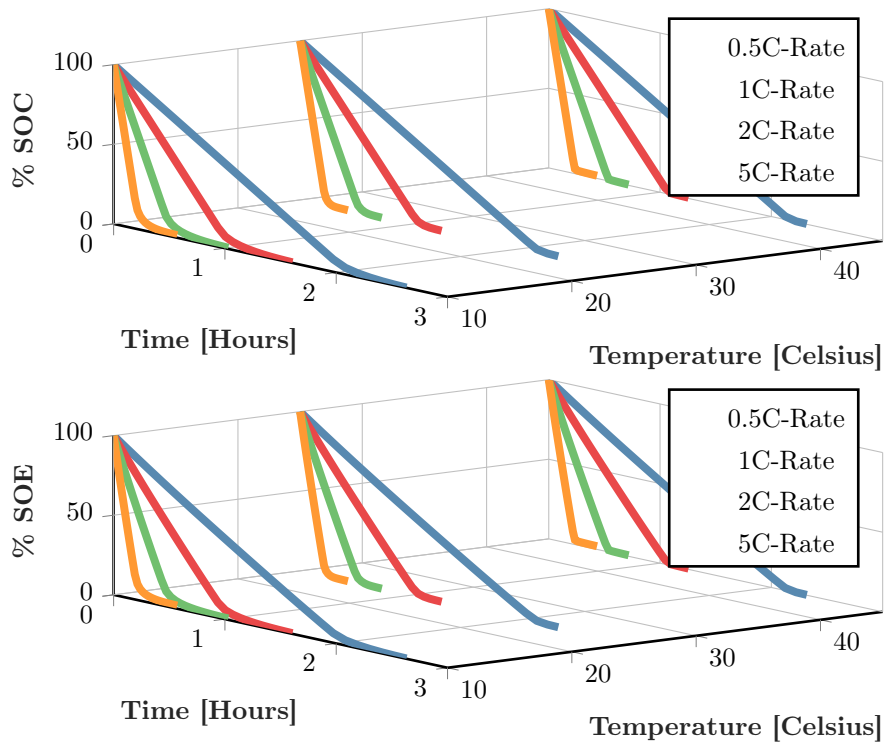

Figure 2.9: Experimental results at multiple temperatures for single discharge event where top plot is showing SOC, and bottom plot showing SOE vs time relationship

and allow justifiable conclusions to be drawn. Figure 2.10 shows the $\Delta SOCSOE$ calculation to help visualize the model differences during a discharge event across a spectrum of temperatures. Note, that the peak value is still C-Rate dependent, but as the temperature is changing, the trend for peak error changes as well. However, the change of the peak value for each respective C-Rate does trend from the highest difference (at lower temperatures) to a smaller model difference (at higher temperatures). This variation in performance can be attributed to the effect that the battery voltage has with respect to temperature. The overall battery voltage is largely effected by changes in temperature, and the SOE model incorporating the voltage into the integral while the SOC model does not would result in the model differences being effected by temperature as well.

If utilizing the SOE model alongside an SOC model in an EMS, any control decisions that are made based on model differences alone needs to fully understood the situation that the system has been exposed to, both in C-Rate but also based on ambient temperature. The experiments focused on understanding the C-Rate dependence for the model differences

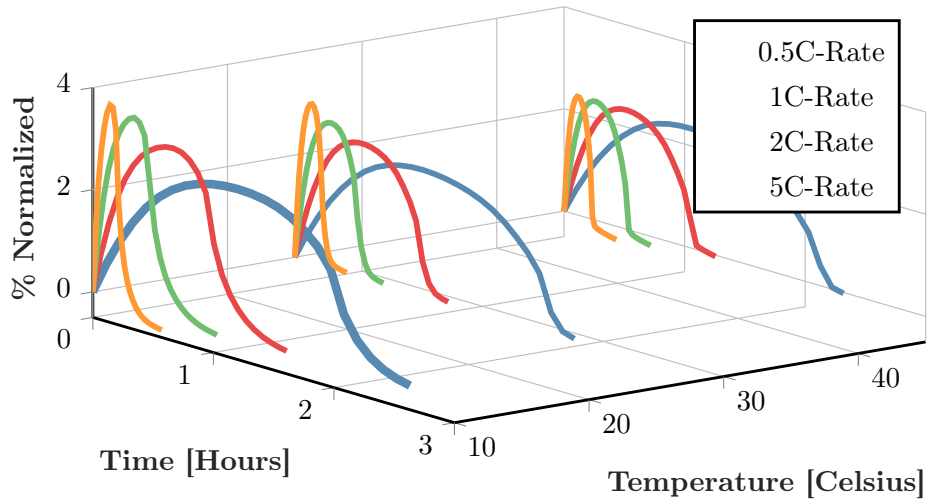

Figure 2.10: ΔSOCSOE vs time experimental results across multiple temperatures

first, then extended to multiple temperatures to understand the dependence beyond just C-Rate. If this correlation seems plausible in a real world application, the next step is to fully understand how these model differences behave as the battery is aging.

2.2.2 Aging Effect on SOC-SOE Model Variations

Previous investigations focused on single discharge event behavior, but understanding how these models behave as a battery is aged is needed for any future consideration in commercial applications. In order to do this, 3 batteries for each C-Rate were aged with the same CCCV protocol used for the single discharge event, however these results were continued on until the batteries reach failure. Failure criteria for this experiment is defined as when a battery reached 80% SOH. This is measured by comparing the discharge capacity in the individual cycle, relative to the discharge capacity achieved in the first cycle of the experiment. Two C-Rates were used in this experiment, 5 and 2 C-Rate. From a time perspective, these rates wouldn't take more than 8-9 months to age the batteries at room temperature, while still providing crucial information about the model differences in a C-Rate range that is widely used in commercial applications.

Since an aging study is being performed for the batteries, tracking the capacity relative to the C-Rate being applied is needed to understand the profile of how the battery capacity fades. Additionally, tracking the battery capacity for each respective C-Rate will serve as the

validation criteria to ensure that the battery has reached failure criteria (e.g., 80% capacity remaining). Figure 2.11 shows the capacity curves for both 2, and 5 C-Rates as the batteries were aged. The figure also contains a line indicating the 80% value of capacity that needs to be reached in order to classify the batteries as "failed". Note that both C-Rates (5 and 2) reached the failure criteria denoted by the black line in the figure. Since they both failed, further figures can be examined to study the aging effect between the SOC and SOE models.

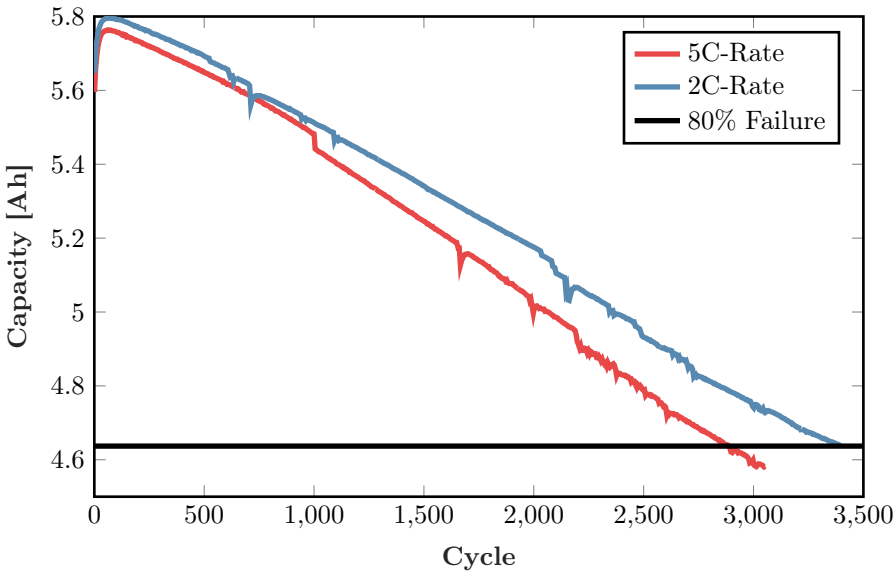

Figure 2.11: Capacity tracking to monitor when each respective C-Rate being tested reaches the 80% failure criteria

After understanding the capacity curves for each respective C-Rate, examination of the voltage profiles for these C-Rates as the batteries were aged is an essential first step. Figure 2.12 shows the 3-D plot for the voltage profile data as a function of cycle number, and the individual discharge event. As expected, the voltage profiles seem relatively unaffected as the battery was aged to the naked eye. However, there were slight changes to the profile over the batteries lifetime. In order to visualize this voltage change effect, moving further to examining the SOE model will reflect any voltage effect incorporated. However, showing just the SOE model might be redundant, as shown in previous sections, but moving straight to the important criteria for this study seems adequate. Prior sections showed that the figures showing solely the SOC, or SOE model were difficult to understand any differences, resulting in skipping these figures in order to directly understand the model differences as a function of aging.

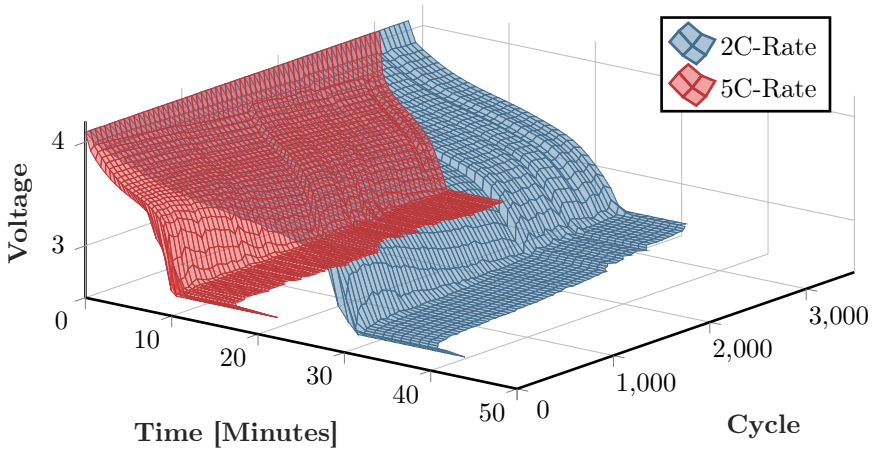

Figure 2.12: Voltage profile for each respective discharge as a function of the cycle, to show how the voltage profile evolves alongside aging of the battery

Since the capacity, and voltage curves have been studied, moving forward to the relationship denoted by ΔSOCSOE is necessary to understand any model differences as the batteries were aged. Recall, that all of the cells failed, so understanding close to the end of life behavior is important to understand how these models behave prior to any failure events. Figure 2.13 shows this ΔSOCSOE data, and remembering the profile behavior in the prior sections is needed to understanding the aging effect. Initially, note that the relative profile remains rather uniform as the battery is aged, with the exception that the actual values for peak difference might change, the overall shape of the curve seems to remain intact.

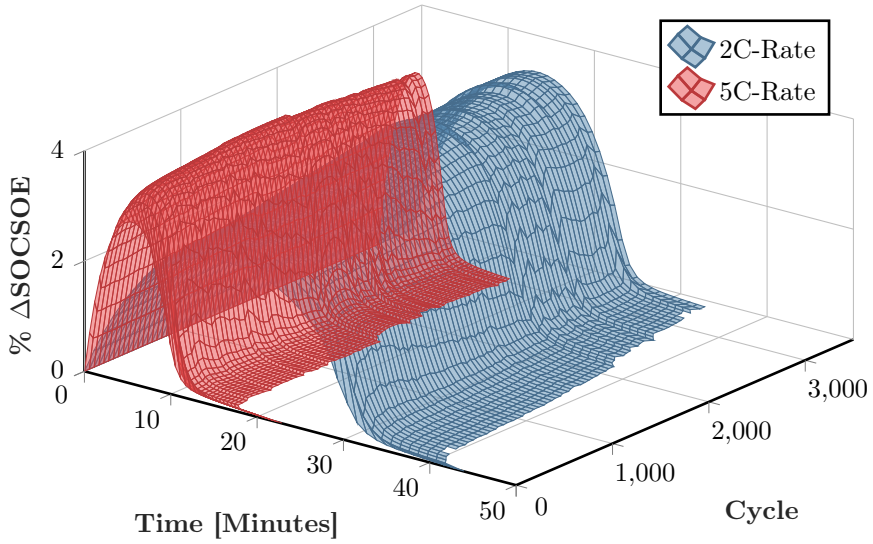

Figure 2.13: ΔSOCSOE vs cycle showing the discharge curve to understand how the model differences behaves as the battery is aged to failure

A few key aspects can be derived from examining the figure for SOC-SOE model differences. First and foremost, the profile of the model differences remains relatively constant in each cycle as the battery was aged. This is important, because this allows the potential for a predictable profile as a function of battery aging. Secondly, the end of life behavior seems unaffected by the model differences. This is important to understand, since predicting performance when the batteries become severely aged, or degraded, becomes more critical. Lastly, the peak value for model differences as a function of cycle increases as the battery ages. Essentially, this means that the batteries voltage profile is changing as the battery ages. Since the model difference increases as the battery ages, this says that the voltage being incorporated into the integral for the SOE model has significant impact on the resultant model output.

Since the aging shows to effect the model differences, some potential paths forward can be constructed to further understand the resulting models. Since the voltage being incorporated into the integral for the SOE model, does the voltage evolution as a function of aging show some type of over-degradation that the SOC model does not detect? In an application scenario, specifically for applications that have DOD less than 100%, the model differences are on the order of approximately 2-4%. Therefor, if a application shuts the battery pack down when the lower SOC limit is reached, the resulting SOE model would have hit its limit sooner than the SOC model. Thus, would shutting the pack down sooner (when the SOE model reaches the lower limit, but the SOC is still above the limit), result in minimizing the battery degradation and/or prolonging the life of the system? If shutting down the pack based on the SOE model prolongs life by reducing the degradation factor, a trade off would need to be well understood to make sure the sacrifice in discharge energy during the cycle is compensated by more throughput prior to the battery failing.

2.3 Chapter Summary

This chapter introduced and analyzed the model differences between SOC and SOE under numerous different test conditions. First, the models were compared for a single

discharge event at room temperature for numerous C-Rates. The model difference between SOC and SOE was found to be C-Rate dependent, as the peak value of model differences was found to increase as the C-Rate increased. Secondly, the model differences was studied as a function of the ambient temperature of the system. The model differences showed similar profile characteristics as how voltage is affected by temperature. Since the model differences plot showed that the difference becomes smaller at elevated temperature, this shows that the model difference is largely effected by the voltage variation, which was largely effected from the ambient temperature change.

Lastly, an aging experiment was performed to understand how the model differences between SOC and SOE behaves alongside battery degradation. The profile showed that model differences remain relatively consistent, however, the peak value of model differences seemingly increases as the battery is degraded closer to failure. Due to this profile evolution, future consideration for the impact of these model differences was proposed. Since the SOE model incorporates voltage into the integral, it seems as though the SOE model considers the voltage aging throughout battery degradation that the SOC model does not track. Due to this, consideration as to whether shutting down the battery system based on SOE instead of SOC might result in lowering the degradation rate of the battery, since the SOE model gives degradation indicators through the voltage signal that the SOC model does not have the capability to do.

Chapter 3

Battery Dimensional Changes for Instantaneous SOC Lookup

3.1 Measuring Battery Dimensional Changes for SOC Lookup

Measuring battery dimensional changes was introduced and discussed in Section 1.4.1, but sparked an interest for potential application to help improve battery systems capability. Previous work on measuring battery dimensional changes was to understand if and how the batteries dimensional changes corresponds to the operating voltage of the battery. However, applying this concept to how the EMS controls and protects the battery, their is unanswered questions that need to be understood if this dimensional changes corresponds to SOC as well. Tradition EMS methodology uses SOC tracking during real time operation, and at times of rest, the EMS performs an OCV-SOC lookup to perform an "SOC Adjustment". However, this OCV-SOC lookup method can only be performed after the system has been at rest. For a DES application, traditional time to wait is 5 minutes, but the more rest time demanded, the higher the SOC accuracy there will be.

From an EMS perspective, if this demanded rest time for SOC adjustments can be mitigated, the overall battery pack throughput across a year, or even the pack lifetime will drastically increase. The goal of this study is two-fold. The first is to understand if measuring dimensional changes can be done locally on a battery in a volume conscious manner (e.g., strain gauges). The second is to understand how the battery dimensional changes are

effected after the system is put to rest. If the battery dimensional changes polarizes similar to the cell voltage, then the need for this sensor wouldn't exist. However, if the battery dimension stays stagnant after the current is changed to zero, then the battery dimensional changes to SOC method could be used as an instantaneous SOC lookup method to mitigate rest time in operation.

3.1.1 Measuring Battery Dimensional Changes

A few measuring techniques were described in Section 1.4.1, and deciding which ones to investigate for use in this battery dimensional change to SOC lookup method is critical to the success of this research. Both thickness measurement and implementing strain gauges show promise for techniques to investigate. Thickness measurement, because it directly measures the dimensional change of the battery, but it is not a practical method. A real application will not have the volume to have this type of apparatus set up around each battery in the system. Strain gauges however, offer a volume effective method to monitor each individual battery in a system. Ideally, a correlation to the strain of the battery to the battery dimensional change, and ultimately to the SOC of the battery can be made. In previous work, the strain gauges were not implemented locally to the battery, they were mounted to a tie rod that is used to hold plates together across a string of batteries (typically 5-6 cells together). So for this work, implementing strain gauges locally to a single battery while having the measurement accuracy to correlate to SOC is critical to the success of this research.

Methods for Monitoring Dimensional Change

Several methods for monitoring battery dimensional changes were discussed in detail in Section 1.4.1, and should reference back for the needed information. However, the purpose of this chapter is to understand the extended work needed, and potential areas within this focus area where an advancement in battery system performance can occur. Understanding that the strain gauge method offers the volume sufficient sensor capability to actually apply this technology in a commercial setting, strain gauge monitoring will be the target method to

monitor battery dimensional changes. However, additionally monitoring the battery thickness via position sensors is desired as a additional validation method to guarantee accurate readings from the strain gauge correlation.

Experimental Test Stand Hardware Setup

The hardware setup for this experiment is comprehensive in order to achieve the multiple measurement systems needed for this technology. First, Digatron systems were used to record the battery related data such as: Voltage, cell temperature, current, etc on the battery side. Details for this system can be found in Section 2.1. For the position sensor, a Versatile Data Acquisition System (VDAS) is used to record the position reading of the Mitutoyo position gauge. Additionally, the VDAS system records the battery voltage, as a means to synchronize the data collected between the Digatron and VDAS systems. The strain gauges were positioned on the cell, and utilizing a wheatstone bridge electrical circuit, the voltage output from the wheatstone bridge will be connected to a voltage sensor that the Digatron system reads. Note that these voltages were collected alongside the battery related events, so no data synchronization is needed here.

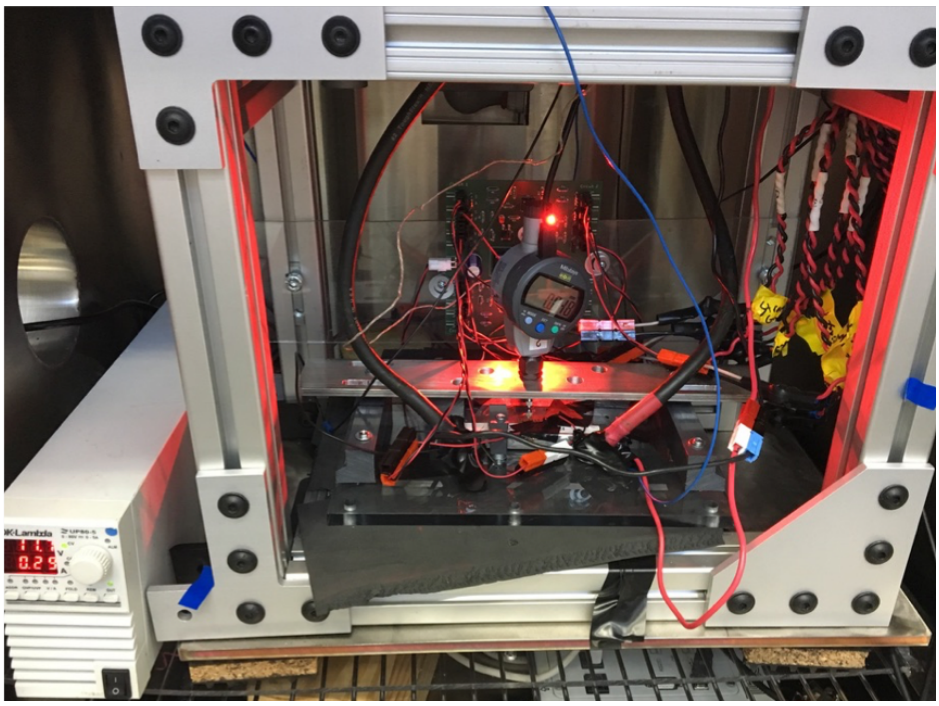

Figure 3.1: Experimental test stand used for monitoring strain and thickness measurement of batteries alongside battery testing

Figure 3.1 shows the full test stand setup inside the battery testing chamber. The wheatstone bridge is found on the custom made PCB board (with red LED light) mounted behind the cell. The DC power source to the left is used as the excitation voltage measurement for the wheatstone bridge. The VDAS system is positioned in the chamber directly below the battery. Two levels of vibration pads were installed into the stand to reduce any potential signal noise that the strain gauges would be recording due to the test conditions of the lab where the stand is located.

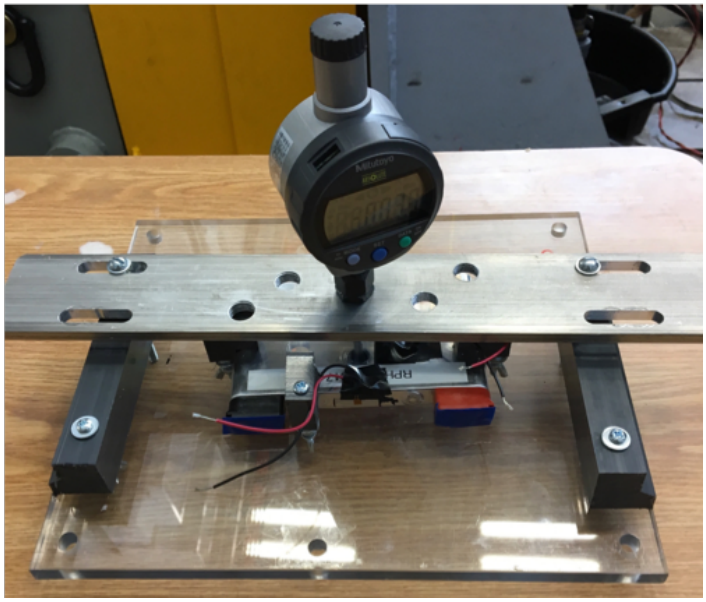

Figure 3.2: Cell holder view showing strain gauge connections, along with the thickness gauge

Figure 3.2 shows the holder that the battery is placed in prior to inserting the battery into the test stand and connected to the Digatron and VDAS systems. Note that the battery is in a fixed location, and cannot move in any direction. The battery is on a flat surface on the bottom, with minimal contact on the top surface of the battery (to reduce any possible effect on the battery dimensional change due to the fixed constraints), and the Mitutoyo position sensor is fixed to the metal plate with the position probe placed directly in the center of the battery surface.

Figure 3.3 shows a side view of the battery holder in order to see the point of contact for the position sensor to the battery. Additionally, two of the three strain gauges can be seen in this view. Placement of the strain gauges will be discussed further in the following section.

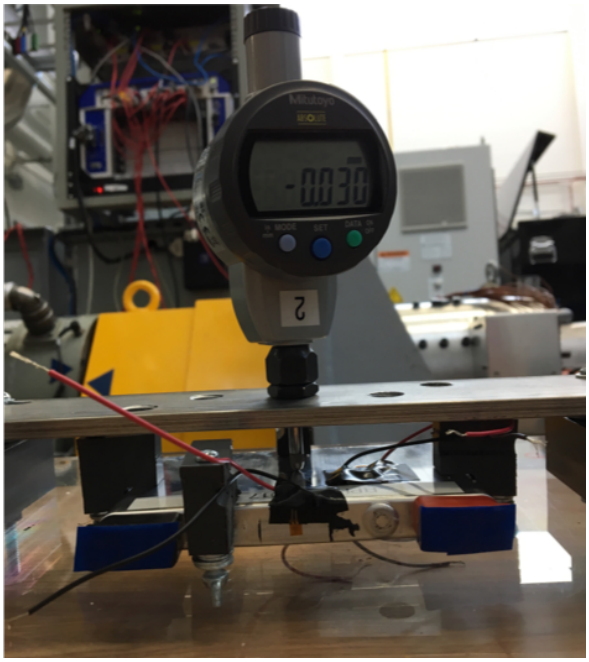

Figure 3.3: Side view of battery holder to see thickness gauge contact point on battery

3.1.2 Strain & Thickness Gauge Implementation on Batteries

The placement of the dimensional changes devices were critical to interpreting the quantitative value of change during battery cycling. On a prismatic cell, the value of dimensional change will differ for each surface on the battery. Figure 3.4 shows the top face view of the cell, and this is the surface that the most dimensional change will occur. Since we will see the most dimensional change here, a strain gauge is desired to be on this surface. Additionally, a position sensor needs to be set to this surface so that a correlation between battery thickness and surface strain can be made.

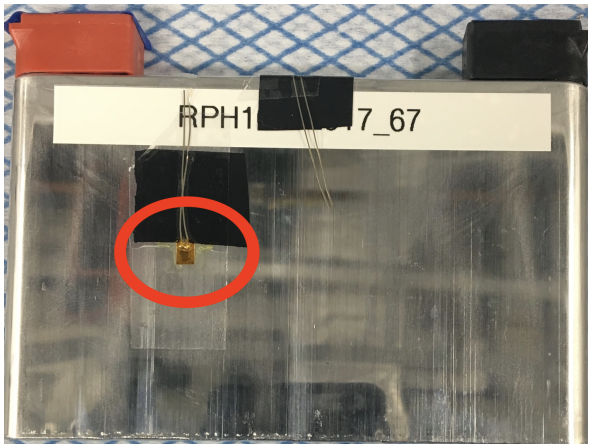

Figure 3.4: Front side view of the cell showing position of the strain sensor, where the red circle shows the location of the sensor

Figure 3.5 shows a enhanced close up view of the strain gauge location on the battery. Note the position of the strain gauge itself relative to the battery. The strain gauge is placed slightly off center, since the Mitutoyo position sensor will be placed directly in the center. By placing the strain gauge slightly next to the position sensor location, the two measurements should be reasonably comparable when correlating to SOC.

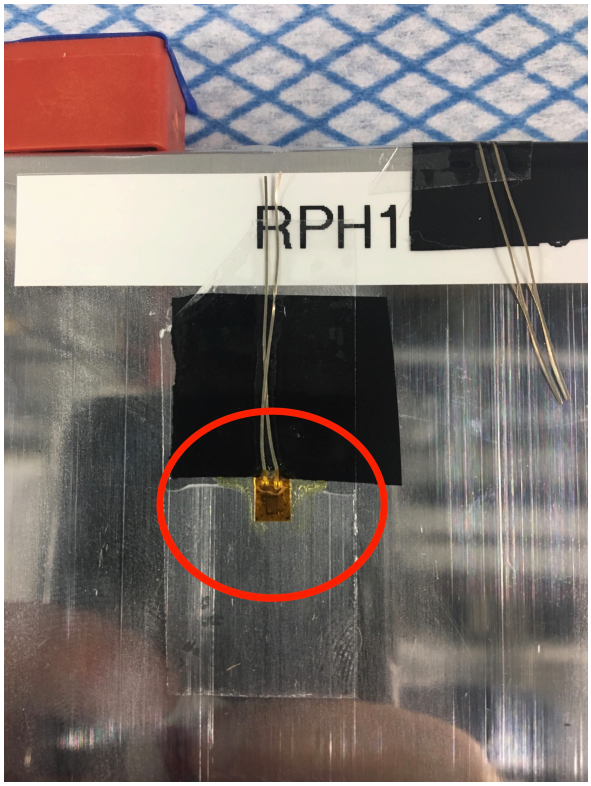

Figure 3.5: Close-up view of the strain gauge mounted on the front surface of the cell, where the red circle shows the location of the sensor

Figure 3.6 shows the location of the additional strain gauge on the back side of the battery. Note that in this case, the strain gauge is offset from center, so that its location is identical to the strain gauge on the front surface. The goal of this sensor is to have virtually identical strain measurement readings compared to the front sensor, in order to validate that both sensors were reading accurately to the battery behavior.

Figure 3.7 shows the final strain sensor placed on the battery. Note that this sensor is not on the location of the battery where the most dimensional change will occur, however it is in a strategically placed location for analysis. The cell design placed a vent location here, which is essentially a thinner thickness location of the metal in order to intentionally

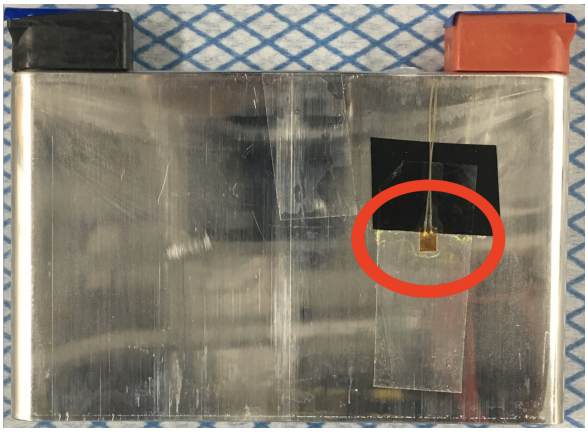

Figure 3.6: Backside view of the cell showing the location of the third strain sensor on the cell, where the red circle shows the location of the sensor

burst when pressure internal to the cell gets to a critical level. Due to this thinner material location, the surface will theoretically show more rapid deflection. Placing a strain sensor here, we hope to see a much more sensitive and rapid signal. If successful, this work could lead to an engineering design process for the cell casing, where a ideal location for the vent and strain sensor will be designed into the cell prior to production to make the best region for strain measurement.

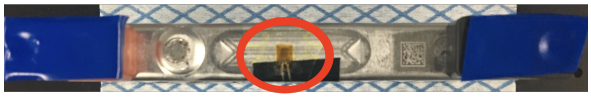

Figure 3.7: Top view of the strain gauge mounted on the vent location of the cell, where the red circle shows the location of the sensor

3.2 Battery Cycling Analysis with Implemented Dimensional Change Sensors

The first goal of this research is to understand the viability of applying strain gauges directly to an individual battery for battery dimensional change measurements in real-time. Prior research discussed in the Literature Review showed strain gauge implementation for dimensional change measurement by applying the strain gauge to tie rods that were used to hold a string of batteries together. The prior work typically had 5-6 batteries in series, stacked side by side with the tie rod strain change reflecting the lumped dimensional changes

of all 5-6 batteries. In order to implement this technology with the purpose of SOC adjustments instead of OCV-SOC correlation, the strain correlation must be battery specific. Ultimately, this means that the strain measurement cannot be a lumped change measurement across a string of batteries, but must be mounted to each battery individually.

Prior sections in this chapter showed the strain gauge, and thickness gauge sensor locations for the experiments, and the first set of experiments purpose were to validate strain gauge measurement potential local to the battery. The test ran via Digatron software is a simple CCCV cycling protocol, with strain, thickness, and battery parameters (Voltage, Current, etc.) being recorded and synchronized accordingly. First, examining an individual cycles performance is adequate to understand the strain gauge readings, and then further examination to cycle life would be necessary to understand commercial viability. Figure 3.8 shows a single cycle curve where the battery is initially at 100% SOC and discharged via CCCV to 0% SOC, rest for 10 minutes, and then charged via CCCV back to 100% SOC. Both voltage, and the thickness sensor measurements are shown in the figure, where the voltage curve corresponds to the primary y-axis, and the thickness sensor corresponds to the secondary y-axis. Note that the secondary y-axis units is normalized, which is done to be able to overlay the thickness measurements with the strain sensors in future plots in order to directly compare the sensors curves relationship to voltage directly against each other.

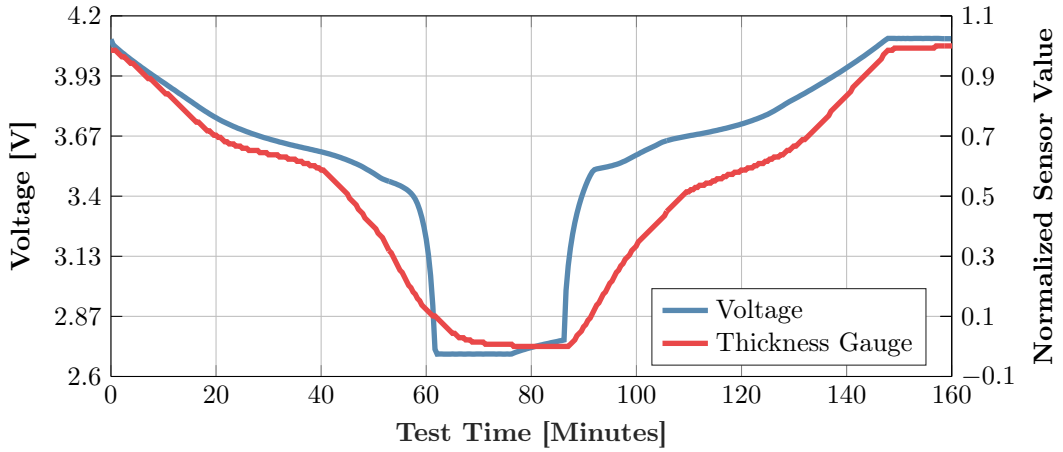

Figure 3.8: Single cycle comparison showing voltage profile alongside the normalized values for the thickness gauge

Figure 3.8 was performed with a 1C-Rate, which is slow enough to reasonably assume the physics behind the battery expansion/contraction has adequate time to take place, which

is reflected in the thickness sensor curve relationship. From this figure, it is reasonable to conclude that this battery specific chemistry is viable to monitor battery dimensional changes and compare them to a voltage, which ultimately could mitigate the OCV-SOC need and instead draw a thickness-SOC comparison. Now that the thickness sensor measurement seems to be adequately measuring the specific battery dimensional change, looking forward to analyzing the three strain gauges implemented on the battery is needed.

Figure 3.9 shows the normalized strain curve for strain gauge 1 (note strain gauge 1 was introduced in the prior section to identify a specific location) during the same CCCV cycle shown for the thickness gauge. First off, the curve for this strain gauge shows significantly more noise than the thickness gauge, which can be contributed to a multitude of factors. The first factor, is that the strain system was a simple wheat-stone bridge made in the lab as a quick test to study the viability, and the noise could be significantly reduced by implementing a robust, industry designed strain gauge measurement system (e.g., adding temperature compensation strain gauges, reduction of wire noise, etc.). However, the scope of this project was vast enough, that financial resources could not be dedicated to purchase a highly accurate system in order to study this at the current stage of this research. Although, the purpose of this study is to understand if this technology can be used, and the perfect measurement is not necessary since this is not moving directly into a commercial application. Future work in this area could dedicate a financial investment to make a more robust measurement system in order to study exact values for an application use.

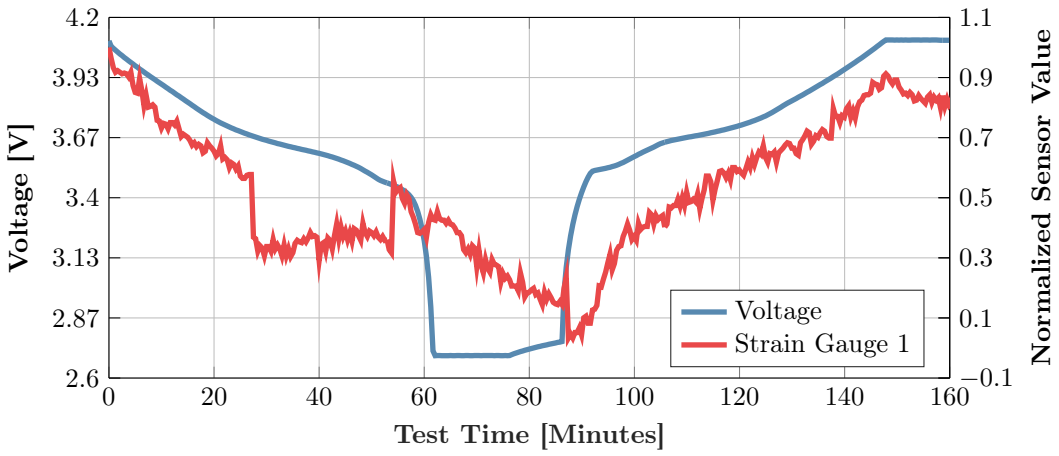

Figure 3.9: Single cycle comparison showing voltage profile alongside the normalized values for the strain gauge 1

Strain gauge 1 certainly showed more noise than the thickness measurement, which is fine, as long as the profile of the curves show the same results overall. At 25-55 minutes, the measurement seems to drop, and then bounce back, which was concluded to be resulting from external noise in the lab. The main source of this noise was a dynamometer that is within close proximity to the equipment that was testing high speed electric machines, and unveiled an important aspect of this strain gauge technology application: vibration. Seeing this result, an in-depth understanding of any surrounding vibration is crucial in order to maintain the integrity of the strain-SOC correlation.

Since strain gauge 1 showed an increase in sensor noise compared to the thickness measurement, further analysis in to the remaining two strain sensors is needed to understand if this is a universal issue, or specific to the location the strain gauge is implemented onto the battery. Figure 3.10 shows the voltage and strain gauge 2 measurements for the same CCCV cycle discussed previously. First off, the strain sensor drop from 25-55 minutes is not seen here, which shows firsthand that the sensor placement decision is critical to the values of strain used to correlate to SOC. However, this sensor still shows significant noise in comparison to the thickness sensor, which is okay in terms of this research investigation, but further sensor optimization is necessary to become commercially viable.

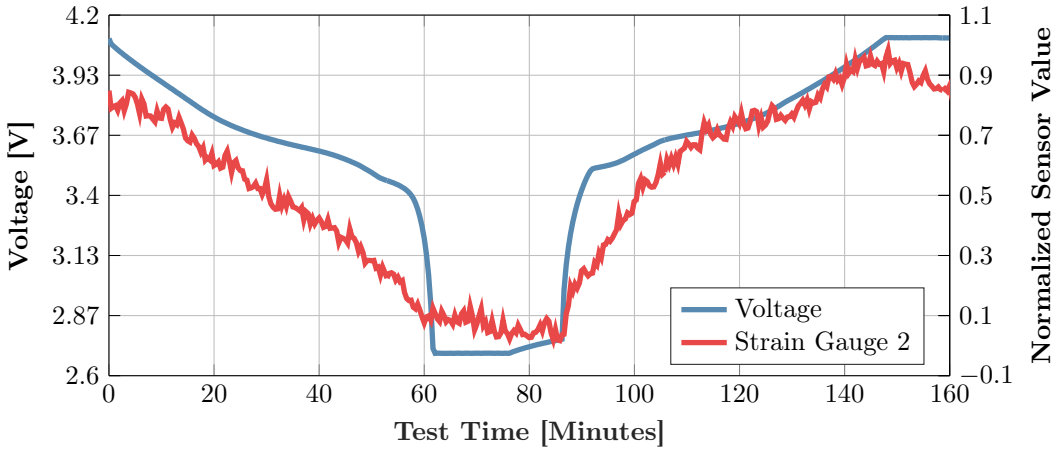

Figure 3.10: Single cycle comparison showing voltage profile alongside the normalized values for the strain gauge 2

Since previous results show that the strain sensors 1 and 2 show an increase in noise, extending the analysis to the third strain gauge is necessary to understand the battery performance. Recall, that this strain sensor is placed over the cell vent region, where a smaller

metal can thickness is found (the smaller thickness is designed so that the vent will systematically fail when the cell internal pressure reaches a critical level). Figure 3.11 shows the voltage and strain measurements for the same CCCV cycle discussed previously. Most importantly, notice that the sensor noise now looks significantly reduced, which can be attributed to the thinner metal can thickness allowing more deflection to be shown. Additionally, it is important to note that for the wheatstone bridge circuit used to record the strain readings, the operational amplifier circuit for strain gauge 3 is 10 times smaller than the amplification needed for strain gauges 1 and 2. This is important, because this says that the vent location shows more than 10 times the overall deflection, additionally resulting in less signal noise due to robust measurements.

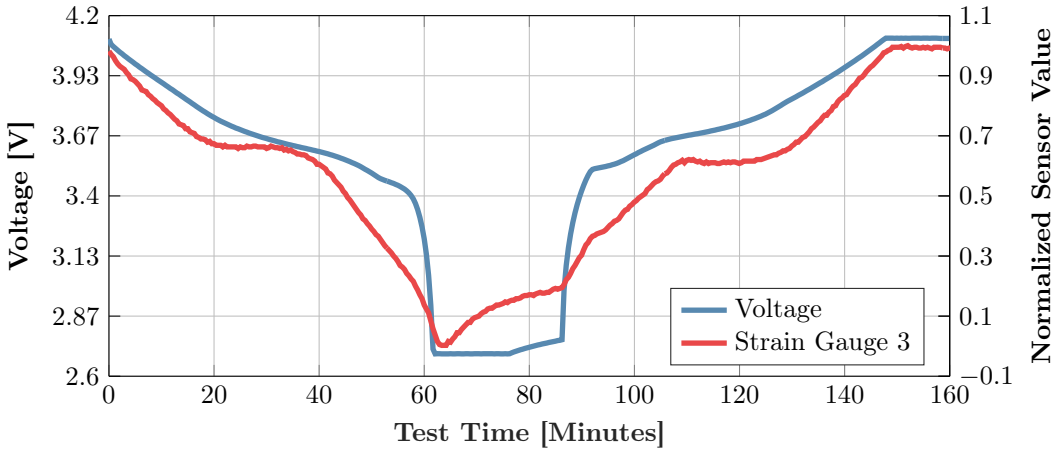

Figure 3.11: Single cycle comparison showing voltage profile alongside the normalized values for the strain gauge 3

Since strain gauge 3 showed a robust signal measurement, further analysis into the SOC correlation can be done, however, a discussion first about this specific strain gauge is necessary. The results of this simple experiment show a future mechanical engineering design application to study a special region built into the battery casing for strain gauge placement. Since the strain gauge was placed on the vent, the surface is not already optimized to place a strain gauge, so in order to optimize this technology, it is reasonable to state that designing a special flat, smooth surface into the battery casing would be best in order to guarantee more robust and most importantly, a reproducible measurement.

Further analsis beyond a single cycle correlation is needed for advancement of this technology's potential. To do this, 40 cycles utilizing the CCCV cycling protocol is performed

on the battery while monitoring both strain and thickness measurements. Since previous results show strain gauge 3 as the clean, noise reduced signal, the comparison between strain gauge 3 and the thickness sensor will be performed in this step. Henceforth, strain gauge 3 is denoted in the following figures simply as the "Strain Gauge" data, since plots overlay both the strain and thickness measurements. Figure 3.12 shows the 40 cycle CCCV test, with Voltage corresponding to the primary y-axis, and both Thickness and Strain Gauge (strain gauge 3) normalized measurements corresponding to the secondary y-axis. Note that throughout the cycling, both strain and thickness curves seem to adequately trace the same profile as the voltage measurement. However, it is important to note that for cycles 9 and 10 (corresponding to times 23-25 hours) show a signal increase for the strain measurement. This is contributed to noise in the lab, which was investigated to validate, in order to ensure this wasn't a significant sensor relationship attribute to the battery expansion/contraction.

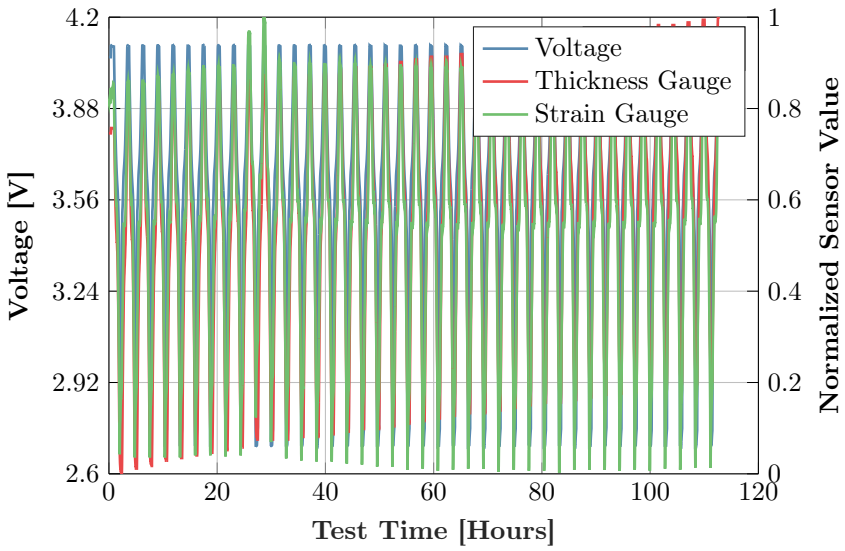

Figure 3.12: Multiple cycles look at voltage, strain, and thickness sensors relationship

Since the cycling results show a somewhat constant behavior as far as the curve profile for both the strain and thickness measurements, further comparison and conclusions can be made between the thickness and strain sensors. Figure 3.13 shows a single cycle CCCV with the secondary y-axis corresponding to both the normalized values for thickness and strain. Understanding how the profiles differ between the two is critical to making a control decision for the EMS to integrate this technology as an SOC adjustment model.

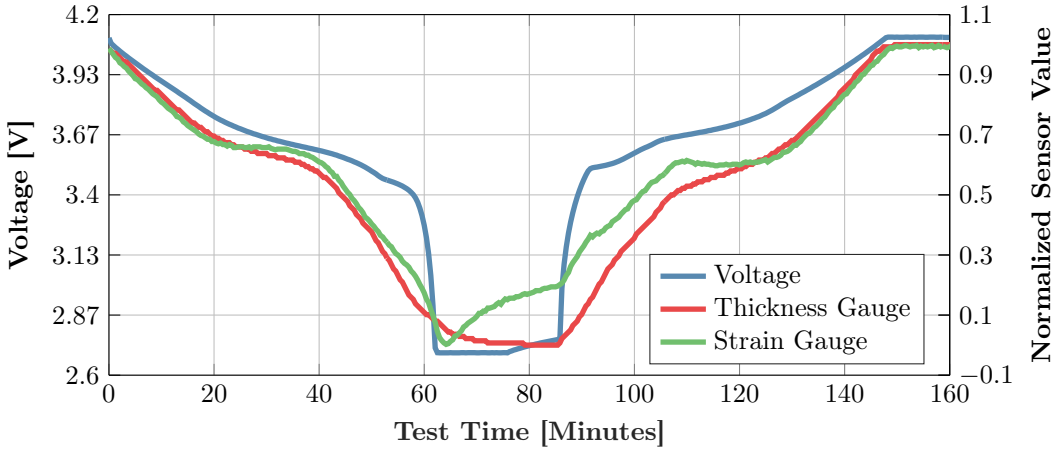

Figure 3.13: Single cycle look at voltage, strain, and thickness sensors relationship

Results from Figure 3.13 show that a somewhat similar profile between the thickness and strain sensors is evident, however some points differ which needs to be fully understood in order to allow EMS decisions to be made. However, the most important aspect of this results to keep in mind is the initial goal to understand the viability of integrating a strain gauge directly onto the specific battery. The results from the data shown allows reasonable conclusion that the battery itself shows enough battery dimensional changes to allow a strain gauge to be directly placed on the battery to correlate the strain change (battery dimensional change) to the battery voltage, and ultimately to the battery SOC in real-time. Now that the strain sensors, and thickness sensors, are believed to be adequate measurement devices to correlate to SOC, a study needs to be performed to understand the model differences between how the OCV polarization behaves throughout rest periods (following a charge/discharge event) and how the strain/thickness measurements behave. Ideally, the strain/thickness sensors show no polarization behavior alternatively to how the OCV behaves, which would show significant potential for this concept's need to be implemented for almost any battery related application where strict SOC monitoring is needed for safe performance.

3.3 Comparison of OCV & Dimensional Change Lookup Methods for SOC

Previous sections performed experiments to understand how strain gauges, and thickness gauges could be implemented on a battery to relate to voltage (and ultimately SOC). In this section, further investigation was performed to understand how the battery dimensional changes was effected following a discharge event. In applications, an SOC adjustment is performed in periods of rest to update the values of SOC for batteries in the system. If the battery dimensional changes does not polarize much like the voltage does, than a more instantaneous SOC adjustment protocol can be performed.

In order to study this polarization behavior, an experiment needs to be performed to analyze the various signals post discharge event during a long rest period. To do this, a 0.5 C-Rate was applied to a battery until 0.5Ah were discharged. At this point, a 2 hour rest period was performed while recording data across all systems. Figure 3.14 shows the results of this study, where the voltage corresponds to the primary y-axis, and the strain and thickness gauge (normalized values in order to plot together) are represented by the secondary y-axis. Additionally, note that the strain gauge data plotted in this figure corresponds to the strain gauge located on the vent area (denoted previously as "strain gauge 3").

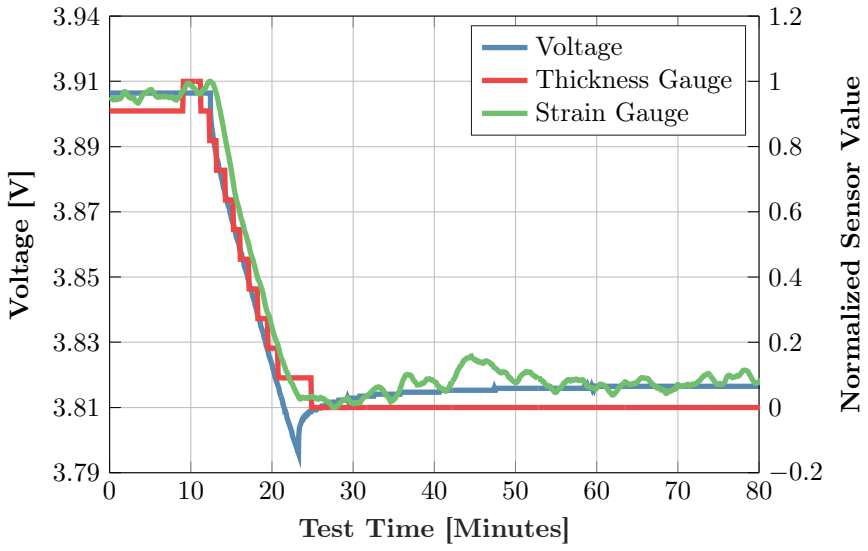

Figure 3.14: Discharge pulse (0.5 C-Rate) followed by 1 hour rest period to understand polarization of battery dimensional change relative to voltage polarization.

Analyzing this plot results in numerous conclusions and observations that need to be made. First off, the thickness gauge seems to have a stepping function behavior as the discharge event was performed. This can be explained by the Mitutoyo position gauge accuracy, where the resolution in mm that the gauge reports is limited to 0.05mm. The relative change of the battery dimension results in the position gauge recording this step like behavior, however it is reasonable to conclude that if a position gauge was employed with more accuracy, a smooth profile would be found. The next key observation is the behavior of both dimensional change sensors following the discharge event. The voltage immediately polarizes back to its steady state value, however, it takes at least 20-30 minutes until the polarization is minimized to a value that an SOC adjustment could be performed. Most importantly, the thickness and strain gauges do not seem to polarize much at all. It is believed that the fluctuations in the strain gauge can be attributed to temperature effects on the surface of the battery. Following the discharge event, the battery temperature has risen slightly, and as the discharge event concludes, the battery temperature will reduce gradually back to ambient. If employing temperature compensation as well as other strain gauge optimization techniques, it is reasonable to believe that the profile found in the thickness sensor could be obtained by the strain gauge sensors.

Results from Figure 3.14 provide significant evidence that the battery dimensional changes could be used as an SOC adjustment protocol much like OCV. However, from the figure, the thickness sensor showed no polarization following the discharge event beyond approximately 1 minute of rest. With this result, the battery dimensional change could provide much more time efficient SOC lookup methods in to contrast remaining at rest for additional time to utilize OCV.

3.4 Chapter Summary

This chapter introduced and analyzed the potential integration of strain gauges locally to a battery in order to correlate to an SOC measurement. Introduced previously in Literature, thickness measurements of batteries were performed, and found to track the voltage profile

of a battery quite well. Additionally, some research has been conducted focusing on using strain gauges instead of a thickness measurement, however, the strain gauges were never used locally on a battery. The strain gauges were typically a lumped sum measurement of 5-6 batteries. The focus of this study was to investigate that a strain gauge could be placed locally on a battery, and have the resolution needed to still track the voltage profile previously identified in literature.

This chapter showed experiments where multiple strain gauges were placed on a battery, alongside the traditional thickness measurement system to track the battery dimensional changes while testing the battery. First and foremost, the experiments showed that a strain gauge could be placed locally on a battery and track the voltage profile, ultimately leading to allowing the strain to SOC correlation we were looking for. Looking further, there are many aspects to this technology that need further investigation and optimization to make this a commercially viable option.

Perhaps the most important observation was the significance of the strain gauge location selected, which showed the potential for a specially designed battery casing for the optimized sensor design. The location where the vent was located showed significantly better visibility of the strain measurement, which lead to the desire to design the battery case in the future for a smooth, idealized case thickness to allow optimal strain readings.

Future work that needs to be performed is to continue investigations into the signal behavior when the battery goes to rest. This work was unable to be performed under the scope of this research, but investing additional time and financial resources to reduce signal error by multiple methods. The first is investing in industrial grade strain gauge measurement data acquisition, but then additionally optimizing the strain gauge adhesion process alongside adding temperature compensation to the strain system. By improving these qualities, the confidence in the measurement results will increase, and lead to confident EMS decisions based on the strain-SOC correlation that will be derived.

Chapter 4

Dynamic Reconfiguration in Large Battery Systems

4.1 State of Health Minded Dynamic Reconfiguration Model

The concept of DR at its fundamental level was introduced previously in Section 1.5.3. In this chapter, DR will be employed in a simulation based environment to study potential performance improvements in comparison to traditional static configuration based battery systems. Before understanding these improvements, the basic simulation model must be introduced to understand the systematic equations, as well as key nomenclature that will be used throughout this chapter.

4.1.1 Battery Simulation Model Breakdown

Figure 4.1 shows the block diagram schematic that each individual cell in the battery system employs [65]. Note that all variables listed in this schematic, as well as the equations listed below are also defined in the list of symbols section (1). Additionally, the parameters will be discussed in this section relative to each equation presented. The first set of equations to introduce are Equations 4.1 - 4.2 which correspond to the functions for Discharge and Charge Models evaluated, respectively. To fully understand the variables listed in the equations, exploration in [65] will provide detailed explanation for parameter extraction of each specific variable.

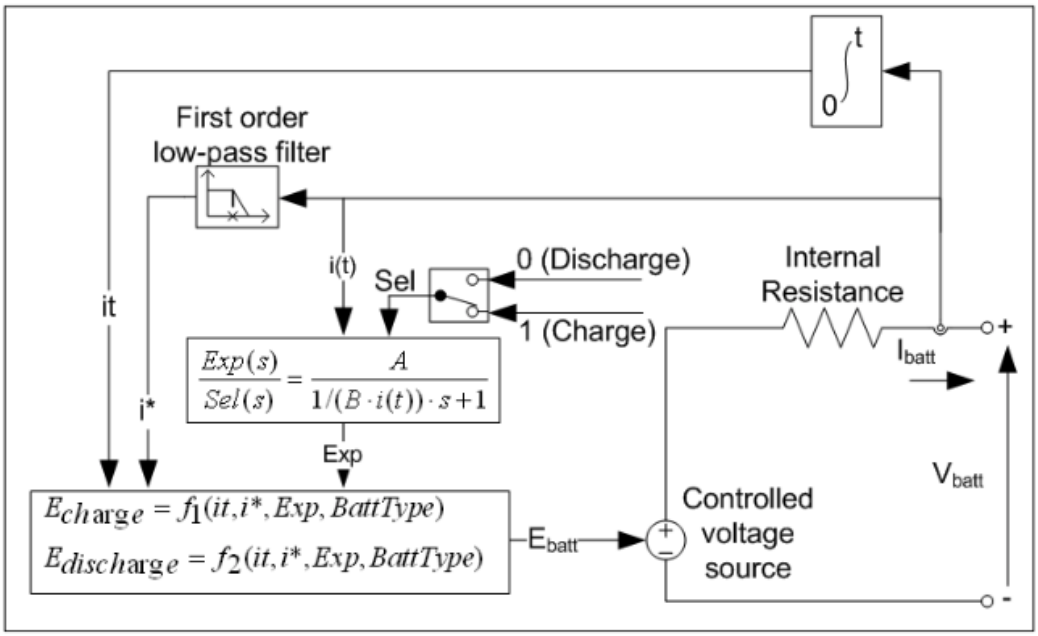

Figure 4.1: Control schematic employed for generic battery model in Simulink [65]

$$f_1(it, i*, i, T, T_a) = E_0(T) - K(T) * \frac{Q(T_a)}{Q(T_a) - it} * (i* + it) + A * exp(-B * it) - C * it \quad (4.1)$$

$$\begin{aligned} f_2(it, i*, i, T, T_a) &= E_0(T) - K(T) * \frac{Q(T_a)}{it + 0.1 * Q(T_a)} * it \\ &- K(T) * \frac{Q(T_a)}{Q(T_a) - it} * it + A * exp(-B * it) - C * it \end{aligned} \quad (4.2)$$

Since many parameters in the charge and discharge model equations are temperature dependent, the derivation of these parameters must be defined in order to compensate for temperature effects. Equations 4.3-4.9 were utilized to define the nonlinear battery voltage, constant battery voltage, polarization constant, maximum battery capacity, and the battery internal resistance, cell temperature, and cell power losses, respectively for the temperature input into the model. The evaluation of these equations were critical in order to evaluate the charge and discharge models previously defined.

$$V_{batt}(T) = f_1(it, i*, i, T, T_a) - R(T) * i \quad (4.3)$$

$$E_0(T) = E_0|_{\mathrm{T_{ref}}} + \frac{\partial E}{\partial T}(T - T_{\mathrm{ref}}) \tag{4.4}$$

$$K(T) = K|_{\mathrm{T_{ref}}} * exp\left(\alpha\left(\frac{1}{T} - \frac{1}{T_{\mathrm{ref}}}\right)\right) \tag{4.5}$$

$$Q(T_{\mathrm{a}}) = Q|_{\mathrm{T_a}} + \frac{\Delta Q}{\Delta T} * (T_{\mathrm{a}} - T_{\mathrm{ref}}) \tag{4.6}$$

$$R(T) = R|_{\mathrm{T_{ref}}} * exp\left(\beta\left(\frac{1}{T} - \frac{1}{T_{\mathrm{ref}}}\right)\right) \tag{4.7}$$

$$T(t) = L^{-1}\left(\frac{P_{\mathrm{loss}} R_{\mathrm{th}} + T_{\mathrm{a}}}{1 + s * t_{\mathrm{c}}}\right) \tag{4.8}$$

$$P_{\mathrm{loss}} = (E_0(T) - V_{\mathrm{batt}}(T)) * i + \frac{\partial E}{\partial T} * i * T \tag{4.9}$$

All of the equations introduced previously were utilized in real time evaluation of the current state of the batteries during any charge/discharge event. However, to truly understand the lifetime performance improvements of the DR concept, there needs to be an aging model to systematically degrade the battery performance based on the charge/discharge severity employed in the system. In order to accomplish this, the introduction of equations centered around the aging of the battery needs to be employed. Again, the variables nomenclature can be found in the List of Symbols section at the beginning of this thesis (1). First, Equation 4.10 describes the battery aging factor for the individual battery, that is ran in parallel to the previously listed equations. The aging model is evaluated at a given sampling rate, that can be the same as other parameters, or altered to be evaluated incrementally to reduce computation complexity. In order to evaluate Equation 4.10, additional equations need to be evaluated, and introduced to do so. Equation 4.11, and Equation 4.12 were used to define the maximum cycles until battery failure, as well as the SOC calculation of the battery.

$$\varepsilon(n) = \begin{cases} \varepsilon(n-1) + \frac{0.5}{N(n-1)}\left(2 - \frac{DOD(n-2)+DOD(n)}{DOD(n-1)}\right), & \text{if } k/2 \neq 0. \\ \varepsilon(n-1), & \text{otherwise.} \end{cases} \tag{4.10}$$

$$N(n) = H\left(\frac{DOD(n)}{100}\right)^{-\xi} * exp\left(-\psi\left(\frac{1}{T_{\text{ref}}} - \frac{1}{T_{\text{a}}(n)}\right)\right) * (I_{dis_ave}(n))^{-\gamma_1} * (I_{ch_ave}(n))^{-\gamma_2} \tag{4.11}$$

$$SOC = 100\left(1 - \frac{1}{Q}\int_0^t i(t)dt\right) \tag{4.12}$$

4.1.2 Graph Theory Representation for Obtaining Configuration Options

The model that was employed consisted of a set number of batteries connected together in predetermined configurations to support a load. In order to connect these batteries together, the graph theory representation discussed in Section 1.5.3 was be used to determine any and all configurations that can be made based on the number of switches implemented in the system. The number of SPC is a key metric to understanding the respective performance improvement that the battery system will see in contrast to the static configuration. In these models, every battery will have a minimum of two switches which were used to connect the individual battery to the positive and negative terminals of the battery pack. The additional switches added provide new configurations by adding series connections from one battery to another. For a visual representation, Figure 4.2 shows a 6 cell system. The legend in the picture depicts the color scheme used to show the system configuration options. Note the light grey lines indicate that a switch is employed as a series line connection between the two batteries. The maximum performance situation will occur when every battery has a switch to connect in series with all of the batteries in the system. As the number of SPC

is increased, intuitively one would think the performance benefit of DR will increase due to the increased number of configuration options in the system.

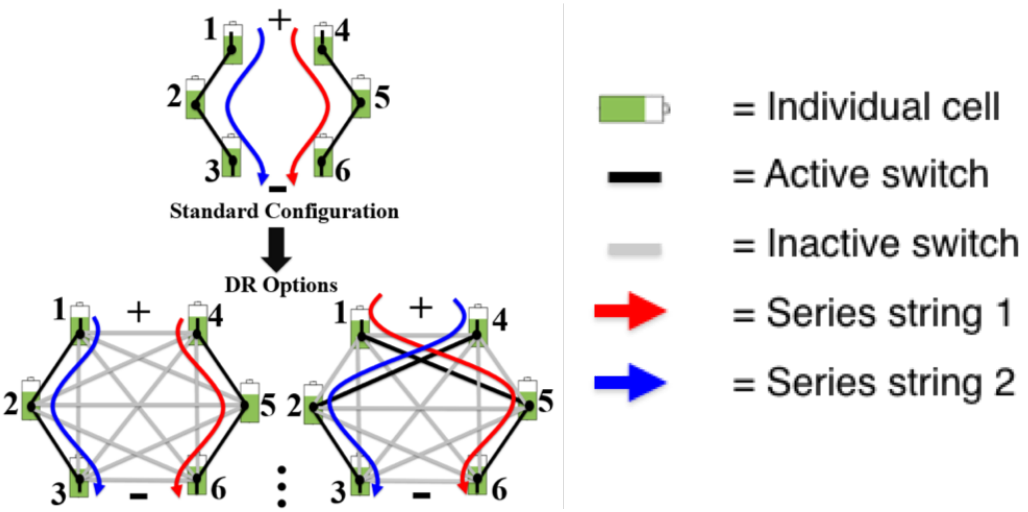

Figure 4.2: Visual description of configuration options for a 6 cell system based on switch implementation

Figure 4.2 shows two potentially different configurations that could be employed in the 6 cell system with the specific switches implemented in the system. If the number of switches in the system were decreased, either of these two configurations could become invalid, which would result in lower performance improvement due to the non-ideal utilization of a configuration at a given simulation time. For the research discussed in the remainder of this section, it is important to understand how the number of SPC would impact the potential performance improvement that would be seen utilizing DR. Subsequent sections will analyze simulation results for the 8 battery system, but before being able to simulate the battery systems, the configuration options need to be identified for the DR controller to use throughout the simulation. Table 4.1 shows the overall number of configurations available based on two criteria's. The first, is the overall number of SPC metric, which is intuitively directly tied to the potential performance improvement. The second, is the number of parallel strings that the system will operate in. The more cells in the system, relative to the number of parallel strings will indicate the potential configurations available to the DR controller.

Understanding the significance of Table 4.1 is critical before examining the results of the simulations. As the number of switches in the system increases, the total configurations increases at a much larger rate proportional to the increase in number of switches. However,

Table 4.1: Configuration options based on SPC metric for 8 and 16 cell systems

Switches Per Cell	**2 Parallel Strings**		**4 Parallel Strings**		**8 Parallel Strings**	
	8 Cell	**16 Cell**	**8 Cell**	**16 Cell**	**8 Cell**	**16 Cell**
3	1	1	1	1	-	1
4	4	8	5	30	-	34
5	21	918	16	1,137	-	491
6	32	3,545	35	10,191	-	3,116
7	35	5,370	63	69,350	-	12,483
8	35	6,132	90	329,424	-	36,500
9	35	6,373	105	877,691	-	86,311
10	35	6,428	105	1,515,132	-	180,560

understanding that as the number of configurations gets large, the overall performance improvement can saturate due to the extremely high number of configurations available. When analyzing the simulation results, understanding the performance benefits for the SPC groups were critical to understanding how to cost effectively retain a low cost product, while still obtaining the maximum performance benefits available.

4.1.3 Simulation Model Design

The design of the simulation model was performed in Simulink, by utilizing the simpowersystems Toolbox. The model is visually simplified by utilizing the subsystem blocks, and the overall breakdown of the model will be performed here. Figure 4.3 shows the model in its simplest form, with a battery pack subsystem coupled with a controlled current source. The controlled current source accepts a commanded current ($i*$), which can be either positive or negative to signify the battery pack either charging, or discharging, respectively. The commanded current ($i*$) is supplied from the system controller, which also decides the system configuration and sets the command for all switches in the model.

Figure 4.4 shows the subsystem for the battery pack that was utilized in Figure 4.3. While this schematic can be quite complex, the ideology behind the connections is rather

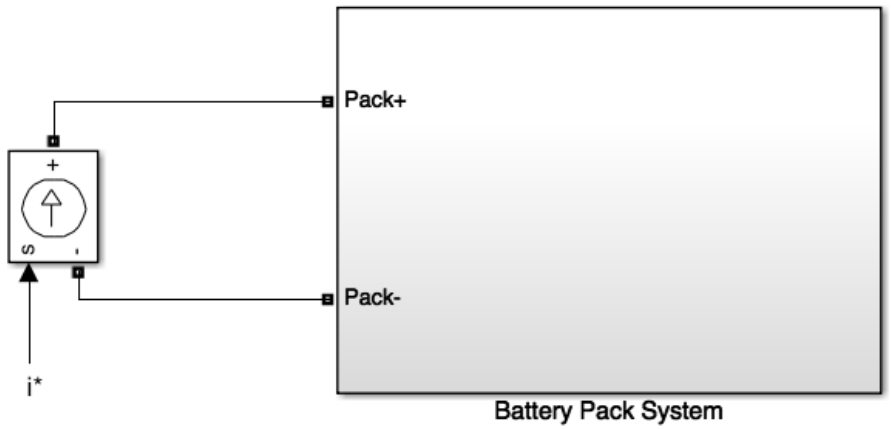

Figure 4.3: DR Simulation Model showing connection from battery pack to operating load/source.

straight forward. This model has 8 batteries in the system, with a balancing controller connected to all terminals of the batteries. The overall system controller decides when to perform balancing, and if necessary, the balancing controller will begin operation. The balancing schematic will be discussed below. Each of the batteries in Figure 4.4 contain the same subsystem, and each connection is set in a intuitive manner. Each battery has two switches to connect to the battery pack positive and negative terminals. In addition, there is a switch that is connected in series to connect each battery in the system to all other batteries. Based on the simulation running, some switches may be valid to use, and some not. This is determined by the criteria for the simulation that is being ran. Discussed previously, the number of SPC, and ultimately the total number of configurations is resulting in the number of switches in the system. For simulations where not all switches were used, the model simply doesn't ever utilize them. By doing this, the same model is able to be utilized for all switch option situations, making autonomous simulation programming much less complex.

Figure 4.4 showed the battery pack system, which contained additional subsystems for each battery. Figure 4.5 shows the subsystem for each battery, with the battery block connected to numerous physical connections. Each connection out of the battery subsystem is connecting to a different battery in the battery pack, with a power electronic switch to connect between them. In addition to each of the series connections, the individual battery terminals have connections for positive and negative pack terminals, in addition to the

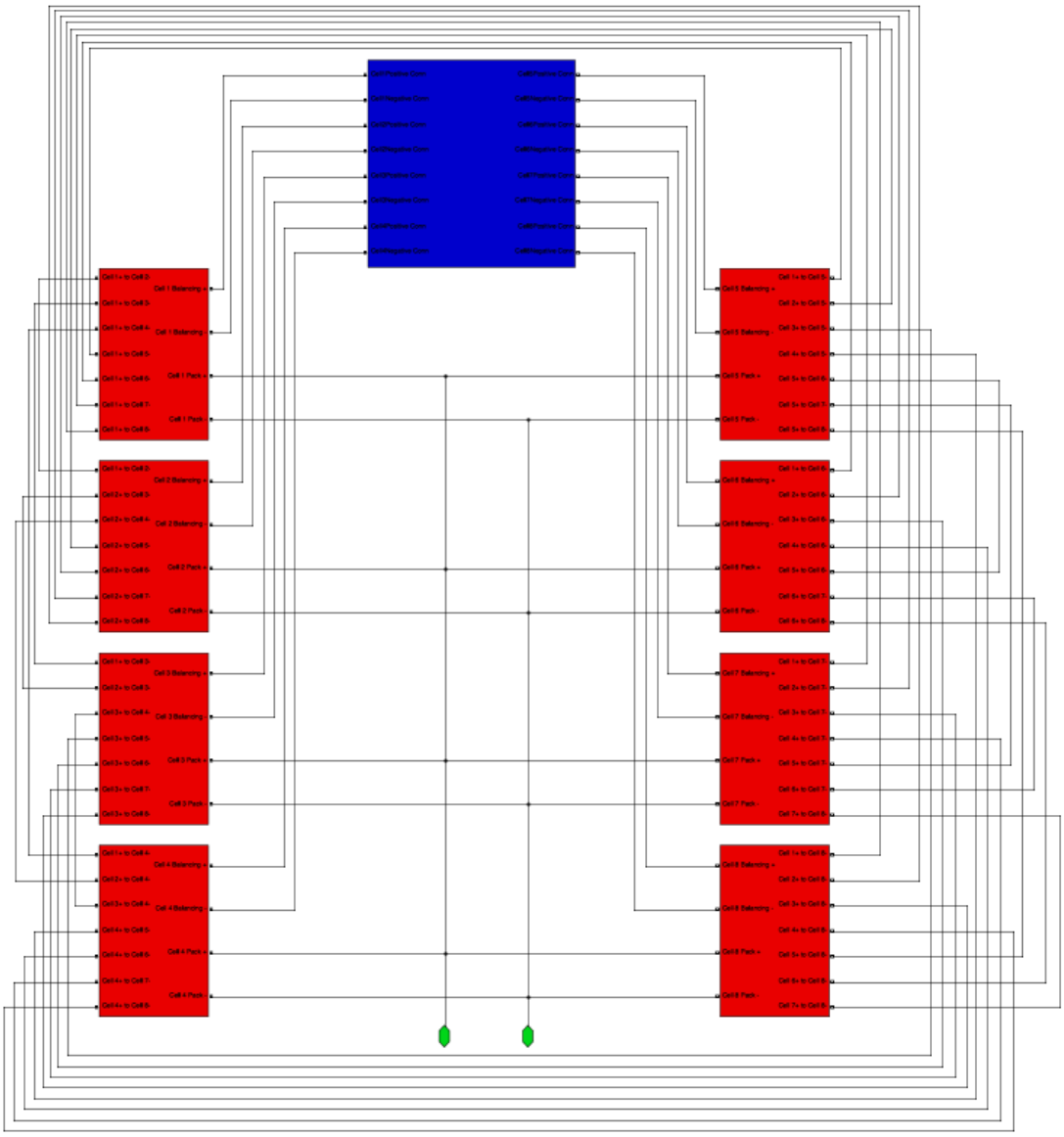

Figure 4.4: DR Simulation Model showing the subsystem used for the battery pack. Red indicates a subsystem for a cell/battery, blue for the balancing subsystem, and green for the pack positive/negative terminals

positive and negative balancing connections.

The balancing circuit that connects individually to each battery in the system is shown in Figure 4.6. The simplest balancing system was employed in this simulation setup as a passive resistive balancing topology. The commanded current $i*$ in the figure is the rate at which the controller decides to discharge the individual battery to align the voltage to be within the set tolerance specification.

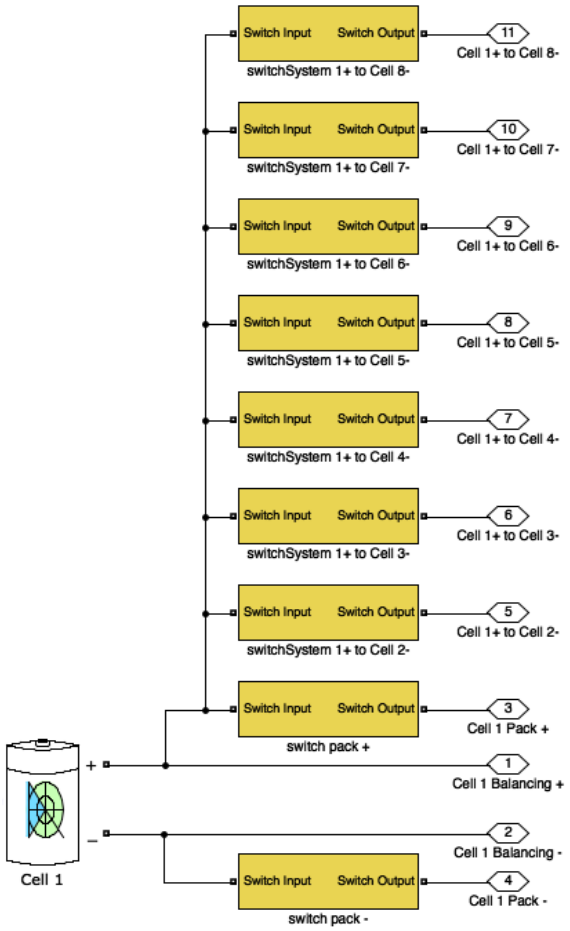

Figure 4.5: DR Simulation Model showing the subsystem used for the cell blocks. Yellow indicates the subsystem for a power electronic switch in the system to connect to another cell/battery.

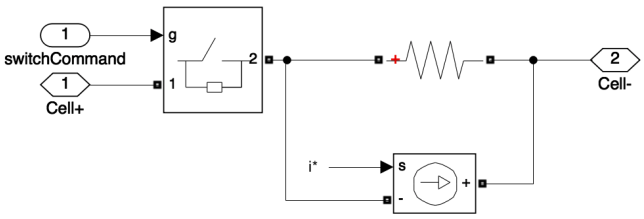

Figure 4.6: DR Simulation Model showing the subsystem used for the balancing circuit

The simulation model outlined above was created in a way to allow extensive customization of the simulation parameters without altering physical design, structure or operation methodology. The various parameters and criterion able to alter programmatically were discussed in the following section prior to analysis of the results.

4.2 Performance Improvements of Dynamic Reconfiguration compared to traditional

To understand any performance improvement for DR compared to traditional static configurations, several criteria needs to be chosen as unique attributes to study. The selected criteria were chosen as key attributes for a battery pack's operation across a wide range of applications. The focus of this research targets automotive applications, but also has considered grid applications in some niche conditions. Table 4.2 shows the different variables that were being simulated for this experiment. The benefit of conducting this research in a simulation environment is the extensive amount of variable conditions we were able to explore without containing a large expense to purchase batteries, BMS systems, and testing equipment to run the various conditions.

Table 4.2: Simulation variables for eight cell system

Parameter	Specification Tested
Pack Configuration	4S2P, 2S4P
Switches per Cell	4, 5, 6, 7, 8, maximum condition
Balancing Voltage Specification	30mV, 40mV, 50mV
Capacity Condition	Constant, 2% Variation
SOH Condition	Constant, 2% Variation, 1(2, 3, 4, 5) Fresh amongst aged
C-Rate	5C, 2C, 1C
Simulation Type	Static, Dynamic

Understanding the nomenclature in Table 4.2 is critical prior to analyzing the results of the simulations. The "Pack Configuration" parameter signifies the series-parallel topology that the system will operate in. For example, "4S2P" stands for 4 Series 2 Parallel, which means that the system contains 2 parallel strings, each with 4 batteries in series. The "Switches per Cell" (SPC) parameter means how many switches were in the system relative to each battery. Note, that each battery has two switches for the pack positive and pack negative connections, and any additional switches signifies series connections between batteries. Recalling Table 4.1, as the number of SPC increases, the configurations options also increases significantly. The "Balancing Voltage Specification" signifies the tolerance of voltage difference between the batteries at the end of the discharge event for every cycle.

The smaller the tolerance, the more balancing will likely occur. The "Capacity Condition" signifies the initial condition that the simulation begins with relative to the battery rated capacities in the system. The constant value signifies that all batteries have exactly the same rated capacity, which is an ideal case and doesn't happen practically. The 2% variation case means that a 2% standard deviation across the batteries in the system for the initial condition of rated capacity. The parameter "SOH Condition" is similar to the capacity condition for both constant and 2% variation specifications, but has some extra conditions that would need further explanation. The 1 Fresh amongst aged signifies the condition that there is 1 fresh battery and the rest of the batteries in the system were aged to 85% SOH. This condition is how the simulation starts, and acts as an initial condition for SOH. Then, instead of 1 fresh battery, additional simulations were ran for having 2 fresh batteries (for an 8 battery system, consequently then 6 batteries would be aged), and then having 3 fresh, and so on. The parameter "C-Rate" is rather intuitive, and we were basically executing simulations where the individual batteries will see a 5C, 2C, and 1C current throughout the simulation both on charging and discharging. The last parameter is "Simulation Type", which basically means Static or Dynamic. For Static, this is considered the traditional Metal Bus-Bar connections to get the series-parallel topology that we want. While the Dynamic option is allowing the use of power electronic switches to dynamically control the series-parallel topology, as well as the individual battery location in each of the target configurations.

4.2.1 Ideal Case Comparison Static vs Dynamic Reconfiguration

Now that the unique simulations have been introduced along with the important nomenclature associated with it, the comparison for performance improvement of DR to static configurations can be done. Before investigating performance impact based on the number of SPC criteria, understanding how the DR concept performs in comparison to static in the simplest form is critical. For this to be done, the static simulations were directly compared to the DR - max condition. Recall, that the max condition utilizes the maximum number of SPC, meaning that every battery can series connect to every battery in the system. This

condition isn't practical, since as battery system's cell count increases, the needed power electronic switches increases significantly (Recall Table 4.1). However, based on the theory of this concept, this condition should show the most performance improvement which is an essential first step in understanding DR enhancements.

Table 4.3 shows the simulation results for the 8 battery system when the initial conditions for the 8 batteries were set to have constant capacity and SOH. This means that there is no variation at the start of the simulation. Note, that this is an extremely ideal case, as many battery manufacturers, like Johnson Controls, has to essentially "bin" sort their batteries at the plant prior to integrating into battery packs. Even when mass producing, there is always slight variation in terms of performance, actual battery capacity, and other aspects. The reason for simulating this ideal case is to understand the outcome of the DR model in a fully ideal situation.

Table 4.3: Simulation results for total energy delivered to the load in kWh under conditions: 4S2P configuration topology, constant SOH and Capacity for initial conditions, 30mV balancing tolerance, and DR max configuration options.

Model	5C-Rate	2C-Rate	1C-Rate
Static	84.834	131.368	190.975
Dynamic	83.863	129.591	186.915

Thoroughly understanding the results in Table 4.3 is an important first step to truly understanding where DR can benefit battery systems. Initially examining the table of results, in all C-Rates that were tested, the static model delivered more energy to the load than the DR - max conditions case. At first, this may be troublesome, as DR would be expected to perform superior than static configuration in all cases. However, understanding what the DR model changes to achieve this reconfiguration capability is critical. By employing all of these power electronic switches in the system, a new loss mechanism is added to the system. By adding large amounts of switches, the amount of losses increases as well, meaning that in order to have the end performance between static and DR to be the same, the DR has to perform better to counteract the additional losses in the system. Additionally, the way that DR extends performance is by changing the configuration to a better configuration option at any given time. In this simulation case, all of the cells start with the same aging and

capacity, so in order for a new configuration to be selected by the controller, the cells need to age nonlinearly to a point where the same configuration is no longer best. By examining the results in Table 4.3, it is clear that the cells had minimal variation, resulting in no need for a new configuration in order to drastically change the performance enough to counteract the additional switches in the system.

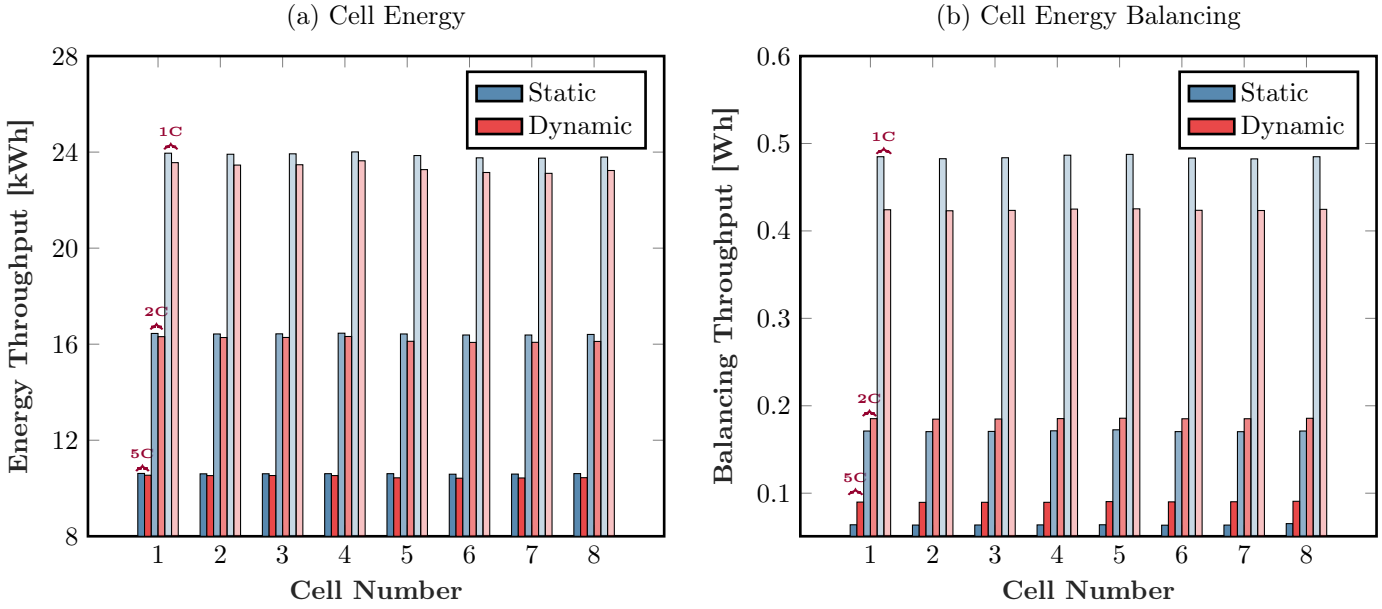

Figure 4.7: Simulation results for (a) total energy of the cells in kWh across the 8 cell system and (b) balancing energy in Wh under conditions: 4S2P configuration topology, constant SOH and Capacity for initial conditions, 30mV balancing tolerance, and DR max configuration options

After understanding the results based on the total energy delivered to the load, examining the energy throughput for each individual battery is necessary to understand any additional performance alterations based on DR. Figure 4.7 shows the total energy for each cell in the system that was simulated for 5C, 2C, and 1C rates denoted in (a). Note that each cell number has 6 bar plots, with two corresponding to each C-Rate tested. The order of these bars based on C-Rate is signified for battery 1, and applies for all. This structure will be utilized for multiple plots in this section. For each C-Rate, the static and DR simulation result is shown. For this extremely ideal case, the variation in performance from cell to cell during the same simulation does not vary significantly, which makes sense due to the DR performance effect occurring most when cell variation is evident. Figure 4.7 denoted in part (b) shows the balancing losses for each cell during the same simulation conditions.

Further examination of Figure 4.7 (b) shows some interesting results. Under the higher rate conditions (5C-Rate, 2C-Rate), the DR simulation shows more balancing losses than the static model. This means that by switching the configuration significantly when the cell variation isn't significant, that the DR model is being over-utilized, and not achieving the performance benefit desired. Since this was a very ideal situation that isn't practical, the exploration of a more "real-world" case is important to understand if there is any potential benefit when using DR topologies.

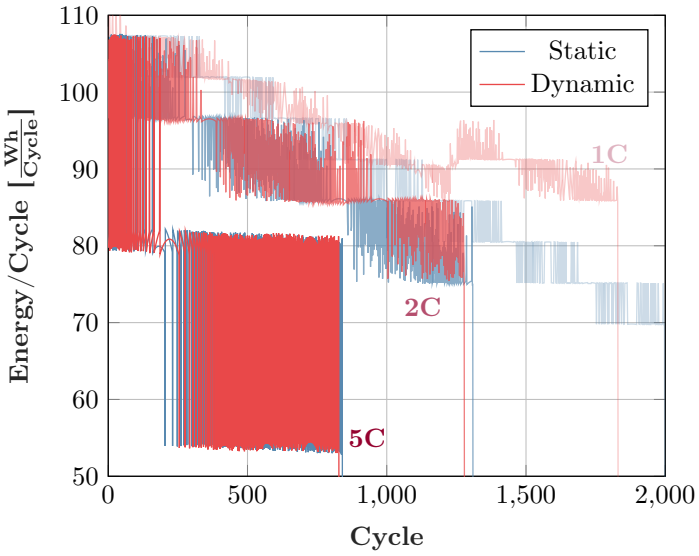

Figure 4.8: Comparison of static vs dynamic models under the maximum SPC condition across multiple C-Rates for the ideal condition (initial conditions of constant SOH and capacity). Each C-Rate is labeled in the figure, where both static, and dynamic simulations results were plotted. The data shows the total energy delivered to the load for each cycle.

While examining the final values of the simulations provides adequate insight into the integration of the dynamic reconfiguration topology, understanding the behavior throughout simulations was performed. Figure 4.8 shows the total energy delivered to the load during each cycle for each of the three C-Rates tested (5C, 2C, 1C). Note that the 5C-Rate results seem to be virtually the same for both static and dynamic conditions. However, the dynamic model starts to deliver more energy per cycle as the total cycles increases for the lower C-Rate conditions shown in the figure. Although, recall that the dynamic model under these ideal conditions do not provide the performance enhancement expected in comparison to the static model. Beyond just the final deliverable energy, examining the average energy throughput across the 8 cells in the system was performed.

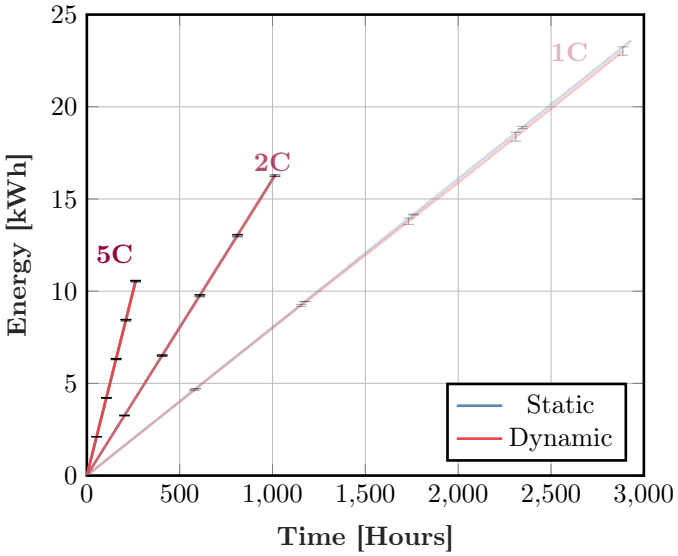

Figure 4.9: Comparison of static vs dynamic models under the maximum SPC condition across multiple C-Rates for the ideal condition (initial conditions of constant SOH and capacity). Each C-Rate is labeled in the figure, where both static, and dynamic simulations results were plotted. The data shows the average energy throughput (with error bars to signify standard deviations) across the 8 cells in the system.

Figure 4.9 shows the average energy throughput across the 8 cells in the system (with error bars indicating the standard deviation), for the numerous C-Rates across static and dynamic simulations. Note that the static and dynamic models seem to have identical behavior throughout the simulations, but closer analysis shows that the standard deviation for the dynamic model is lower than the static model as the simulation evaluates. An important note for this plot is that the x-axis is in time, and the y-axis is a running total of energy throughput, unlike Figure 4.8 where the data showed the energy per cycle. Since the results in Figure 4.9 were hard to differentiate a relationship between static and dynamic, the separation of cell energy throughput per cycle was performed.

Figure 4.10 shows the average cell energy throughput per cycle (with error bars indicating standard deviation), for both static and dynamic conditions. Note that for each of the C-Rates, the static model shows a rather smooth, linear performance throughout the system's cycle life. However, the dynamic model shows a significant point about halfway through the simulation, where the average value of energy per cycle increases, which was resultant of the controller finally finding a better configuration, and began reconfiguring to deliver more energy. Essentially, the variance in the system was so low, that the controller could not find a better configuration to adjust to, until the variance in the system increases over time to where

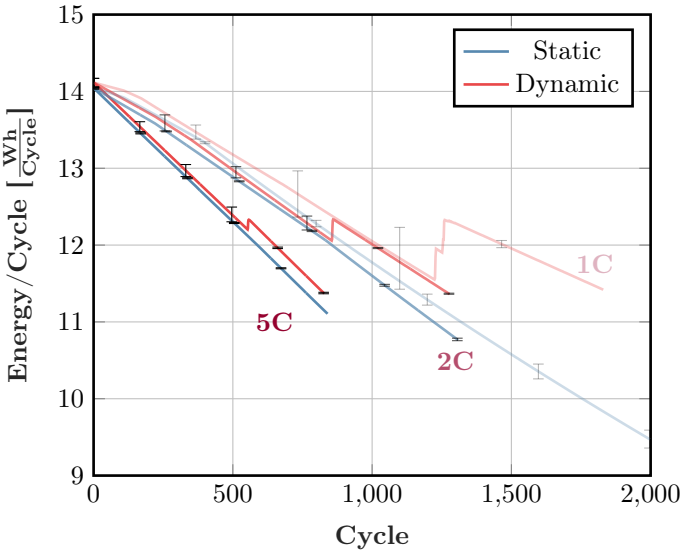

Figure 4.10: Comparison of static vs dynamic models under the maximum SPC condition across multiple C-Rates for the ideal condition (initial conditions of constant SOH and capacity). Each C-Rate is labeled in the figure, where both static, and dynamic simulations results were plotted. The data shows the average energy (per cycle) throughput (with error bars to signify standard deviations) across the 8 cells in the system.

the controller found the opportunity to adjust the configuration for better performance. Note the cycle for which this increase in energy throughput begins for both the 2C and 1C rates on Figure 4.10 was close to the same area in Figure 4.8 began to deliver more energy (per cycle) to the load in comparison to the static condition.

4.2.2 Practical Case Comparison Static vs Dynamic Reconfiguration

Table 4.4 shows the more practical simulation results for the total energy delivered to the load when inducing a 2% variation in both SOH and capacity across the 8 cells in the system. Recall, that previously the DR simulations delivered less energy to the load in all C-Rate conditions, but when inducing the more practical initial aging and capacity, the DR delivers more energy to the load. Now that the system has more cell variability, the DR controller is able too find more optimized configurations and is able to execute the DR topology to begin improving performance at the start of operation. The DR case showed a 3.07% improvement for the 5C-Rate condition, 3.39% improvement for the 2C-Rate condition, and 1.23% improvement for the 1C-Rate condition. Beyond this indication, it is important to note that in the previous few figures, the dynamic model shows an overall reduction in standard deviation relative to the static model under the same test conditions. This reduction

in standard deviation is identified as a potential advantage for the dynamic reconfiguration topology, since the lower standard deviation indicates an overall better utilization of the batteries potential.

Table 4.4: Simulation results for total energy delivered to the load in kWh under conditions: 4S2P configuration topology, 2% variable SOH and Capacity for initial conditions, 30mV balancing tolerance, and DR max configuration options.

Model	5C-Rate	2C-Rate	1C-Rate
Static	76.270	122.403	182.665
Dynamic	78.614	126.549	184.908

Since the DR simulations outperformed the static model with the 2% variation in initial SOH and capacity, further examination of this test condition is necessary to understand any further performance improvements. The 2% variation was decided based on recommendation from Johnson Controls as a typical deviation found in battery systems which was the foundation of reasoning for selecting this condition as the practical case. Figure 4.11 shows the same plot design discussed previously, but now the data corresponds to the 2% variation in initial SOH and capacity case. Recall, that previously (for the constant SOH and capacity initial condition) that the static condition had more energy throughput for each cell, as well as very minimal variation from cell to cell in comparison to the DR case. Examining the figure, the static case shows much more variability from cell to cell performance, especially compared to the DR case.

Table 4.5 shows a statistical analysis for Figure 4.11 (a) in order to quantify the per cell variation in performance across both the static and DR case. This table has two important aspects to take under consideration: First, that the mean value of energy throughput for the cells in the system is superior for the DR case than the static case across all C-Rates. Additionally, the standard deviation across the 8 cells in the system was significantly lower for the DR case than that of the static case. Having more consistent per cell performance is significantly more desirable for a battery management perspective, which could ultimately lead to more predictable and manageable lifetime system performance.

Since the DR case proved to reduce cell variability in the system for total energy throughput, examining the overall cell balancing is important to understand the losses in

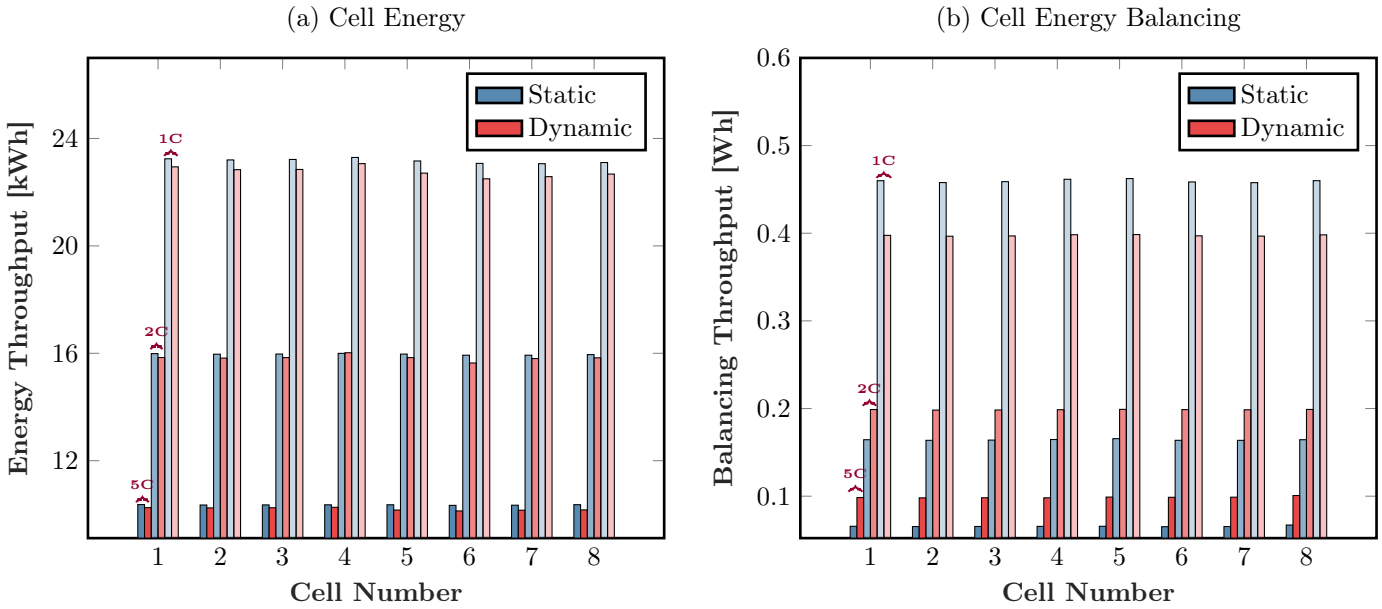

Figure 4.11: Simulation results for (a) total energy of the cells in kWh across the 8 cell system and (b) balancing energy in Wh under conditions: 4S2P configuration topology, 2% variable SOH and Capacity for initial conditions, 30mV balancing tolerance, and DR max configuration options

Table 4.5: Simulation results for total energy of the cells in kWh, with statistics performed (mean and standard deviation) across the 8 cell system under conditions: 4S2P configuration topology, 2% variable SOH and Capacity for initial conditions, 30mV balancing tolerance, and DR max configuration options.

Model	**5 C-Rate**		**2 C-Rate**		**1 C-Rate**	
	Mean	**St. Dev.**	**Mean**	**St. Dev.**	**Mean**	**St. Dev.**
Static	9.53	0.4093	15.30	0.6283	22.83	0.7986
Dynamic	9.83	0.0604	15.82	0.1012	23.11	0.3893

the system. Figure 4.11 (b) shows the balancing energy losses for each of the cells across multiple C-Rates for both the static and DR case. Note that in all cases, the DR simulations result in more cell balancing than the static case. This shouldn't be perceived as a problem, since the changing configurations results in less variation in cell use compared to static. The less variation results in more universal cell balancing throughout the pack.

Increased balancing losses for the DR case can be acceptable based on the performance improvement for the delivered energy to the load. However, understanding potential reasons for the increased deliverable and balancing energy is important for moving forward with this technology. Table 4.6 shows the final value of SOH both in mean and standard deviation values for the simulations ran. For the DR case, the average final value of SOH is lower than the static case across all C-Rate conditions. The failure limit to end the simulations

is when a cell reaches 80% SOH, which is standard failure criteria in applications. By DR allowing the average value of SOH to be lower, the overall energy being delivered is being pushed further than the static case. Not just lower SOH values, but the DR cases show lower standard deviation across the cells in the system, which indicates overall better utilization of the energy capabilities. Additionally, since the cells were being further utilized, the overall balancing needed is increased, which justifies the increased values in cell balancing for the DR case.

Table 4.6: Simulation results for final SOH of the cells, with statistics performed (mean and standard deviation) across the 8 cell system under conditions: 4S2P configuration topology, 2% variable SOH and Capacity for initial conditions, 30mV balancing tolerance, and DR max configuration options.

Model	**5 C-Rate**		**2 C-Rate**		**1 C-Rate**	
	Mean	**St. Dev.**	**Mean**	**St. Dev.**	**Mean**	**St. Dev.**
Static	81.99%	1.9126	81.93%	1.7379	82.81%	2.2297
Dynamic	81.31%	1.2341	80.95%	1.1144	81.21%	0.9480

Examining the final simulation results provide interesting results for the dynamic model under this practical condition, and further examining into the performance differences throughout the simulations was done similar to the analysis previously discussed for the ideal case. Figure 4.12 shows the same figure that was used in the ideal case, but now shows the results for the practical case conditions (2% variation in initial SOH and Capacity across the 8 cells in the system). Note that for all C-Rates tested, the dynamic model delivers more energy per cycle than the static case, where in the ideal case conditions discussed previously, the 5C did not. Additionally, as the cycles increase, the overall separation in performance between the static and dynamic deliverable energy per cycle increased for each respective C-Rate.

Since the more practical case has shown to have enough variability in the system to prove the benefit of DR, examining the performance for the battery utilization in the system was performed. Figure 4.13 corresponds to the total energy throughput (averaged across the 8 cells in the system, with error bars indicating standard deviation), for each of the three C-Rates tested. Note that for the practical case, the performance difference between static and dynamic has enough separation to distinguish a performance difference, where the same figure under the ideal case previously discussed did not. Additionally, note that the standard

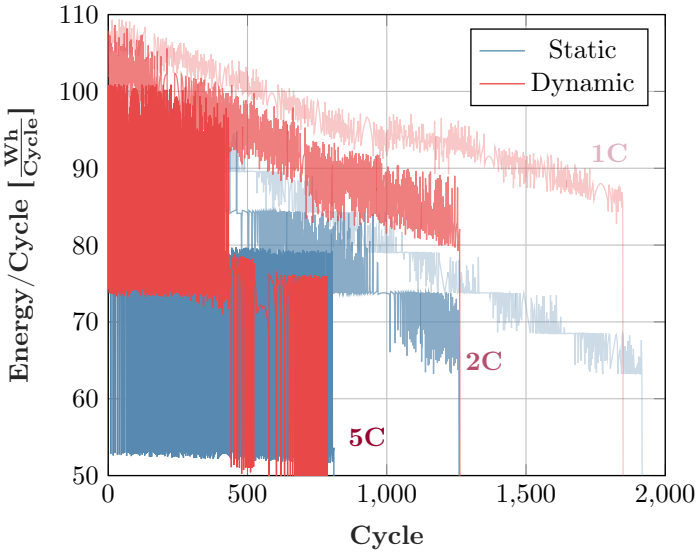

Figure 4.12: Comparison of static vs dynamic models under the maximum SPC condition across multiple C-Rates for the practical condition (initial conditions of 2% variable SOH and capacity). Each C-Rate is labeled in the figure, where both static, and dynamic simulations results were plotted. The data shows the total energy delivered to the load for each cycle.

deviation for the dynamic case was noticeably smaller compared to the static case. Having smaller standard deviation for the cell energy throughput indicates that overall, the battery system is better utilizing its components, rather than wasting potential energy due to cell variance in the system.

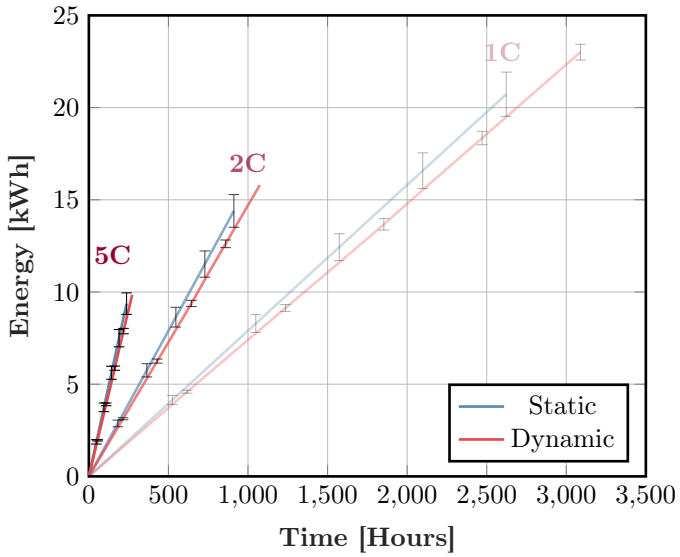

Figure 4.13: Comparison of static vs dynamic models under the maximum SPC condition across multiple C-Rates for the practical condition (initial conditions of 2% variable SOH and capacity). Each C-Rate is labeled in the figure, where both static, and dynamic simulations results were plotted. The data shows the average energy throughput (with error bars to signify standard deviations) across the 8 cells in the system.

The more practical case has shown to have enough variability in the system to begin to reconfigure in order to boost performance, so the analysis was performed again to show the

average cell energy throughput per cycle, in order to see where the dynamic model begins to boost performance with new configuration opportunities. Figure 4.14 corresponds to the simulation results for the average cell energy throughput per cycle (with error bars indicating standard deviation across the 8 cells in the system) for each of the C-Rates tested. Note that the average value of energy per cycle seemed to begin oscillating about midway through the simulations for each of the C-Rates, which indicates that the dynamic models began to find better configurations to reconfigure. Also, it is important to note that the standard deviation is significantly reduced for the dynamic model in comparison to the static model for each of the C-Rates, which is indicated by the error bars in the figure.

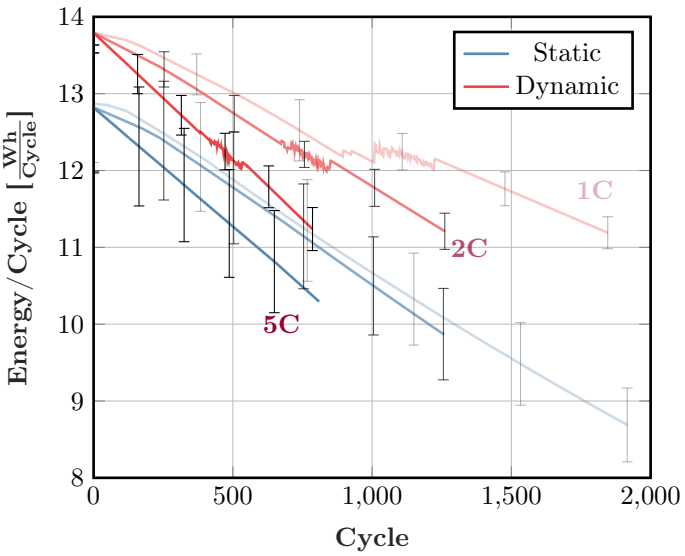

Figure 4.14: Comparison of static vs dynamic models under the maximum SPC condition across multiple C-Rates for the practical condition (initial conditions of 2% variable SOH and capacity). Each C-Rate is labeled in the figure, where both static, and dynamic simulations results were plotted. The data shows the average energy (per cycle) throughput (with error bars to signify standard deviations) across the 8 cells in the system.

Since the performance in this practical case showed that DR started to find better configurations to adjust to about midway through the simulations, understanding the specific configuration selection was performed. Figure 4.15 shows the comparison for both the ideal and practical simulation case to understand how the induced variance in the system (e.g., the practical case) resulted in different configuration selection by the controller. Ultimately, this difference in configuration selection was what results in the change from DR not delivering as much energy to the load as the static (for the ideal condition), to the DR delivering more energy to the load for the DR case (for the practical condition).

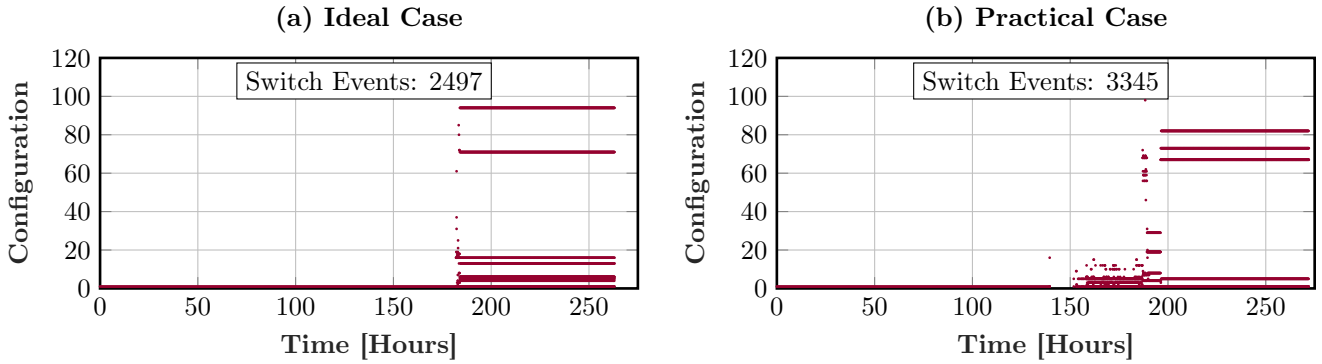

Figure 4.15: Comparison of the configuration choice throughout the simulation for the 5C-Rate condition where (a) corresponds to the ideal case (constant SOH and Capacity as initial conditions), and (b) corresponding to the practical case (2% variation in SOH and Capacity as initial conditions)

Examining the configuration selection in Figure 4.15 results in two main conclusions. First, note the time where the first reconfiguration occurs. For the ideal case, this occurs around a time of 180 hours (simulation time). However, for the practical case, the first reconfiguration occurs around a time of 140 hours. This extra 40 hours of reconfiguring essentially resulted in the change from DR delivering less energy in the ideal condition, to DR delivering more energy in the practical condition. Secondly, note the text box placed in both of the subplots indicating the total number of switch events. For the ideal case, 2,497 reconfigurations occurred, while for the practical case, 3,345 reconfiguration events occurred. By having more reconfiguration events, this means that the controller found significantly more opportunities to deliver more energy just between this ideal and practical case. However, note that in comparison to the static condition, by having more than 2-3 thousand opportunities where the initial configuration was not the optimum, this acts as an essential proof of concept that DR has performance enhancement opportunities.

After analyzing both the ideal case, and the practical case the DR topology has proven to provide some performance improvement, while the true improvement is found when larger variability amongst the cells in the system can be found. Since variability seems to play the larger role, investigating specific applications that invoke larger variabilities is a necessary next step.

4.2.3 Distributed Energy Storage - Dynamic Reconfiguration Opportunities

Johnson Controls (our research sponsor) discussed the standard protocol when a cell fails in a module for the grid related DES systems. According to them, replacing a single cell in a module is too expensive in terms of training technicians to replace a single cell. So, they replace the entire module in the system with a new (fresh) module of batteries. When placing a fresh module alongside already aged modules, the full utilization of the fresh module will not occur. DR gives promise to better utilizing the fresh modules by reconfiguring the modules to better work together. For this case, simulations were performed by treating the individual cells as the modules, and by placing fresh cells amongst already aged cells in order to understand if DR can provide any performance improvement compared to the static version.

The case to study this DES application is the simplest condition in which 1 module starts the simulation with the fresh 100% SOH condition, while the rest were "aged", and in this case the aged modules were set to 85% SOH. Recall, that the simulation completes when any cell in the system reaches 80% SOH. Table 4.7 shows the simulation results for this condition for both static and DR cases under various C-Rates. In all C-Rate conditions, the DR cases deliver more energy to the load. The DR case showed a 5.48% improvement for the 5C-Rate condition, 7.52% improvement for the 2C-Rate condition, and 6.31% improvement for the 1C-Rate condition.

Table 4.7: Simulation results for total energy delivered to the load in kWh under conditions: 4S2P configuration topology, 1 fresh cell with rest aged, 2% variable capacity for initial conditions, 30mV balancing tolerance, and DR max configuration options.

Model	5C-Rate	2C-Rate	1C-Rate
Static	17.709	27.695	40.283
Dynamic	18.680	29.776	42.824

Further examination for the 1 fresh cell placed amongst aged cells in the system requires the understanding of cell to cell performance variation for both static and DR cases. However, at this point, the goal is to understand if DR provides any performance enhancement

under maximum SPC conditions in contrast with the static model. Table 4.7 certainly shows that more energy is delivered to the load across all C-Rates, and needs to be explored further. However, understanding if there is any performance enhancement for SPC conditions less than the maximum situation needs to be evaluated.

4.3 Investigation of Configuration Flexibility Correlation to Performance Benefits

In previous sections, the performance improvement for DR compared to static was investigated via simulation. Since the max condition was explored (maximum number of SPC), and found to result in a significant performance improvement, further engineering exploration is necessary to understand the performance impact of DR on a SPC basis.

First priority of this investigation is to understand if DR performance improvements were only evident in the maximum SPC configuration. This investigation runs separate simulations for multiple SPC criteria, ranging from 4 through 8. Additional results for static and the maximum DR case were shown to understand results of this study. Recall, that all switches have 2 dedicated to the pack parallel connections, and the remaining switches were used for series connections with other batteries.

4.3.1 Switches Per Cell Performance Comparison - Practical Case

Table 4.8 shows the simulation results for total energy delivered to the load where the DR cases were shown for each SPC metric, under multiple C-Rate conditions. First note that in nearly all cases, the DR outperforms the static metric. However at the lower SPC values, the static performance supersedes the DR. This is important to note, as this indicates that DR might not always outperform the static case, but by implementing more switches into the system, the performance enhancement for DR compared to static can be achieved. Understanding the performance impact based on the SPC metric is critical to optimizing the system not only for performance, but also the initial capitol cost for the battery pack.

Table 4.8: Simulation results for total energy delivered to the load in kWh under conditions: 4S2P configuration topology, 2% variable SOH and capacity for initial conditions, 30mV balancing tolerance, and various DR configuration options.

Model	Switches Per Cell	5C-Rate	2C-Rate	1C-Rate
Static	-	76.27	122.40	182.66
Dynamic	4	78.53	122.00	175.55
	5	78.55	127.01	188.86
	6	78.53	126.61	185.09
	7	78.61	126.55	184.91
	8	78.61	126.55	184.91
	Max	78.61	126.55	184.91

The test condition shown in Table 4.8 were based on the condition where a 2% variable SOH and capacity is set for initial conditions. Recall, that in the previous section for this simulation criteria, the performance improvement for DR was not as significant as expected. This seemed to make sense, due to the DR premise of variability in the system resulting in the need for reconfiguration. However, understanding the performance improvement on a per switch basis is important even for this less desired situation.

Figure 4.16 below shows the simulation results for each battery across the numerous simulations run to compare the SPC correlation to performance improvement of DR. First, understanding that DR showed significantly less variability on a cell to cell basis in energy throughput for each of the cells no matter which SPC value was simulated. Additionally, note the very large variation in performance for the static model when examining the energy throughput for cells 1-4 compared to cells 5-8. This can be simply explained for the static model, since the configuration is 4S2P, with cells 1-4 in the first parallel string, and cells 5-8 in the second parallel string. Since these cells are in the same parallel string, cells 1-4 result in similar performance, while cells 5-8 show different throughput (while cells 5-8 have similar performance relative to eachother). By taking this into account, this large separation in throughput between the parallel strings should be alarming, since the system will reach its failure criteria (80% SOH) at an earlier time. When that failure is reached, cells 1-4 are heavily underutilized, which is why examining the various SPC DR cases, it should be quite clear that the overall battery utilization is far superior, as the overall cell throughput across the cells in the system is significantly better aligned.

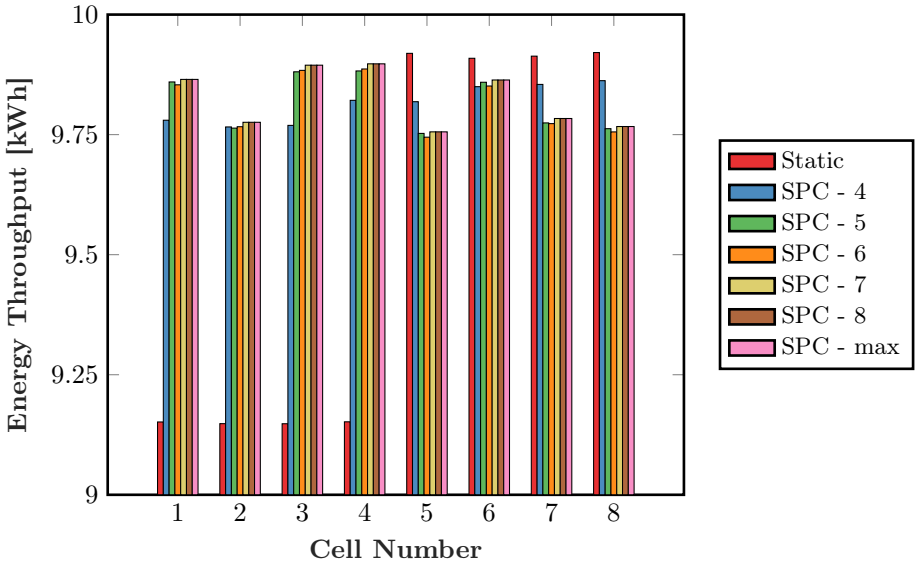

Figure 4.16: Simulation results for total energy of the cells in kWh across the 8 cell system under conditions: 5C-Rate, 4S2P configuration topology, 2% variable SOH and Capacity for initial conditions, 30mV balancing tolerance, and various DR configuration options (SPC variation)

Understanding that there is significant variation in performance for the static case, but not so much for the DR case, a statistical analysis should be done to compare the various SPC metrics. Table 4.9 shows the mean and standard deviation values for all of the simulations done with the main metric of 2% variation in SOH and capacity for initial conditions. Most importantly, note that the average value of energy throughput for the cells is nearly higher for all DR cases compared to static (only 1 simulation was slightly lower performance than static). Additionally, note that the performance enhancement for DR based on specific SPC values seems to saturate the improvement prior to reaching the maximum SPC case. While the performance is still superior to the static case, understanding what values of SPC the improvement saturates is critical to engineering optimization to reduce overall cost in the system (in this case by reducing the number of switches needed).

Not just the average value of cell energy throughput was improved for all DR cases, but the standard deviation is significantly improved compared to the static case. Interesting enough, the standard deviation shows less fluctuation as the SPC value changes, in comparison to the fluctuation in the mean values. However, it is important to note that no matter what SPC value was used, the DR simulations were significantly less variable than the static model. Reducing the cell to cell performance variation can lead to overall better utilization

Table 4.9: Simulation results for total energy of the cells in kWh, with statistics performed (mean and standard deviation) across the 8 cell system under conditions: 4S2P configuration topology, 2% variable SOH and capacity for initial conditions, 30mV balancing tolerance, and various DR configuration options.

Model	Switches Per Cell	5C-Rate		2C-Rate		1C-Rate	
		Mean	St. Dev.	Mean	St. Dev.	Mean	St. Dev.
Static	-	9.533	0.4093	15.300	0.6283	22.832	0.7986
Dynamic	4	9.815	0.0393	15.249	0.4043	21.942	1.0318
	5	9.817	0.0583	15.876	0.1255	23.606	0.4107
	6	9.814	0.0601	15.824	0.1046	23.134	0.4088
	7	9.825	0.0604	15.817	0.1012	23.112	0.3893
	8	9.825	0.0604	15.817	0.1012	23.112	0.3893
	Max	9.825	0.0604	15.817	0.1012	23.112	0.3893

of the batteries, but also improved model accuracy for predicting lifetime and failure criteria across applications.

Table 4.10: Simulation results for final SOH of the cells, with statistics performed (mean and standard deviation) across the 8 cell system under conditions: 4S2P configuration topology, 2% variable SOH and capacity for initial conditions, 30mV balancing tolerance, and various DR configuration options.

Model	Switches Per Cell	5C-Rate		2C-Rate		1C-Rate	
		Mean	St. Dev.	Mean	St. Dev.	Mean	St. Dev.
Static	-	81.99%	1.9126	81.93%	1.7379	82.81%	2.2297
Dynamic	4	81.04%	0.9700	81.84%	1.5574	83.19%	2.4048
	5	81.33%	1.2418	80.92%	1.0885	80.67%	0.5870
	6	81.33%	1.2412	80.95%	1.1051	81.20%	0.9541
	7	81.31%	1.2341	80.95%	1.1144	81.21%	0.9480
	8	81.31%	1.2341	80.95%	1.1144	81.21%	0.9480
	Max	81.31%	1.2341	80.95%	1.1144	81.21%	0.9480

Since the total energy delivered to the load, and the per cell energy throughput was shown to improve as the number of switches increases, understanding the performance improvement for cell utilization is important. Table 4.10 shows the final cell SOH mean and standard deviation values for this simulation. Note that in almost all cases, the average and standard deviation value is improved for DR compared to static. However, the number of switches implemented into a system will ultimately drive the cost of the system up, which means understanding the significance on a per cell basis. Examining the results shown, the performance improvement for conditions 6-8 (SPC) show nearly identical performance. Ultimately, this means that spending the extra capitol on these switches is unnecessary, and the

same end user performance can be achieved using less materials.

4.3.2 Dynamic Reconfiguration Performance Improvement Parameter Effects

Previous sections have shown that DR can show significant performance improvement in contrast with the static case not just for the maximum SPC condition, but across numerous SPC values. Further analysis of the SPC effect on overall DR performance improvement is necessary, but perhaps most important is understanding the effect of specific parameters within applications. Prior sections showed that as the variability of cells is increased, the DR performance thrives, so understanding the effect of the SOH variance in the system is needed (moving from 1 fresh cell to 2 fresh cells, etc.). Additionally, understanding the performance improvement based on the battery pack configuration is critical to understanding the DR topology. For the 8 cell system, this can be done by analyzing the performance difference between the 4S2P and 2S4P configurations. Finally, different applications will have their own balancing specification that will be used throughout cycling. By examining literature, values for balancing specifications ranging from 30mV to 50mV was performed to understand how DR performance is effected by the balancing specification used.

Previous sections showed that DR resulted in performance improvement across the vast majority of the SPC conditions in contrast to the static model, and due to this the results to follow will be compared based on percent improvement for each SPC relative to the static model in order to reduce clutter in figures. Additionally, the deliverable energy to the load could vary based on configuration (significant difference in pack voltage), so by calculating the percent improvement for configuration relative to the static model (at the same configuration) is a way to directly compare the DR performance improvement across different configurations.

Dynamic Reconfiguration Performance Improvement - Effect of SOH Variability

Previous sections showed that DR showed much more performance improvement when more variance is introduced to the system. Specifically, implanting a fresh cell (or multiple fresh cells) amongst already aged cells proved the demand for DR to improve system performance. Figure 4.17 shows the direct comparison for percent performance improvement of DR (relative to the static performance at that same condition) for deliverable energy to the load across multiple C-Rates and SPC values. Notice, that in all cases, the DR simulations outperforms the static model but most importantly as the number of switches increases, the performance does as well. However, as the number of SPC increases, the performance improvement saturates, which proves that there is a fundamental limit where the integration of additional switches is deemed unnecessary from both a technological, and most importantly a financial standpoint.

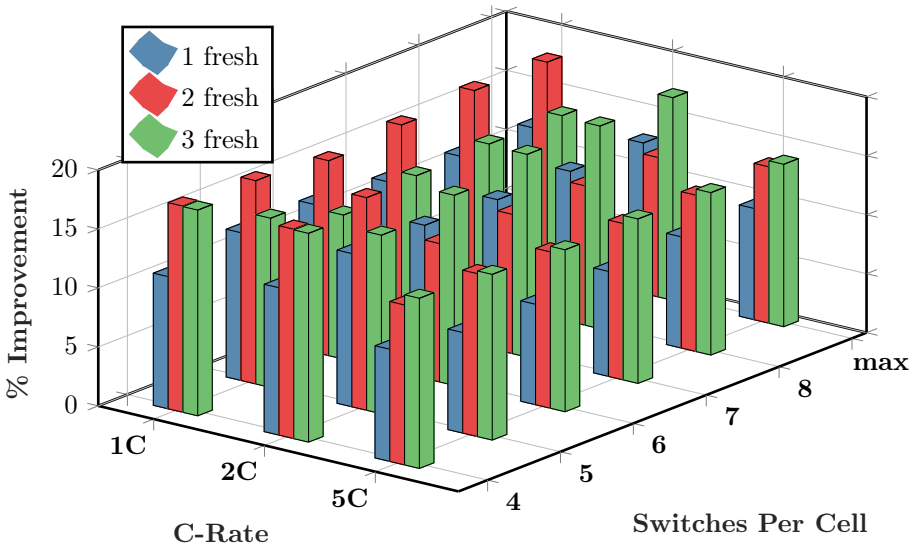

Figure 4.17: Simulation results for total energy delivered to the load in kWh across the 8 cell system under conditions: 2S4P configuration topology, 2% variable Capacity for initial conditions, 30mV balancing tolerance, and various DR configuration options (SPC variation)

While Figure 4.17 certainly contains a lot of information to understand, several conclusions can be made based on these results. First, in all cases (both C-Rate and SPC) the DR topology improves performance in comparison with the static configuration. Additionally, in some cases, the performance increased by 15%, which is a quite significant improvement. Lastly, the relationship for performance improvement for each case (C-Rate and SPC) does

not show consistent performance improvement when moving from 1-3 fresh cells placed in the system. This is a significant property to note, as in DES applications where fresh modules are continuously placed amongst aged, the performance improvement that is seen with DR cannot be linearly increasing with every new fresh module. However, understanding performance improvements through experimental and simulation research, this performance improvement could be understood on a per application basis for commercial suppliers like Johnson Controls.

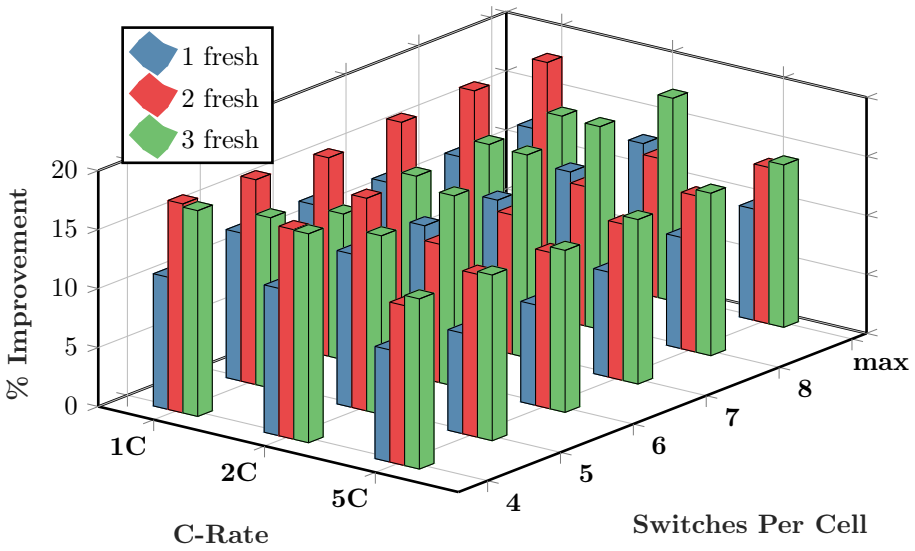

Figure 4.18: Simulation results of mean cell energy throughput in kWh across the 8 cell system under conditions: 2S4P configuration topology, 2% variable Capacity for initial conditions, 30mV balancing tolerance, and various DR configuration options (SPC variation)

Since the deliverable energy showed such promising results (cases with 15% improvement) for DES application conditions with fresh cells integrated with aged cells, further analysis to understand DR improvements was performed. Figure 4.18 shows the analysis for the mean value of cell energy throughput for each of the cases (C-Rate and SPC) represented by the mean value across the 8 cells, and additionally as the percent improvement seen by DR relative to the static model. With performance improvements ranging from 8-18% across all of these cases, it should be noted that by improving the mean value of cell energy across the system essentially translates to better utilization of system components. The average cell energy being increased signifies that by utilizing DR topologies (across different SPC values), the energy delivered to the load is being better distributed across the cells in the system, rather than the bulk of the load being applied to specific string of cells.

Table 4.11: Standard deviation values across multiple C-Rates and SPC for the cell energy throughput comparison across 1-3 fresh cells in the 8 cell system.

Model	SPC	5C-Rate			2C-Rate			1C-Rate		
		1 Fresh	2 Fresh	3 Fresh	1 Fresh	2 Fresh	3 Fresh	1 Fresh	2 Fresh	3 Fresh
Static	-	0.1341	0.1368	0.1344	0.2009	0.2047	0.2019	0.2529	0.2645	0.2554
Dynamic	4	0.0679	0.1831	0.1885	0.1003	0.2917	0.2990	0.1332	0.4096	0.4301
	5	0.0821	0.1729	0.1267	0.1197	0.2797	0.1554	0.1632	0.3958	0.2248
	6	0.0822	0.1642	0.1576	0.1194	0.1202	0.2086	0.1632	0.3298	0.1847
	7	0.0541	0.1642	0.1451	0.0846	0.1224	0.2230	0.1208	0.3626	0.1748
	8	0.0543	0.1642	0.1394	0.0847	0.1227	0.2217	0.1199	0.3683	0.1892
	max	0.0543	0.1642	0.1394	0.0847	0.1227	0.2217	0.1198	0.3683	0.1892

After analyzing the average cell energy throughput figure, the effect of fresh cells being placed amongst aged cells showed significant improvement, however no clear relationship was found when moving from 1-3 fresh cells. Further analysis was conducted to understand if any potential relationship can be found by comparing the standard deviation across the 8 cells in the system for each of the initial SOH conditions previously discussed. Table 4.11 shows the standard deviation values for each of the 1-3 fresh cell conditions simulated.

While examining the final results across all of these simulations has provided a strong case for DR topologies in the DES cases (where significant cell to cell variability can be found), further understanding and analysis was performed to understand how the performance varies throughout the simulation. Figure 4.19 shows the energy delivered to the load per cycle, for the 1C-Rate condition with each SPC value for the dynamic simulations in addition to the static case. Note that this figure contains 3 plots, where (a) is the DES condition of 1 fresh cell, (b) 2 fresh cells, and (c) with 3 fresh cells, and the remaining cells in the system are set to aged (85% SOH) as the initial condition. Note that in all 3 of the DES conditions shown in the plot, the DR topologies (SPC from 4-max) show more energy delivered to the load per cycle in comparison to the static model. Interesting enough, when examining the DR cases of varying the SPC, the energy per cycle delivered to the load doesn't change significantly when integrating additional switches into the system (e.g., increasing the SPC). This is important to understand, as by increasing the SPC value, the cost of the system will increase, so the additional capitol investment in both switches, but increased controller complexity needs to be returned with a boost in performance enhancement.

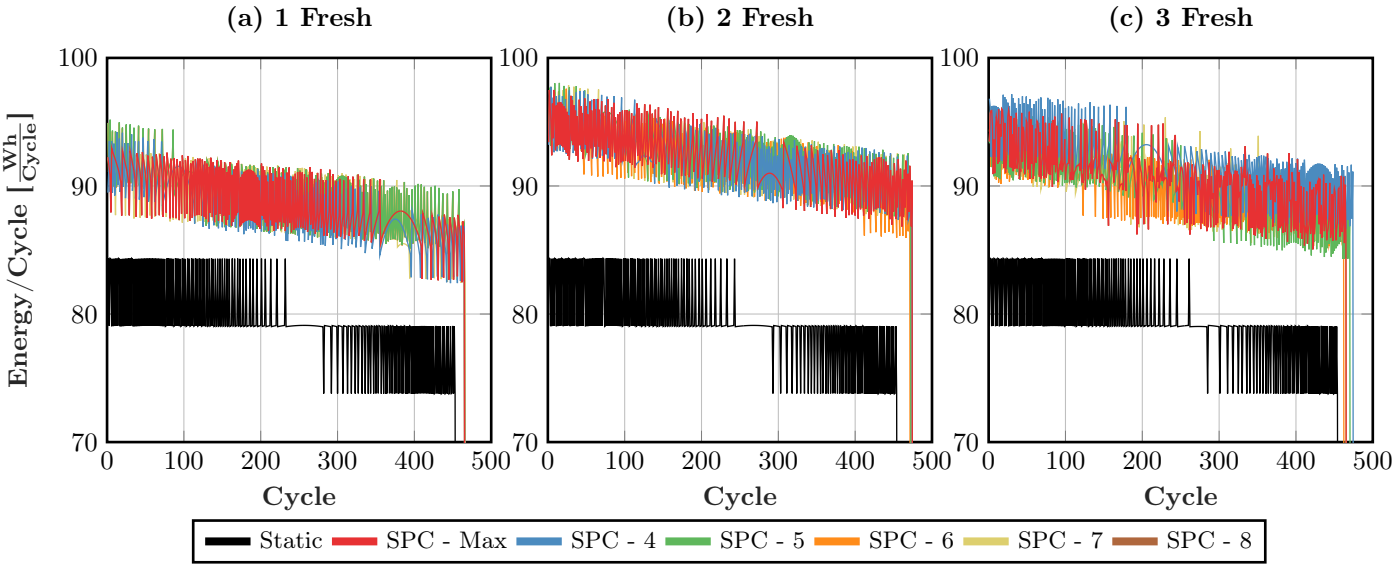

Figure 4.19: Comparison of static vs dynamic models under the multiple SPC conditions (labeled in the legend) for 1C-Rate current. The initial SOH conditions for (a) is 1 fresh cell, (b) 2 fresh cells, and (c) 3 fresh cells, where the remaining cells in the system (total of 8 cells) are initially at 85% SOH. The data shows the total energy delivered to the load for each cycle.

Since the delivered energy to the load per cycle showed interesting results for the three DES cases, further understanding to the performance variation across the 8 cells in the system throughout these simulations was performed. Figure 4.20 corresponds to the standard deviation (or variance) across the 8 cells in the system for (a) 1 fresh cell, (b) 2 fresh cells, and (c) 3 fresh cells cases. Note that in the delivered energy per cycle figure previously discussed, the differentiation between each of the values of SPC showed unclear indication as to the performance difference when changing levels of SPC. However, the cell to cell variation in energy per cycle now shows clear evidence to the performance difference for the cells as a function of the SPC. In the case of this figure, the DR simulations goal is to have the lowest variation across the cells in the system, ultimately indicating overall better battery utilization, in comparison to the static model. Note, that for some values of SPC, the variance in the system increases above the level of the static condition, which proves the need t examine the results throughout the simulation, rather than solely the final value.

As the number of fresh cells (or modules) increases in the system, this research showed that not only does the DR topologies provide significant performance improvement, but the specific SPC value can significantly impact the deliverable energy, as well as the overall battery utilization in the system. Within this condition, the variability in the system can

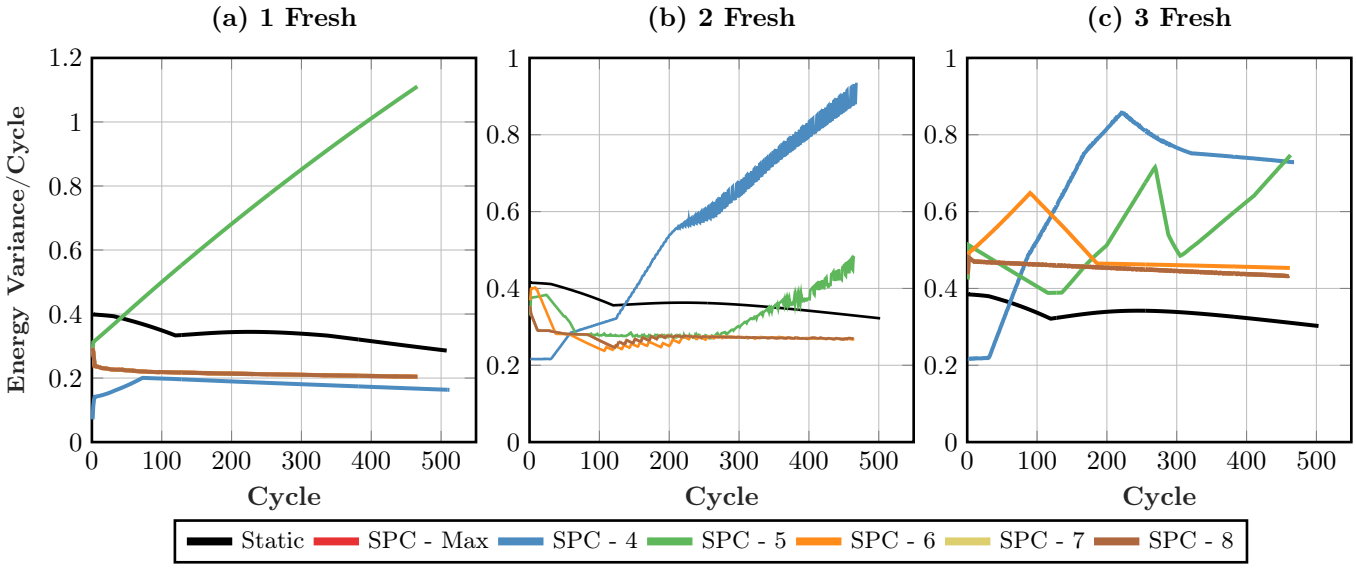

Figure 4.20: Comparison of static vs dynamic models under the multiple SPC conditions (labeled in the legend) for 1C-Rate current. The initial SOH conditions for (a) is 1 fresh cell, (b) 2 fresh cells, and (c) 3 fresh cells, where the remaining cells in the system (total of 8 cells) are initially at 85% SOH. The data shows the standard deviation across the 8 cells in the system for energy throughput per cycle (Wh/cycle) throughout the simulations.

be quite significant, which applies well with the DR topology. In DES applications where modules get replaced frequently, applying the DR topology can result in significant performance improvements (shown to be around 8-15% improvement) in contrast to traditional static topologies.

Dynamic Reconfiguration Performance Improvement - Effect of Configuration Variability

After analyzing the SOH effect on DR performance improvement, the large variation in cell to cell aspects showed quite significant effect on system improvement when implementing DR. The next parameter to investigate is the effect of the configuration. For the 8 cell system, there are two configuration options: 4S2P, and 2S4P. The important distinction between these two configurations is the number of parallel strings in each. Referring back to Table 4.1, the number of configurations at each value of SPC varies quite significantly. When increasing the number of parallel strings (2S4P configuration), the DR controller has significantly more opportunities to reconfigure and ultimately limit the performance demand from the weaker (lower SOH/SOC) cells in the system, while the stronger (higher SOH/SOC) cells in the system can take the bulk of the load.

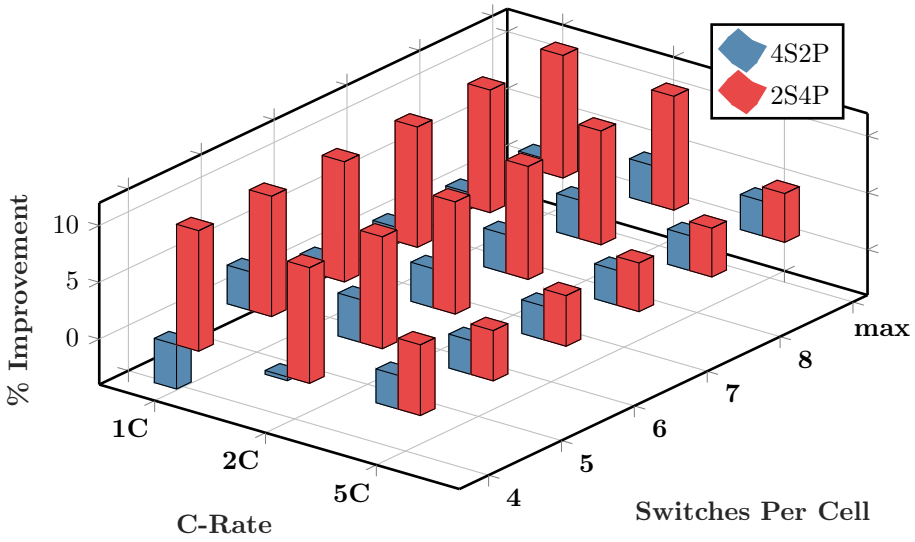

Figure 4.21: Simulation results for total energy delivered to the load in kWh across the 8 cell system under conditions: 2% variable Capacity and SOH for initial conditions, 30mV balancing tolerance, and various DR configuration options (SPC variation)

Analyzing the results from simulations corresponding the the practical case (2% variable SOH and Capacity), Figure 4.21 shows the total energy delivered to the load across multiple C-Rates and SPC values. Initial conclusions from this figure should note that when increasing the number of parallel strings (difference between 4S2P and 2S4P), the percent improvement that DR provides increases substantially. As this is a more practical case, understanding how the selected configuration plays a role in deliverable energy improvement. Since this is a practical case, by selecting systems with 4 parallel strings, the resulting performance improvement ranges around 8-10% in deliverable energy. For applications such as automotive, a 10% increase in deliverable energy (e.g. range) is highly desirable. However, what makes this ultimately more appealing is by applying DR topologies to existing systems, the volume needed for the battery system likely will not change, so any performance improvement in applications with limiting volume is in high demand.

The deliverable energy showed a significant increase in percent improvement when shifting from 2 parallel strings to 4. Further understanding of this configuration effect on performance was performed to understand the cell energy throughput. Figure 4.22 shows the mean value (across the 8 cell system) for cell energy throughput corresponding to each of the specific C-Rate and SPC simulations performed. Examining the figure, an interesting aspect shows that the performance difference relative to the configuration increases as the

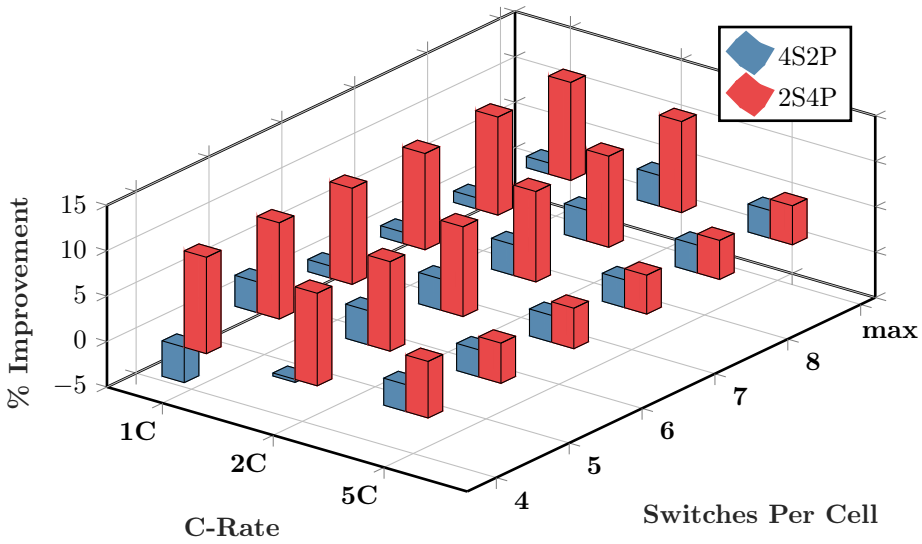

Figure 4.22: Simulation results of mean cell energy throughput in kWh across the 8 cell system under conditions: 2% variable Capacity and SOH for initial conditions, 30mV balancing tolerance, and various DR configuration options (SPC variation)

C-Rate is lowered. Essentially, the lower the C-Rate, the better the performance improvement should be expected when increasing the parallel strings in the configuration. While this simple relationship was found for an 8 cell system, typical systems in commercial applications employ battery packs with much larger cell counts. Due to this, the relationship as the number of parallel strings extends beyond 4 is needed. After making these conclusions both for delivered energy, and cell energy, further examination into the configuration impact on performance needs to be focused on the cell to cell variation in performance.

Table 4.12: Standard deviation values across multiple C-Rates and SPC for the cell energy throughput comparison across 4S2P and 2S4P configurations in the 8 cell system.

Model	**SPC**	**5C-Rate**		**2C-Rate**		**1C-Rate**	
		4S2P	**2S4P**	**4S2P**	**2S4P**	**4S2P**	**2S4P**
Static	-	0.4093	0.5784	0.6283	0.8862	0.7986	1.1985
Dynamic	4	0.0393	0.2128	0.4043	0.2974	1.0318	0.4350
	5	0.0583	0.1741	0.1255	0.2682	0.4107	0.4132
	6	0.0601	0.1726	0.1044	0.2627	0.4088	0.4196
	7	0.0604	0.1795	0.1012	0.2605	0.3893	0.4176
	8	0.0604	0.1799	0.1012	0.2605	0.3893	0.4279
	max	0.0604	0.1799	0.1012	0.2605	0.3893	0.4285

In order to examine the relationship for cell to cell variation with respect to the variation in configurations, Table 4.12 is presented to deduce conclusions. Examining this table, it can be concluded that the DR topologies result in overall lower standard deviations, or variation,

in cell to cell performance regardless of configuration. However, it seems as though the standard deviation increases when moving to configurations with more parallel strings. This could be perceived as a potential drawback, but it should be noted that the standard deviation for the DR cases is still improved in comparison with the static case. Even though the variation in cell to cell performance increases with more parallel strings, the performance enhancements in both cell energy throughput, as well as total energy delivered to the load certainly supersedes any potential drawback from a slight increase in standard deviation.

Examining the performance differences during the simulations was performed in order to better understand any performance variations between static and DR topologies solely based on the different configurations. While it has already been shown that the increased number of parallel strings results in more performance enhancement in terms of final values, understanding how the performance varies during the simulation for various numbers of parallel strings was done. Figure 4.23 shows the 1C-Rate simulations for the DES case of 1 fresh cell with the rest aged, since this condition showed significant variability in the system to allow the full potential of DR to enhance performance. (a) in the figure represents the 4S2P configuration (2 parallel strings), and (b) represents the 2S4P configuration (4 parallel strings). By examining the results for this DES case, we see the most performance improvement potential through DR since there is a large variance across the cells in the system, where the controller begins finding optimum configurations immediately when the simulation starts, unlike the figures shown previously for the ideal and practical case (see Figure 4.15). Since the simulation was based on an 8 cell system, there are only two configuration options that are reconfigurable (8S1P and 1S8P would only have one potential configuration that is unique), so examining the differences when doubling the number of parallel strings is the only option thus far. Examining this figure, the deliverable energy per cycle instantly shows superior performance for the DR case in comparison to the static case. However, the effect of the number of parallel strings results in the various levels of SPC to largely effect the performance improvement in terms of energy per cycle when comparing against SPC ranging from 4 to maximum. Since the 4S2P (plot (a) in the figure) shows more of a performance separation when changing the value of SPC, it is intuitive to assume that

when increasing the number of parallel strings in the system, the resulting need for higher values of SPC diminishes. To illustrate this, refer back to Table 4.1 where we can see the total number of configuration options as a function of parallel strings and SPC values. As we increase the SPC, under 4 parallel strings (2S4P in this case), the total number of configurations is already extremely high, that it is difficult to find a new configuration that delivers more that a lower value of SPC might not have access to.

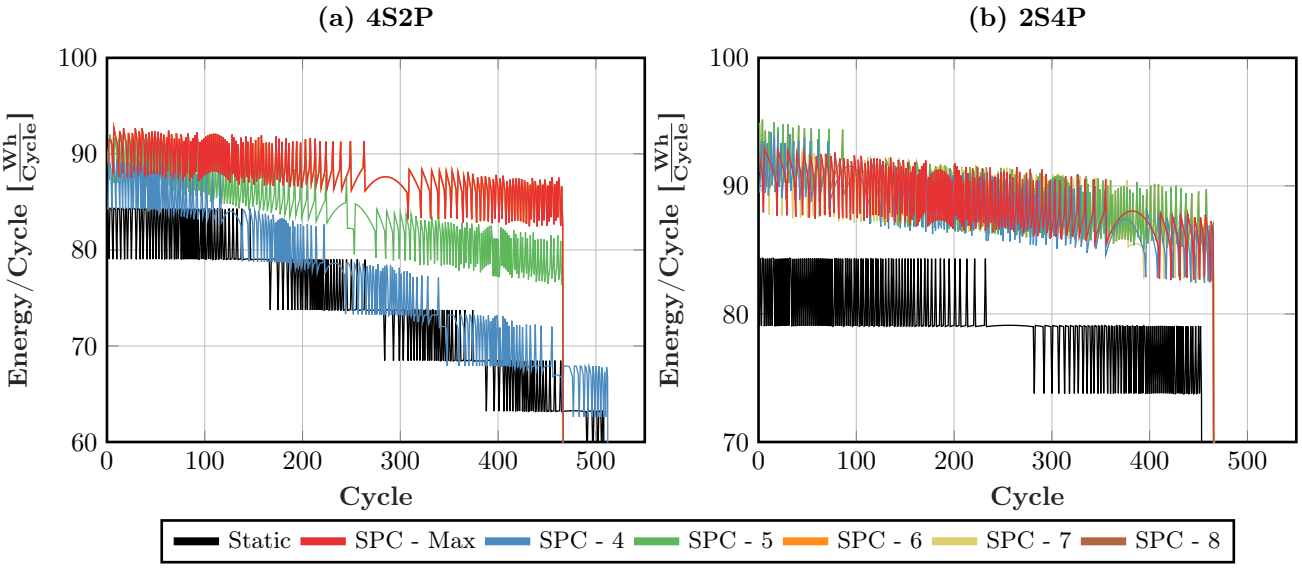

Figure 4.23: Comparison of static vs dynamic models under the multiple SPC conditions (labeled in the legend) for 1C-Rate current. The configurations are: (a) 4S2P (b) 2S4P, and both were tested under the initial condition of 1 fresh cell with the rest aged (DES case). The data shows the total energy delivered to the load for each cycle.

In order to further understand the implication of SPC relative to the number of parallel strings, Figure 4.24 was used to illustrate the configuration selection for the 1C-Rate test condition across (a) the 4S2P configuration, and (b) the 2S4P configuration. Note that the 2S4P case had over 2,000 more reconfiguration events during the lifetime of the system, which ultimately resulted in the far superior performance discussed previously in the section. From Table 4.1, the 2S4P configuration had 105 potential configuration options, while the 4S2P configuration had only 35. This nearly 3x increase in configuration options lead to 2,000 more reconfiguration events, and ultimately a larger percent improvement for the 2S4P configuration in contrast to the 4S2P configuration. However, an interesting observation was that both configurations did not use every configuration option available, and seemed to gravitate towards a few throughout the entire lifetime. In a commercial setting, the engineer

could identify these key configurations, and solely select these for the controller to evaluate in order to greatly reduce the computation needed to determine the optimum configuration, especially in scenarios where the potential configurations get larger than 1,000 (e.g., battery systems with more than 8 cells).

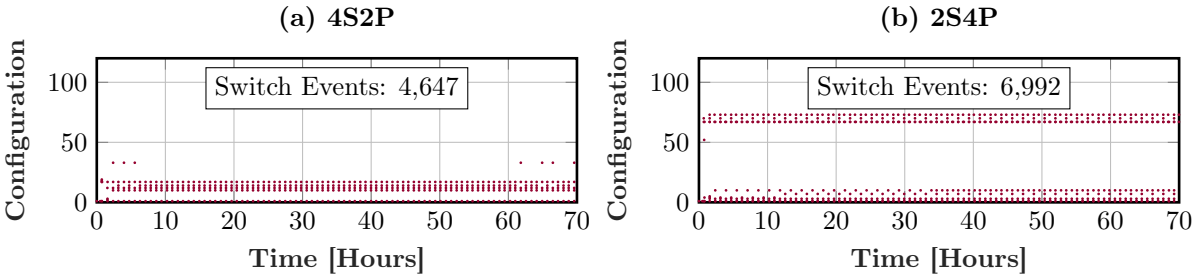

Figure 4.24: Comparison of the configuration choice by the reconfiguration controller for the max SPC condition for the 1C-Rate condition where (a) corresponds to the 4S2P configuration, and (b) corresponds to the 2S4P configuration.

Further understanding of the performance difference as a function of SPC and configuration choice was performed by understanding how the variance in cell energy per cycle behaves. Figure 4.24 shows the 1 fresh cell (e.g., DES condition), 1C-Rate condition with the SPC values varying from 4 to maximum, where (a) corresponds to the 4S2P configuration, and (b) corresponds to the 2S4P configuration. Note that again, the 2S4P shows little separation in performance as a function of SPC, even though the performance far supersedes the static condition. However, the 4S2P does show the impact of SPC selection relative to the cell energy throughput to expect in the system, which results in the conclusion that by increasing the parallel strings, the configuration options is increased significantly enough to allow lower levels of SPC to achieve the same performance enhancement.

The results in this section provided a strong case to understand how the configuration selection for an application will impact the resulting performance enhancement when integrating DR topologies. As the number of parallel strings increases, the total number of configuration options increases as well, which seemed to become redundant as the performance enhancement for varying SPC values did not seem to change significantly. Application specific studies would need to be conducted in order to determine the optimized SPC value to use in order to retain the performance enhancement of DR, while minimizing the cost to implement the system. While an 8 cell system would not have a large quantity of switches

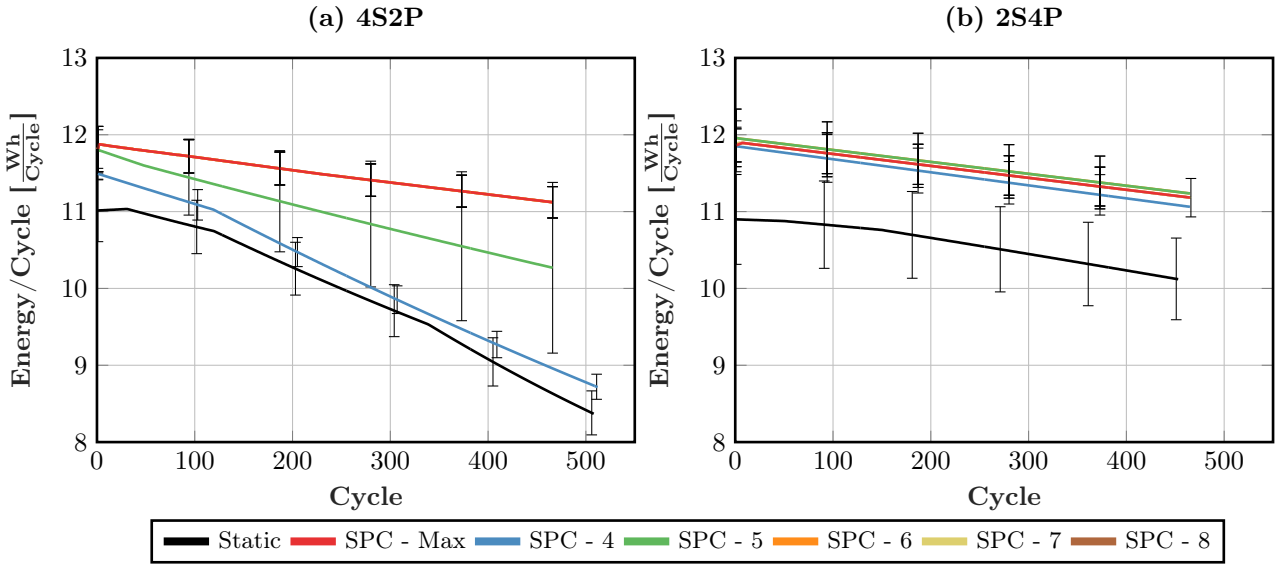

Figure 4.25: Comparison of static vs dynamic models under the multiple SPC conditions (labeled in the legend) for 1C-Rate current. The configurations are: (a) 4S2P (b) 2S4P, and both were tested under the initial condition of 1 fresh cell with the rest aged (DES case). The data shows the average energy throughput across the 8 cell system (with error bars indicating the standard deviation) per cycle (Wh/cycle) throughout the simulations.

to try to optimize for minimizing switches (and cost), when moving to larger sized systems (e.g., EV's with battery systems containing thousands of batteries), the reduction of SPC just by one level could result in significant cost savings.

Dynamic Reconfiguration Performance Improvement - Effect of Balancing Specification Variability

The final parameter of interest to investigate was the effect of the balancing specification on any performance enhancements when utilizing DR. Searching through literature and commercial products, typical balancing specifications were found to range from 30mV to 50mV. By investigating this range of balancing specifications, it is important to understand if changing the balancing specification can result in any impact on the DR performance enhancement.

To examine any performance impact due to the balancing specification, the practical case was studied for the balancing specification conditions: 30mV, 40mV, and 50mV. Recall, that the practical case consists of the initial condition for SOH and capacity being equal to 2%. Figure 4.26 shows the results for the total energy delivered to the load for the practical case, while the data corresponds to each balancing specification simulated.

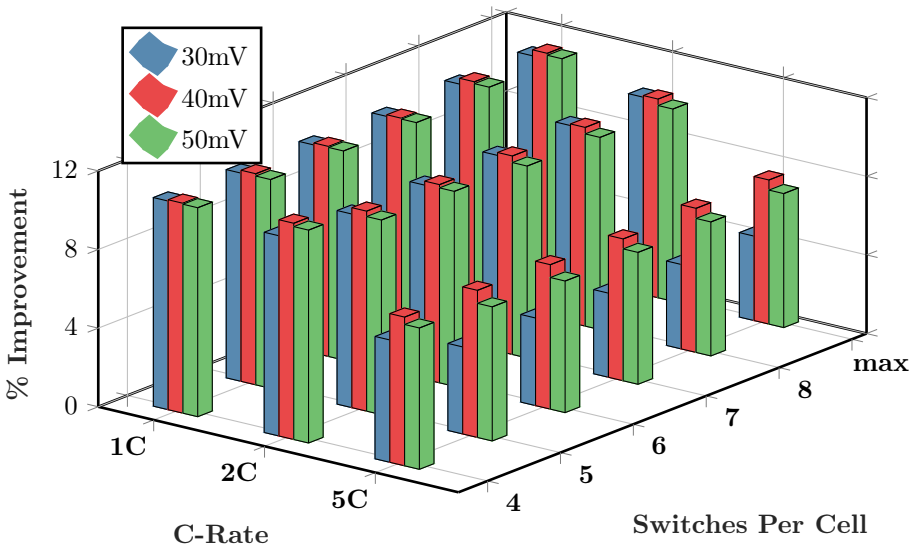

Figure 4.26: Simulation results for total energy delivered to the load in kWh across the 8 cell system under conditions: 2% variable Capacity and SOH for initial conditions, 2S4P Configuration, and various DR configuration options (SPC variation)

Several key conclusions can be made by studying the results shown in Figure 4.26. First, by studying each individual case (e.g. 5C-Rate and SPC-4) the performance impact relative to each balancing specification seems to be rather minimal. While the average value across each case differs when comparing the deliverable energy for one C-Rate to another, or one SPC to another, the local values for the range of balancing specifications from 30mV to 50mV changes minimally. This is important, since this indicates that the balancing specification seems to have only a slight impact on any performance enhancements found within DR topologies. Additionally, the balancing specification seems to have more significant of an impact as the C-Rate through the system increases. This seems rather intuitive, since as the C-Rate gets higher, the variance in the batteries will be separated more within each cycle. By having more separation in the cycle, some batteries hit the voltage limits sooner, which could result in more balancing needed for that specific C-Rate. Due to this, it is reasonable to state that as the system's C-Rate increases, the impact on the balancing specification becomes more critical, at least in terms of deliverable energy to the load.

The deliverable energy to the load showed promising results relative to the impact on balancing specifications discussed previously. Further verification of the balancing specification impact is presented in Figure 4.27 as the average value of cell energy throughput. The profile of this figure seems similar to Figure 4.26 when comparing the performance

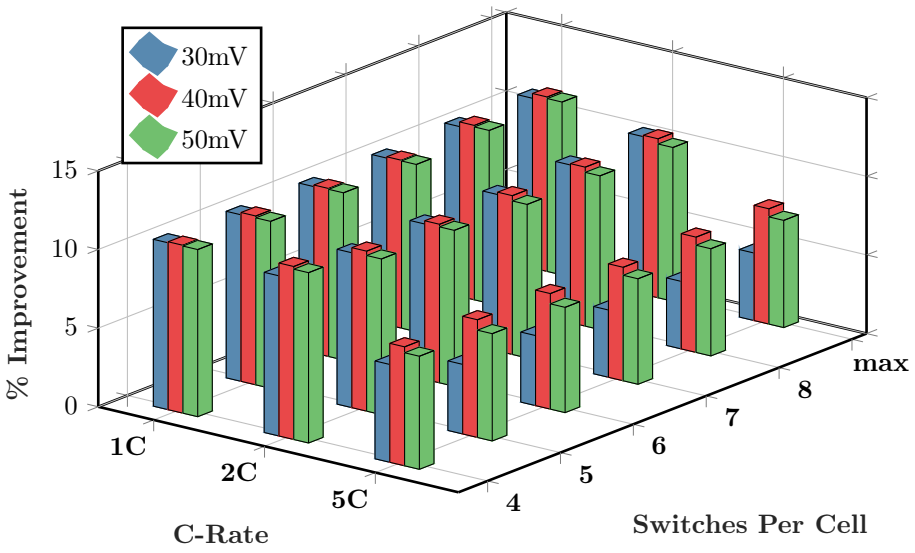

Figure 4.27: Simulation results of mean cell energy throughput in kWh across the 8 cell system under conditions: 2% variable Capacity and SOH for initial conditions, 2S4P Configuration, and various DR configuration options (SPC variation)

profile across the C-Rates and SPC values. Cell energy, similar to deliverable energy, shows the same traits when comparing the performance impact based on balancing specifications. Further examination into the simulation results was performed to understand the energy per cycle metric previously used.

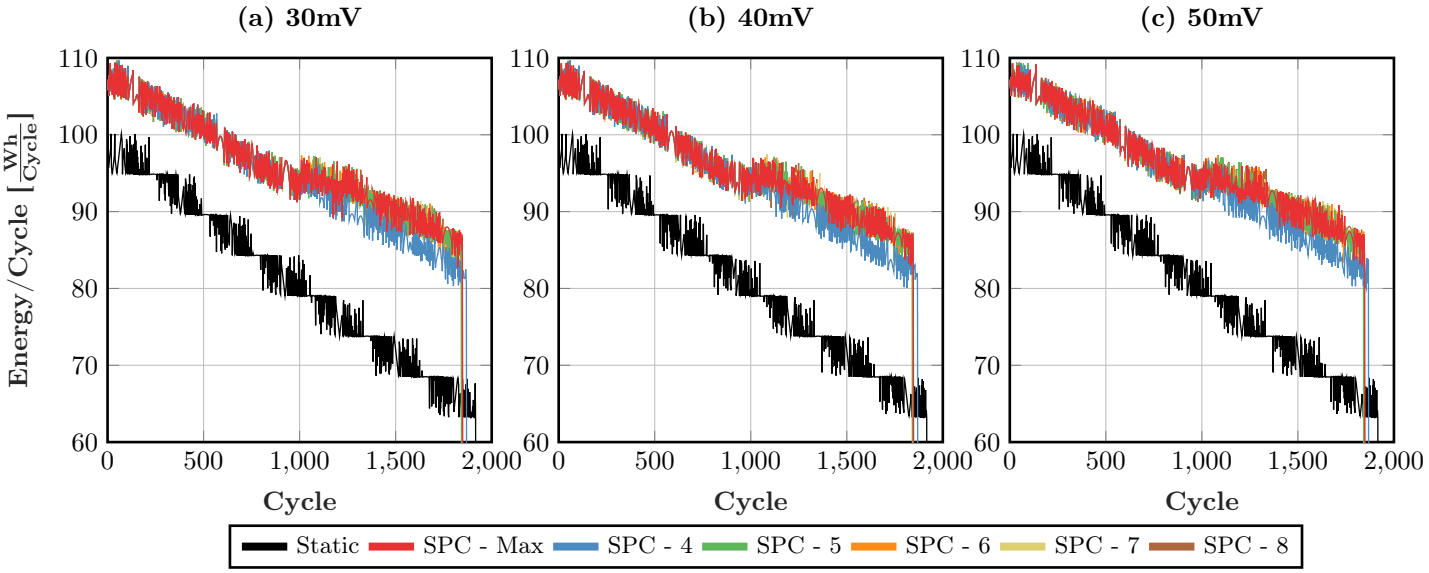

Figure 4.28: Comparison of static vs dynamic models under the multiple SPC conditions (labeled in the legend) for 1C-Rate current, and 2S4P configuration. The balancing specifications are: (a) 30mV (b) 40mV, and (c) 50mV, and all were tested under the initial condition of 2% variable SOH and Capacity. The data shows the total energy delivered to the load for each cycle.

Understanding the balancing specification impact on performance was shown across all C-Rates and SPC values as a final value for deliverable and cell energy previously, but

understanding how the DR case reacts during the simulation is needed. Figure 4.28 shows the simulation results for deliverable energy per cycle with conditions: 2S4P configuration, 1C-Rate, initial conditions of 2% variable SOH and Capacity (e.g., practical case), and balancing specification of (a) 30mV, (b) 40mV, and (c) 50mV. Note that in this practical case scenario, the system achieved enough variability for the controller to reconfigure about midway through the simulation, which can be seen in (a-c) on the figure. Comparing the different balancing specifications for the deliverable energy per cycle across each of the SPC values, once again it seems as though the balancing specification does not significantly impact performance.

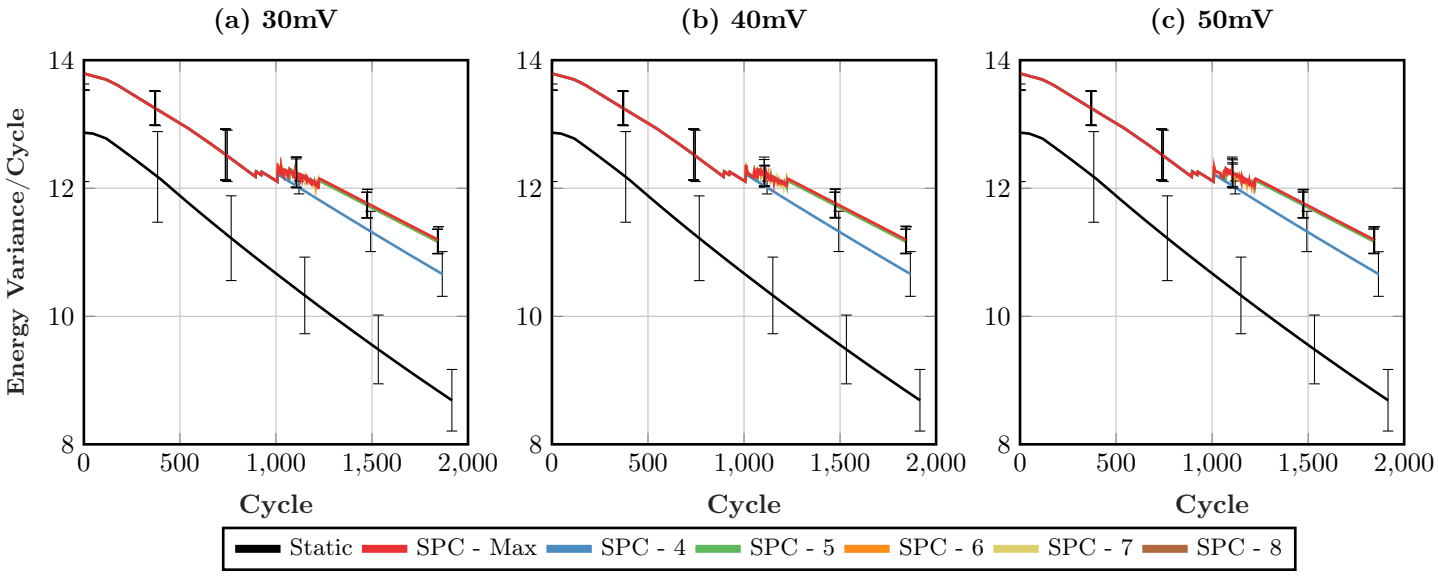

Figure 4.29: Comparison of static vs dynamic models under the multiple SPC conditions (labeled in the legend) for 1C-Rate current, and 2S4P configuration. The balancing specifications are: (a) 30mV (b) 40mV, and (c) 50mV, and all were tested under the initial condition of 2% variable SOH and Capacity. The data shows the average cell energy for each cycle (with error bars indicating standard deviation across the 8 cells in the system).

The deliverable energy showed little, to no effect from the balancing specification, so further analysis was performed to understand the average cell energy per cycle as well. Figure 4.29 shows the simulation results for average cell energy per cycle (with error bars indicating standard deviation across the 8 cells in the system) with conditions: 2S4P configuration, 1C-Rate, initial conditions of 2% variable SOH and Capacity (e.g., practical case), and balancing specification of (a) 30mV, (b) 40mV, and (c) 50mV. The cell energy throughput seems to be virtually the same across each of the balancing specifications as observed before. An observation here is that the variance in cell energy throughput is significantly

lower for the DR cases than in the static case, even across each of the different balancing specifications. Regardless, both the deliverable energy, and the cell energy throughput show that the balancing specification does not significantly impact performance.

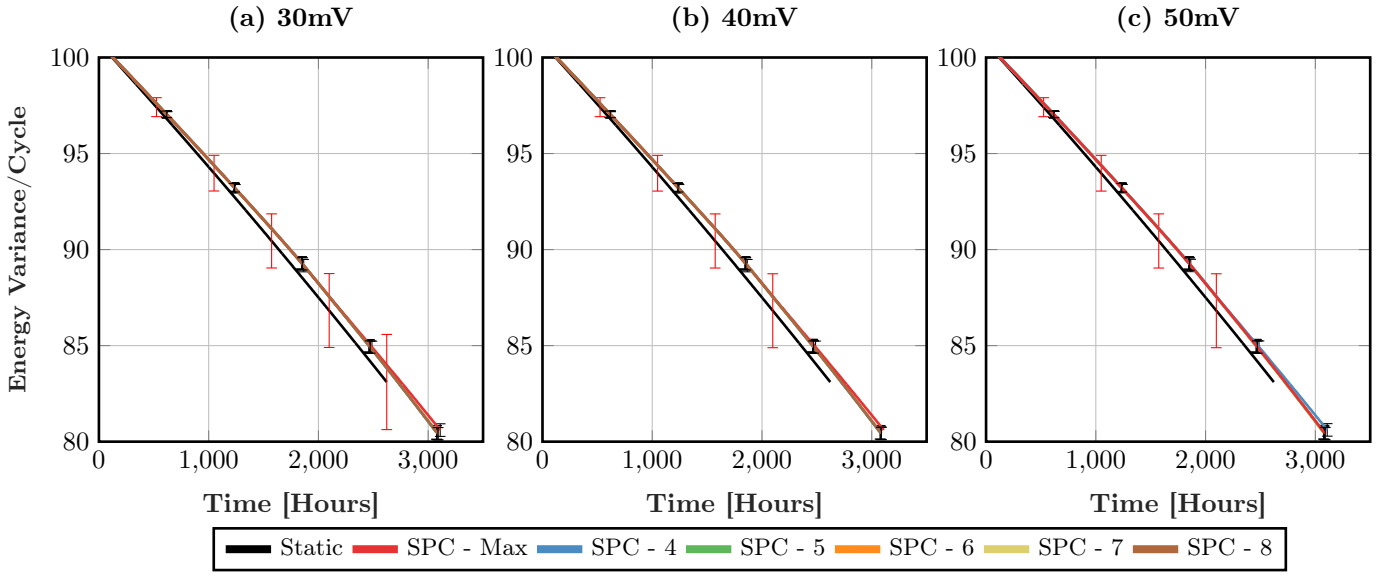

Figure 4.30: Comparison of static vs dynamic models under the multiple SPC conditions (labeled in the legend) for 1C-Rate current, and 2S4P configuration. The balancing specifications are: (a) 30mV (b) 40mV, and (c) 50mV, and all were tested under the initial condition of 2% variable SOH and Capacity. The data shows the average cell SOH across the 8 cell system (with error bars indicating the standard deviation).

The last aspect to study for the balancing specification effect was the average cell SOH throughout the simulation. Figure 4.30 shows the simulation results for average cell SOH (with error bars indicating standard deviation across the 8 cells in the system, red bars for the static model) with conditions: 2S4P configuration, 1C-Rate, initial conditions of 2% variable SOH and Capacity (e.g., practical case), and balancing specification of (a) 30mV, (b) 40mV, and (c) 50mV. The variation across each of the balancing specifications certainly was not evident when analyzing the cell SOH. Although, notice that again the DR shows significantly lower standard deviation across the 8 cells in the system in comparison to the static model. By having a smaller variance, this means that overall the batteries were better utilized, by maximizing the energy available and using the cells with higher SOH to degrade those cells faster than the cells with lower SOH. In an ideal scenario, all cells in the system would reach the 80% failure criteria together, meaning that every bit of energy was utilized before the pack is shut down. However, by showing SOH values in the figure greater than 80%, this means that batteries were not fully utilized. Due to this, it is clear that the DR

cases (across all SPC's) have better battery utilization, but examining across each of the balancing specifications, the value for the balancing specification choice seems to be negligible. Since the balancing specification seems to have minimal impact on performance for both the cell energy throughput, cell SOH, and deliverable energy, it is reasonable to conclude the balancing specification can be deemed as negligible to the performance enhancements found in DR topologies.

4.4 Chapter Summary

This chapter introduced and analyzed the potential for DR topologies performance impact on pack level battery systems. Since this technology was relatively immature in literature, there were significant areas of interest that demanded answers to understand potential application of DR topologies. Since previous studies have focused on single cycle DR application performance enhancement, or more specific scenarios such as fault tolerance, the focal point of this research was designed around lifetime modeling and simulation of DR. Conducting simulations was the important decision in order to reduce experimental testing time, financial resources needed, but also provide the potential to study a vast range of DR application scenarios in a reasonable time. Further studies could be conducted in a real-world experimental testing to validate any findings from the simulations.

The first question raised about application of DR in contrast to the static condition is validating that the lifetime performance of the battery system will improve when applying the DR topology to the same battery system. Throughout the simulations and data presented in this chapter, the DR case was shown to significantly improve system performance, while some application specific scenarios were found to have a higher performance improvement than others. Table 4.13 shows the percent improvement for the DR case against the static case with results for the multiple SOH initial conditions studied in this chapter. Note that in all conditions, the DR topology showed improvement, deeming the implementation of this technology necessary for total system performance enhancement.

Table 4.13: Summary of % improvement for DR case (maximum SPC condition) in comparison with the static case results for total energy delivered to the load across multiple C-Rate conditions (for the 2S4P configuration)

SOH Condition	5C-Rate	2C-Rate	1C-Rate
2% Variable	4.29%	10.02%	10.79%
1 Fresh Cell	9.43%	12.75%	11.81%
2 Fresh Cell	13.25%	11.81%	17.66%
3 Fresh Cell	13.77%	17.18%	13.43%
4 Fresh Cell	17.32%	20.05%	20.65%
5 Fresh Cell	20.13%	21.06%	20.36%

Now that understanding DR shows performance improvement, the results in this chapter next focused on the understanding of how the SPC metric correlates to the system performance enhancement. While these results were thoroughly discussed throughout the chapter, a summary of the percent improvement for the DR topology is shown in Table 4.14. This table does an excellent job to allow easy comparison of different SPC values across the four main SOH conditions discussed. Note that with the exception of two cases, the DR outperforms the static case in delivering energy to the load. However, understanding how the performance increases as the variance in initial conditions alters is significant to analyzing DR performance enhancement. The percent difference going from 1 fresh cell to 2, and ultimately 3 fresh cells SOH conditions continuously increases to show the significance of DR technology and improving the overall deliverable energy to the load.

The final goal of Table 4.14 is to be able to conclude that the SPC value certainly matters both from a performance enhancement standpoint, but most importantly a cost to consumer standpoint. As the number of switches increases, the overall cost of the system increases as well, so in order to justify the added expense, the performance enhancement has to increase alongside the switches. However, from examining the table, it is clear to conclude that implementing all of the switches into the system is not necessary as the performance enhancement saturates mainly around 5 SPC values.

This chapter also examined the specific effect of parameters on any performance enhancement found in DR. First, the effect of the SOH was discussed for the specific DES

Table 4.14: Summary of % improvement for DR case in comparison with the static case results for total energy delivered to the load across multiple C-Rate conditions, showing the simulation results for varying the SPC value

SOH Condition	Switches Per Cell	5C-Rate	2C-Rate	1C-Rate
2% Variable	4	2.97	-0.33	-3.89
	5	2.98	3.77	3.39
	6	2.96	3.43	1.33
	7	3.07	3.39	1.23
	8	3.07	3.39	1.23
	max	3.07	3.39	1.23
1 Fresh Cell	4	5.10	4.65	3.28
	5	7.16	7.48	3.89
	6	5.48	7.52	6.31
	7	5.48	7.52	6.31
	8	5.48	7.52	6.31
	max	5.48	7.52	6.31
2 Fresh Cell	4	4.55	8.17	5.17
	5	7.13	8.03	6.09
	6	6.56	8.08	7.41
	7	6.14	8.10	7.14
	8	6.14	8.10	7.14
	max	6.14	8.10	7.14
3 Fresh Cell	4	3.99	7.55	4.63
	5	8.34	7.98	8.11
	6	8.60	8.86	8.05
	7	8.56	9.12	8.02
	8	8.56	9.12	8.02
	max	8.56	9.12	8.02

application where fresh modules were placed with aged modules, as done in industry. Additionally, the effect of the configuration was discussed and shown that as the number of parallel strings increased in the system, the percent improvement when utilizing DR significantly increased. Finally, the balancing specification impact on performance was studied to understand how strict, or lenient, the balancing specification will effect any performance enhancements found within DR applications.

With all of these conclusions being made, an observation can be made at the highest level of speculation for potential advantages of DR being implemented in industry. From speaking to our sponsor (Johnson Controls), "bin" sorting that is done at manufacturing plants can be very expensive, both in time, but also space needed within the manufacturing

plant. Recall, that "bin" sorting is essentially performing capacity checks on the batteries as they are made, and grouping them in bins to get them all within an allowable tolerance range to put together in a pack. It is intuitive to think that this could take a lot of physical space in a plant, but also a significant time expense. The results of the DR research shown indicated that the DR truly thrives when finding variation in the system. While this variation will ideally be after the system is integrated into an application, it provides the idea that the bin sorting being performed can be overcame with DR. Although, maybe bin sorting is still necessary, and should not be completely removed if implementing DR, but perhaps it is reasonable to assume the bin sorting tolerance could be lightened to a wider range resulting in less time, and space expenses to the industry.

Chapter 5

Conclusions, Contributions, and Recommended Future Work

5.1 Conclusions

Since the areas of this research vary significantly, the conclusions will be sorted by the specific area, with each item in the list denoted at the beginning the area that the bullet point covers:

- **State of Energy -** The first aspects of this research focused on a single discharge event to directly compare the SOC and SOE models variation. The results showed that these models do in fact show a difference, but most importantly, the peak value of the difference occurs in the middle of the SOC operating range ($\approx$50%). Knowing where this peak value is located is critical, since most applications narrow the SOC operating window, and could result in a small SOC window that oscillates frequently around this peak error range.

- **State of Energy -** Investigating the model differences resulted in a profile that showed the model differences between SOC and SOE, and examining further, the peak value of the model differences was found to be strictly dependent on the C-Rate of the discharge. All C-Rates showed similar profile, however the model differences showed dependent on the C-Rate.

- **State of Energy -** The aging effect of the batteries were studied to understand how the model differences between SOC and SOE are shown as the battery ages. Results showed that the model differences do not remain constant, but do in fact change as a function of battery SOH. This resulted in numerous paths that could be taken for this algorithm in improving EMS performance. First, this aging effect on the model differences needs to be understood in order to accurately make EMS decisions based on either SOC or SOE, or some combination of both. Next, the investigation into the slope of the model differences change was investigated and introduced as a potential candidate to use as an aging, or lifetime prediction of the battery as a way for the EMS to efficiently predict SOH of the individual batteries.

- **Battery Dimensional Changes -** The first main conclusion surrounding this research area was determining that a strain gauge could be directly applied to a battery and be used to show a profile correlation to a voltage profile. Ultimately, this showed that a strain gauge adhered directly to the cell can be used to correlate to SOC the same way voltage can be used.

- **Battery Dimensional Changes -** The location selected for the strain gauge was found to be critical in terms of visibility of the batteries expansion/contraction. In this analysis, the vent location on the battery was found to have the most visibility in the strain signal, which concludes the desire to engineer a special surface location on the cell casing to allow optimal placement of the strain gauge for the best possible measurement of the strain on the surface of the battery.

- **Dynamic Reconfiguration -** The initial round of simulations showed at the fundamental level that Dynamic Reconfiguration showed a performance enhancement in contrast to the traditional static configuration. The scope of this work focused on implementing the maximum number of switches per cell in order to understand any performance enhancement in the technology. The significance of the performance

enhancement was found to be heavily dependent on the initial conditions of the system, which were selected in ways to target specific application areas that Dynamic Reconfiguration could offer improvements.

- **Dynamic Reconfiguration -** After the scope of this research showed that Dynamic Reconfiguration found to have a performance enhancement, the study focused on understanding the Switches Per Cell value (SPC), and the resulting performance enhancement associated with the SPC value. The results showed that the maximum condition does in most cases result in the most performance enhancement, however, the improvement was also obtained at lower values of SPC. Ultimately, this showed that an engineering optimization could be performed when understanding the application specific impact in order to reduce the SPC value, while maintaining the same performance enhancement. Reducing the SPC in the system is ideal from a commercial sense, because lowering the SPC directly reduces the overall cost of the battery pack.

- **Dynamic Reconfiguration -** The State of Health minded reconfiguration was showed to better reduce the variance in performance from cell to cell comparisons in the battery pack amongst the vast amount of application specific simulations performed. The batteries showed better overall utilization, and ultimately resulted in less variance in terms of State of Health at the end of the simulation. By reducing the variance in cell to cell comparison, this resulted in longer overall operation, which led to increasing the deliverable energy to the load.

- **Dynamic Reconfiguration -** The selected configuration was found to significantly impact the percent improvement found with the DR topology relative to the static model. By increasing the parallel strings in the battery system, the percent improvement significantly increased. However, as the number of parallel strings increased, the complexity of the system increased significantly due to the overall configuration options becoming available.

5.2 Contributions

Since the areas of this research vary significantly, the contributions will be sorted by the specific area, with each item in the list denoted at the beginning the area that the bullet point covers:

- **State of Energy -** Examining this work in literature resulted in discussions about the advantages/disadvantages of SOE in comparison to SOC, however there were no studies directly comparing them under various temperature, and C-Rate conditions. This work directly compared these models to understand exactly where they differ, resulting in an in depth understanding of how the models provide different results that could be supplied to the EMS.

- **State of Energy -** Most of literature focused on a single discharge/charge event, while not extending the model differences as the battery is aged. By running aging experiments at 2 different C-Rates, further understanding of how these models compared against each other as the batteries age was previously undefined. Understanding how the model differences between SOC and SOE results could be used as a lifetime model indication, while not resulting in an extensive SOH model to be run separately can be used as a way to reduce the computational needs of the EMS system.

- **Battery Dimensional Changes -** This work, for the first time, showed that strain gauges could be directly applied to a battery as a way of monitoring the battery dimensional changes to correlate to the voltage, and furthermore to the SOC of the individual battery.

- **Battery Dimensional Changes -** This work also found that redesigning the battery case could result in an optimized surface for increased resolution of the strain measurement, which would allow for less signal noise, and better EMS decisions for the strain signal being utilized.

- **Dynamic Reconfiguration -** Within the Dynamic Reconfiguration research, this work introduced the first aging study on the Dynamic Reconfiguration technology performance improvement as the batteries are aged. Previous work studied the effect solely for a discharge or charge event. This work extended the research to understand the lifetime performance enhancements available when utilizing the Dynamic Reconfiguration concept.

- **Dynamic Reconfiguration -** Previous work on State of Health minded reconfiguration focused on the deliverable energy to the load in a single discharge event. With this research extending to lifetime modeling, the understanding of performance enhancement when reconfiguring the battery pack with State of Health minded control was evaluated and well understood.

- **Dynamic Reconfiguration -** Previous work focused on implementing switches into the system in a maximum Switches Per Cell (SPC) standpoint. This research studied the effect on the SPC value correlation to the resulting performance enhancement for the energy system.

5.3 Recommended Future Work

Since the areas of this research vary significantly, the recommended future work will be sorted by the specific area, with each item in the list denoted at the beginning the area that the bullet point covers:

- **State of Energy -** The next logical step in this research area would be to perform the lifetime experiments at both high and low temperature environments. The aging effect on SOC and SOE model differences was found for room temperature, but understanding the temperature effect on this relationship is critical for accurate commercial products.

- **State of Energy -** Since this study performed an aging experiment solely at 5, and 2 C-Rates, further exploration at lower C-Rates is needed. Ideally, 1 C-Rate, and 0.5 C-Rate would be recommended to evaluate if time and resources permit. Understanding a wider range of C-Rates and the effect on the SOC-SOE correlation is needed to move closer to a commercial application.

- **Battery Dimensional Changes -** This research showed the validation that a strain gauge could be directly placed onto a battery for correlation to SOC, further experiments would be needed to extend the scope of this research to optimizing the strain gauge sensor. The current strain measurement could be significantly improved by investing in better strain measurement systems, which are commercially available to help reduce signal noise apparent in the research. Additionally, adding temperature compensation strain gauges at the same location would significantly help reduce signal noise, especially in events of higher C-Rates where the surface temperature of the battery could change significantly, which would result in polarization of the strain signal.

- **Battery Dimensional Changes -** Further experimentation to understand the polarization effect of the strain gauge under current events is needed to validate the concept improvement in contrast with OCV measuring. Performing tests such as Hybrid Pulse Power Characterization (HPPC), or other discharge events (not full DOD) and setting the system to rest to understand how the voltage, and strain measurements polarize. However, this work is dependent on the optimization of the strain measuring equipment, in order to accurately make conclusions of the polarization effect in the strain measurement.

- **Dynamic Reconfiguration -** Studying the effect of performance on the total cell count in the pack, in order to understand if performance benefit remains the same while reconfiguring with State of Health minded control. Additionally, understanding the Switches Per Cell performance correlation as the total battery count in the system increases is essential to progressing towards a commercially viable product.

- **Dynamic Reconfiguration -** Since all of this research in this area focused on simulation level experiments to evaluate a wide range of application parameters, performing experimental round trials in a lab environment is essential to validating the results found in simulation. Selecting the right conditions to study would depend on the target application to pursue, and based on this work produced, exploring the conditions when placing fresh modules amongst aged would be one of the most significant simulations to validate in the laboratory.

Bibliography

[1] Henk Jan Bergveld. *Battery Management Systems*. 2002, pp. 1–328. ISBN: 978-90-481-6108-9. DOI: 10.1007/978-94-017-0843-2. arXiv: arXiv:1011.1669v3. URL: http://link.springer.com/10.1007/978-94-017-0843-2.

[2] Xiaopeng Chen et al. "An overview of lithium-ion batteries for electric vehicles". In: *2012 10th International Power & Energy Conference (IPEC)* (2012), pp. 230–235. DOI: 10.1109/ASSCC.2012.6523269. URL: http://ieeexplore.ieee.org/document/6523269/.

[3] E Joseph Nemanick and Ryan P Hickey. "The effects of O 2 pressure on LieO 2 secondary battery discharge capacity and rate capability". In: (2014). DOI: 10.1016/j.jpowsour.2013.12.016. URL: http://dx.doi.org/10.1016/j.jpowsour.2013.12.016.

[4] Languang Lu et al. "A review on the key issues for lithium-ion battery management in electric vehicles". In: *Journal of Power Sources* 226 (2013), pp. 272–288. ISSN: 03787753. DOI: 10.1016/j.jpowsour.2012.10.060. URL: http://dx.doi.org/10.1016/j.jpowsour.2012.10.060.

[5] Haisheng Chen et al. "Progress in electrical energy storage system: A critical review". In: *Progress in Natural Science*. 2009, pp. 291–312. DOI: 10.1016/j.pnsc.2008.07.014. URL: https://ac-els-cdn-com.ezproxy.library.wisc.edu/S100200710800381X/1-s2.0-S100200710800381X-main.pdf?{_}tid=3124b1b4-ea86-4014-baed-d994eae011df{\&}acdnat=1527789115{_}4466a9d8152a54ddf1eb90956df7e768.

[6] Jason Leadbetter and Lukas Swan. "Battery storage system for residential electricity peak demand shaving". In: *Energy and Buildings* 55 (2012), pp. 685–692. ISSN: 03787788. DOI: 10.1016/j.enbuild.2012.09.035. URL: http://dx.doi.org/10.1016/j.enbuild.2012.09.035.

[7] D. Kottick, M. Blau, and D. Edelstein. "Battery Energy Storage for Frequency Regulation in an Island Power System". In: *IEEE Transactions on Energy Conversion* 8.3 (1993), pp. 455–459. ISSN: 15580059. DOI: 10.1109/60.257059.

[8] Sekyung Han, Hee Han Soo, and Kaoru Sezaki. "Design of an optimal aggregator for vehicle-to-grid regulation service". In: *Innovative Smart Grid Technologies Conference, ISGT 2010* 1.1 (2010), pp. 65–72. ISSN: 0885-8950. DOI: 10.1109/ISGT.2010.5434773.

[9] Makena Coffman, Paul Bernstein, and Sherilyn Wee. "Integrating electric vehicles and residential solar PV". In: (2016). DOI: 10.1016/j.tranpol.2016.08.008. URL: https://ac-els-cdn-com.ezproxy.library.wisc.edu/S0967070X16305583/1-s2.0-S0967070X16305583-main.pdf?{_}tid=eccc85e8-d290-467f-9265-b20e2ef7aacb{\&}acdnat=1527287866{_}4861da20f31b3714650f95eefd5195ac.

[10] Ahmed Yousuf Saber and Ganesh Kumar Venayagamoorthy. "Plug-in vehicles and renewable energy sources for cost and emission reductions". In: *IEEE Transactions on Industrial Electronics* 58.4 (2011), pp. 1229–1238. ISSN: 02780046. DOI: 10.1109/TIE.2010.2047828.

[11] Bruno G. Pollet, Iain Staffell, and Jin Lei Shang. "Current status of hybrid, battery and fuel cell electric vehicles: From electrochemistry to market prospects". In: *Journal of Electrochemistry* (2012), pp. 235–249.

[12] A. Sciarretta and L. Guzzella. "Control of hybrid electric vehicles". In: *IEEE Control Systems* 27.2 (2007), pp. 60–70. ISSN: 1066-033X. DOI: 10.1109/MCS.2007.338280. URL: http://ieeexplore.ieee.org/ielx5/5488303/4140731/04140747.pdf?tp={\&}arnumber=4140747{\&}isnumber=4140731{\%}5Cnhttp://ieeexplore.ieee.org/xpls/abs{_}all.jsp?arnumber=4140747{\&}tag=1.

[13] Xuewei Qi et al. "Development and Evaluation of an Evolutionary Algorithm-Based Online Energy Management System for Plug-In Hybrid Electric Vehicles". In: *IEEE Transactions on Intelligent Transportation Systems* (2016), pp. 1–11. ISSN: 15249050. DOI: 10.1109/TITS.2016.2633542.

[14] Robert F Nelson. "Power requirements for batteries in hybrid electric vehicles". In: *Journal of Power Sources* 91 (2000), pp. 2–26. URL: www.elsevier.comrlocaterjpowsour.

[15] K.T Chau and Y.S Wong. "Overview of power management in hybrid electric vehicles". In: *Energy Conversion and Management* 43 (2002), pp. 1953–1968. ISSN: 01968904. DOI: 10.1016/S0196-8904(01)00148-0. URL: https://ac-els-cdn-com.ezproxy.library.wisc.edu/S0196890401001480/1-s2.0-S0196890401001480-main.pdf?{_}tid=84cfb6ff-4778-4664-8063-9b32acb971e9{\&}acdnat=1527276977{_}e4e4bd9c6723e1d9e48015ea9c01c39a.

[16] C.E. Sandy Thomas. ""How green are electric vehicles?"" In: (2012), pp. 6053–6062.

[17] *BU-1003: Electric Vehicle (EV) – Battery University*. URL: https://batteryuniversity.com/learn/article/electric{_}vehicle{_}ev (visited on 08/27/2018).

[18] Kong Soon Ng et al. "Enhanced coulomb counting method for estimating state-of-charge and state-of-health of lithium-ion batteries". In: *Applied Energy* 86.9 (2009), pp. 1506–1511. ISSN: 03062619. DOI: 10.1016/j.apenergy.2008.11.021. URL: http://dx.doi.org/10.1016/j.apenergy.2008.11.021.

[19] Sabine Piller, Marion Perrin, and Andreas Jossen. "Methods for state-of-charge determination and their applications". In: *Journal of Power Sources* 96.1 (2001), pp. 113–120. ISSN: 03787753. DOI: 10.1016/S0378-7753(01)00560-2. URL: https://ac-els-cdn-com.ezproxy.library.wisc.edu/S0378775301005602/1-s2.0-S0378775301005602-main.pdf?{_}tid=20adef14-4ba4-45c0-8ae3-2c11ae9c6f4e{\&}acdnat=1526774592{_}6bbad24cfedad4b25c467bff472f0286.

[20] James H. Aylor, Alfred Thieme, and Barry W. Johnson. "A Battery State-of-Charge Indicator for Electric Wheelchairs". In: *IEEE Transactions on Industrial Electronics* 39.5 (1992), pp. 398–409. ISSN: 15579948. DOI: 10.1109/41.161471.

[21] Xidong Tang et al. "Li-ion battery parameter estimation for state of charge". In: *Proceedings of the 2011 American Control Conference* (2011), pp. 941–946. ISSN: 0743-1619. DOI: 10.1109/ACC.2011.5990963. URL: http://ieeexplore.ieee.org/document/5990963/.

[22] H.L. Chan. "A new battery model for use with battery energy storage systems and electric vehicles power systems". In: *2000 IEEE Power Engineering Society Winter Meeting. Conference Proceedings (Cat. No.00CH37077)* 1.February 2000 (2016), pp. 470–475. DOI: 10.1109/PESW.2000.850009. URL: http://ieeexplore.ieee.org/document/850009/.

[23] S.J. Lee et al. “The State and Parameter Estimation of an Li-Ion Battery Using a New OCV-SOC Concept”. In: *2007 IEEE Power Electronics Specialists Conference* July (2007), pp. 2799–2803. ISSN: 0275-9306. DOI: 10.1109/PESC.2007.4342462. URL: http://ieeexplore.ieee.org/document/4342462/.

[24] Mark Verbrugge, Damon Frisch, and Brian Koch. “Adaptive Energy Management of Electric and Hybrid Electric Vehicles”. In: *Journal of The Electrochemical Society* 152.2 (2005), A333. ISSN: 00134651. DOI: 10.1149/1.1847658. URL: http://jes.ecsdl.org/cgi/doi/10.1149/1.1847658.

[25] Christian Fleischer et al. “Self-learning state-of-available-power prediction for lithium-ion batteries in electrical vehicles”. In: *2012 IEEE Vehicle Power and Propulsion Conference, VPPC 2012* I (2012), pp. 370–375. DOI: 10.1109/VPPC.2012.6422670.

[26] Shuoqin Wang et al. “Multi-parameter battery state estimator based on the adaptive and direct solution of the governing differential equations”. In: *Journal of Power Sources* 196.20 (2011), pp. 8735–8741. ISSN: 03787753. DOI: 10.1016/j.jpowsour.2011.06.078. URL: https://ac-els-cdn-com.ezproxy.library.wisc.edu/S0378775311013152/1-s2.0-S0378775311013152-main.pdf?{_}tid=79e64b22-439d-408a-9adf-5f2e26ba96e3{\&}acdnat=1526777611{_}f49df55cfd8fdad2106f014894c67464.

[27] Patrick J. van Bree et al. “Prediction of battery behavior subject to high-rate partial state of charge”. In: *IEEE Transactions on Vehicular Technology* 58.2 (2009), pp. 588–595. ISSN: 00189545. DOI: 10.1109/TVT.2008.928005.

[28] Bharat Balagopal and Mo Yuen Chow. “The state of the art approaches to estimate the state of health (SOH) and state of function (SOF) of lithium Ion batteries”. In: *Proceeding - 2015 IEEE International Conference on Industrial Informatics, INDIN 2015* 2 (2015), pp. 1302–1307. DOI: 10.1109/INDIN.2015.7281923.

[29] Seyed Mohammad Rezvanizaniani et al. “Review and recent advances in battery health monitoring and prognostics technologies for electric vehicle (EV) safety and mobility”. In: *Journal of Power Sources* 256 (2014), pp. 110–124. ISSN: 03787753. DOI: 10.1016/j.jpowsour.2014.01.085. URL: http://dx.doi.org/10.1016/j.jpowsour.2014.01.085.

[30] Shriram Santhanagopalan et al. “Review of models for predicting the cycling performance of lithium ion batteries”. In: *Journal of Power Sources* 156 (2006), pp. 620–628. DOI: 10.1016/j.jpowsour.2005.05.070. URL: https://ac-els-cdn-com.ezproxy.library.wisc.edu/S0378775305007810/1-s2.0-S0378775305007810-main.pdf?{_}tid=a6e15ecf-b873-44ce-9312-12a99de0e3c1{\&}acdnat=1526778058{_}0325ccac8df9f18b6fcfc92640d5babd.

[31] Guangzhong Dong et al. “An online model-based method for state of energy estimation of lithium-ion batteries using dual filters”. In: *Journal of Power Sources* 301 (2016), pp. 277–286. ISSN: 03787753. DOI: 10.1016/j.jpowsour.2015.10.011. URL: http://dx.doi.org/10.1016/j.jpowsour.2015.10.011.

[32] Hong Wen He et al. “A novel Gaussian model based battery state estimation approach: State-of-Energy”. In: *Applied Energy* 151 (2015), pp. 41–48. ISSN: 03062619. DOI: 10.1016/j.apenergy.2015.04.062. URL: http://dx.doi.org/10.1016/j.apenergy.2015.04.062.

[33] Kaiyuan Li, King Jet Tseng, and Lemuel Moraleja. “Study of the Influencing Factors on the Discharging Performance of Lithium-ion Batteries and Its Index of State of Energy”. In: (2016), pp. 0–6. DOI: 10.1109/IECON.2016.7793567.

[34] Yongzhi Zhang et al. “Lithium-Ion Battery Pack State of Charge and State of Energy Estimation Algorithms Using a Hardware-in-the-Loop Validation”. In: *IEEE Transactions on Power Electronics* 32.6 (2017), pp. 4421–4431. ISSN: 0885-8993. DOI: 10.1109/TPEL.2016.2603229. URL: http://ieeexplore.ieee.org/document/7553564/.

[35] Kaiyuan Li and King Jet Tseng. “Energy efficiency of lithium-ion battery used as energy storage devices in micro-grid”. In: *IECON 2015 - 41st Annual Conference of the IEEE Industrial Electronics Society* (2015), pp. 5235–5240. DOI: 10.1109/IECON.2015.7392923.

[36] Phillip J Kollmeyer. “Development and Implementation of a Battery-Electric Light-Duty Class 2a Truck including Hybrid Energy Storage”. In: (2015), p. 475.

[37] Xingtao Liu et al. “A method for state of energy estimation of lithium-ion batteries at dynamic currents and temperatures”. In: *Journal of Power Sources* 270 (2014), pp. 151–157. ISSN: 03787753. DOI: 10.1016/j.jpowsour.2014.07.107.

[38] Bultel Y. Mamadou, K., Lemaire, E., Delaille, A. “The State-of-Energy- A New Criterion for the Energetic Performances Evaluation of Electrochemical Storage Devices”. In: 25.35 (2010), pp. 105–112.

[39] Kaiyuan Li and King Jet Tseng. “An equivalent circuit model for state of energy estimation of lithium-ion battery”. In: *2016 IEEE Applied Power Electronics Conference and Exposition (APEC)*. IEEE, 2016, pp. 3422–3430. ISBN: 978-1-4673-8393-6. DOI: 10.1109/APEC.2016.7468359. URL: http://ieeexplore.ieee.org/document/7468359/.

[40] Rujian Fu, Meng Xiao, and Song-Yul Choe. “Modeling, validation and analysis of mechanical stress generation and dimension changes of a pouch type high power Li-ion battery”. In: *Journal of Power Sources* 224 (2013), pp. 211–224. DOI: 10.1016/j.jpowsour.2012.09.096. URL: https://ac-els-cdn-com.ezproxy.library.wisc.edu/S0378775312015285/1-s2.0-S0378775312015285-main.pdf?{_}tid=34424c64-10c5-11e8-9dda-00000aab0f27{\&}acdnat=1518530161{_}fe9a1754d5070e64a68d97aa818f0423.

[41] John Cannarella and Craig B. Arnold. “State of health and charge measurements in lithium-ion batteries using mechanical stress”. In: *Journal of Power Sources* 269 (2014), pp. 7–14. ISSN: 03787753. DOI: 10.1016/j.jpowsour.2014.07.003. URL: https://ac-els-cdn-com.ezproxy.library.wisc.edu/S0378775314010453/1-s2.0-S0378775314010453-main.pdf?{_}tid=e0919b61-5185-497e-811f-fcb5d616e069{\&}acdnat=1526851452{_}63fc1066f1237f1a002ad3d978b58aa1.

[42] Jae Hyun Lee, Hyang Mok Lee, and Soonho Ahn. “Battery dimensional changes occurring during charge/discharge cycles - Thin rectangular lithium ion and polymer cells”. In: *Journal of Power Sources* 119-121 (2003), pp. 833–837. ISSN: 03787753. DOI: 10.1016/S0378-7753(03)00281-7.

[43] Xianming Wang et al. “Understanding Volume Change in Lithium-Ion Cells during Charging and Discharging Using In Situ Measurements”. In: (2006). DOI: 10.1149/1.2386933ÍŤ. URL: http://jes.ecsdl.org.ezproxy.library.wisc.edu/content/154/1/A14.full.pdf.

[44] John Cannarella and Craig B. Arnold. “Stress evolution and capacity fade in constrained lithium-ion pouch cells”. In: *Journal of Power Sources* 245 (2014), pp. 745–751. ISSN: 03787753. DOI: 10.1016/j.jpowsour.2013.06.165. URL: http://dx.doi.org/10.1016/j.jpowsour.2013.06.165.

[45] Anup Barai et al. “A Study of the Effects of External Pressure on the Electrical Performance of a Lithium-ion Pouch Cell”. In: *2013 International Conference on Connected Vehicles and Expo (ICCVE)* (2013), pp. 2–6. DOI: 10.1109/ICCVE.2013.155. URL: http://ieeexplore.ieee.org/articleDetails.jsp?arnumber=6799809{\%}0Ahttp://ieeexplore.ieee.org/iel7/6784566/6799751/06799809.pdf?arnumber=6799809.

[46] M Wenger et al. “Investigation of gas sensing in large lithium-ion battery systems for early fault detection and safety improvement”. In: (2014), pp. 5654–5659. DOI: 10.1109/IECON.2014.7049366.

[47] Nassim A. Samad et al. “Observability analysis for surface sensor location in encased battery cells”. In: *Proceedings of the American Control Conference* 2015-July (2015), pp. 299–304. ISSN: 07431619. DOI: 10.1109/ACC.2015.7170752.

[48] P Wolf, S Moura, and M Krstic. “On optimizing sensor placement for spatio-temporal temperature estimation in large battery packs BT - Decision and Control (CDC), 2012 IEEE 51st Annual Conference on”. In: 973.1 (2012), pp. 973–978.

[49] Chi Yuan Lee et al. “In situ monitoring of temperature inside lithium-ion batteries by flexible micro temperature sensors”. In: *Sensors* 11.10 (2011), pp. 9942–9950. ISSN: 14248220. DOI: 10.3390/s111009942.

[50] S Al Hallaj and J R Selman. “A Novel Thermal Management System for Electric Vehicle Batteries Using Phase-Change Material”. In: *Journal of The Electrochemical Society* 147.9 (2000), pp. 3231–3236. URL: http://jes.ecsdl.org.ezproxy.library.wisc.edu/content/147/9/3231.full.pdf.

[51] Rui Zhao et al. “A review of thermal performance improving methods of lithium ion battery: Electrode modification and thermal management system”. In: *Journal of Power Sources* 299 (2015), pp. 557–577. DOI: 10.1016/j.jpowsour.2015.09.001. URL: https://ac-els-cdn-com.ezproxy.library.wisc.edu/S0378775315302627/1-s2.0-S0378775315302627-main.pdf?{_}tid=c9d0cf00-8fe8-47bc-ab79-7936d8e54382{\&}acdnat=1527722244{_}f9ba699233fa9fc48

[52] Zhonghao Rao and Shuangfeng Wang. “A review of power battery thermal energy management”. In: *Renewable and Sustainable Energy Reviews* 15 (2011), pp. 4554–4571. DOI: 10.1016/j.rser.2011.07.096. URL: https://ac-els-cdn-com.ezproxy.library.wisc.edu/S1364032111003418/1-s2.0-S1364032111003418-main.pdf?{_}tid=5cfe275e-b57d-4a75-8b9a-0ed328735194{\&}acdnat=1527722118{_}9431dce209fa16dde2997a4b0cc00ac3.

[53] Qian Wang et al. “A critical review of thermal management models and solutions of lithium-ion batteries for the development of pure electric vehicles”. In: *Renewable and Sustainable Energy Reviews*. 2016. URL: https://ac-els-cdn-com.ezproxy.library.wisc.edu/S1364032116301435/1-s2.0-S1364032116301435-main.pdf?{_}tid=3b925224-5677-48ab-9f84-9f499d441c5b{\&}acdnat=1527720767{_}12a2f39d06d6795757472054bfe4b227.

[54] W.F. Bentley. “Cell balancing considerations for lithium-ion battery systems”. In: *The Twelfth Annual Battery Conference on Applications and Advances* (1997), pp. 223–226. ISSN: 1089-8182. DOI: 10.1109/BCAA.1997.574107. URL: http://ieeexplore.ieee.org/document/574107/.

[55] Jian Cao, Nigel Schofield, and Ali Emadi. “Battery balancing methods: A comprehensive review”. In: *2008 IEEE Vehicle Power and Propulsion Conference, VPPC 2008* (2008), pp. 3–8. DOI: 10.1109/VPPC.2008.4677669.

[56] Liang He et al. “Exploring adaptive reconfiguration to optimize energy efficiency in large-scale battery systems”. In: *Proceedings - Real-Time Systems Symposium* (2013), pp. 118–127. ISSN: 10528725. DOI: 10.1109/RTSS.2013.20.

[57] Eugene Kim, Kang G. Shin, and Jinkyu Lee. “Modeling and Real-Time Scheduling of Large-Scale Batteries for Maximizing Performance”. In: *Proceedings - Real-Time Systems Symposium* 2016-Janua (2016), pp. 33–42. ISSN: 10528725. DOI: 10.1109/RTSS.2015.11.

[58] Large-scale Lithium-ion Battery Systems et al. “RAC : Reconfiguration-Assisted Charging in”. In: 7.3 (2016), pp. 1420–1429.

[59] Sebastian Steinhorst et al. “Distributed reconfigurable Battery System Management Architectures”. In: *Proceedings of the Asia and South Pacific Design Automation Conference, ASP-DAC* 25-28-Janu (2016), pp. 429–434. DOI: 10.1109/ASPDAC.2016.7428049.

[60] Federico Baronti et al. “Design of a module switch for battery pack reconfiguration in high-power applications”. In: *IEEE International Symposium on Industrial Electronics* (2012), pp. 1330–1335. ISSN: 2163-5137. DOI: 10.1109/ISIE.2012.6237283.

[61] Liang He et al. “SHARE: SoH-Aware Reconfiguration to Enhance Deliverable Capacity of Large-Scale Battery Packs”. In: *Proceedings of the ACM/IEEE Sixth International Conference on Cyber-Physical Systems - ICCPS ’15* (2015), pp. 169–178. DOI: 10.1145/2735960.2735967. URL: http://dl.acm.org/citation.cfm?doid=2735960.2735967.

[62] Song Ci, Ni Lin, and Dalei Wu. “Reconfigurable Battery Techniques and Systems: A Survey”. In: *IEEE Access* 4 (2016), pp. 1175–1189. ISSN: 21693536. DOI: 10.1109/ACCESS.2016.2545338.

[63] Hahnsang Kim and Kang G. Shin. “On dynamic reconfiguration of a large-scale battery system”. In: *Proceedings of the IEEE Real-Time and Embedded Technology and Applications Symposium, RTAS* (2009), pp. 87–96. ISSN: 15453421. DOI: 10.1109/RTAS.2009.13.

[64] Gene Berdichevsky et al. “The Tesla Roadster Battery System Tesla Motors”. In: (2007). URL: http://large.stanford.edu/publications/power/references/docs/tesla.pdf.

[65] Mathworks. *No Title*. 2018.